CONTRAST-ENHANCED MAGNETIC RESONANCE LIVER IMAGE REGISTRATION, SEGMENTATION, AND FEATURE ANALYSIS FOR LIVER DISEASE DIAGNOSIS

A Dissertation
Presented to
The Academic Faculty

by

Ji Hun Oh

In Partial Fulfillment
of the Requirements for the Degree
Doctor of Philosophy in the
School of Electrical and Computer Engineering

Georgia Institute of Technology
December 2012

CONTRAST-ENHANCED MAGNETIC RESONANCE LIVER IMAGE REGISTRATION, SEGMENTATION, AND FEATURE ANALYSIS FOR LIVER DISEASE DIAGNOSIS

Approved by:

Professor Xiaoping Hu, Advisor
Department of Biomedical Engineering
Georgia Institute of Technology

Professor Guotong Zhou
School of Electrical and Computer Engineering
Georgia Institute of Technology

Professor Anthony Joseph Yezzi, Co-Advisor
School of Electrical and Computer Engineering
Georgia Institute of Technology

Professor Robert J Butera
School of Electrical and Computer Engineering
Georgia Institute of Technology

Professor Patricio Antonio Vela
School of Electrical and Computer Engineering
Georgia Institute of Technology

Professor Diego Martin
Department of Radiology
University of Arizona

Date Approved: November 12, 2012

I lovingly dedicate this dissertation to my wife, Dr. Bo Yeon Lee, and my family in South Korea, who supported me.

ACKNOWLEDGEMENTS

First and foremost, I want to express my sincere gratitude to my research advisor, Prof. Xiaoping Hu, for his academic support of my Ph.D. study and research. His guidance with broad, insightful knowledge helped me in all the time of research and write this dissertation. It has been truly my honor to belong to your BITC group. My sincere gratitude also goes to Prof. Diego Martin in the Department of Radiology at University of Arizona, Tucson for providing image data and your priceless medical knowledge needed for my understanding, and reviewing my papers. I owe my faithful gratitude to Dr. Oskar Skrinjar, who is my previous research advisor from my master period, who taught me his abundant knowledge related to medical image processing. I would also like to thank my thesis committee members, Prof. Anthony Joseph Yezzi, Prof. Patricio Antonio Vela, Prof. Guotong Zhou, and Prof. Robert J Butera for their time and support.

I thank my BITC lab members in the school of medicine at Emory University: Prof. Jae Keun Park, Dr. Sin Yeob Ahn, Ki Sueng Choi, Dr. Jae Min Shin, Dr. Jason Langley, Behnaz Yousefi for their help and friendship. I owe my gratitude to my friends at Georgia Tech, especially to Dr. Je Hoon Lee in Prof. Allen Tannenbaum's lab, Brandi Pitta and Daniel Luh in Dr. Oskar Skrinjar's lab.

Most importantly, I must express my deepest gratitude to my wife Dr. Bo Yeon Lee, my father Mr. Se Dong Oh, my mother Mrs. Mi Hoe Kim, my sister Mrs. You Lee Oh, her husband Mr. Beong Woo Kim for their continuous help and support. Without them, I would not imagine that I could earn this Ph.D. degree.

Last but not least, I appreciate Jane Chisholm, who got recognized as great writing instructor at Georgia Tech, for her substantial help of reviewing my papers.

TABLE OF CONTENTS

LIST OF TABLES

LIST OF FIGURES

SUMMARY

Medical image processing, analysis, and visualization are emerging fields of study that enable quantitative analysis and visualization of medical images of numerous modalities such as magnetic resonance image, computed tomography, positron emission tomography, and ultrasound. They have become significant components in many fields of bio-medical research and clinical practice. Image data sets convey highly detailed information as their dimensions increase, which needs to be interpreted in a timely and accurate manner for analysis. To do this, registration of two images of the same target is essential for many areas in which the corresponding voxels between the two images convey the valuable information. There are numerous algorithms accounting for the distortion between two images, but it is challenging to find the true distortion taking physical and biological characteristics of tissue into account. Also, segmentation is critical for delineating structures or specific organ of interest and discriminating them from surroundings or background. From the viewpoint of computer vision, this separation requires very complicated algorithm in some cases even though it looks explicit to human vision system.

The first focus of the research in this dissertation is to derive adaptive image registration algorithm to contrast-enhanced liver MRI. Voluntary motion caused by patient movement is corrected by translation-only registration, but there still remains involuntary motion arising from tissue deformation. Because of intensity change between images, a scarcity of landmarks, and a varying shape and size of the liver, any image registration methods that are currently popular are not applicable in the case of liver image. To overcome these drawbacks, we propose an intensity-based non-parametric registration using local correlation coefficient computed at every voxel. In

addition, symmetric registration approach and its parallel implementation to graphics processing units are implemented to improve the accuracy of motion estimation and accelerate the convergence speed.

The second focus of this research is to design image segmentation algorithm for delineating the entire liver. Visual delineation using human interaction is both time consuming and error prone, so the automation of the process has become a necessity. However, segmentation is often tackled because of the geometric proximity of the liver to its surrounding organs, weak boundary, dual enhancement of kidney and liver, and inhomogeneous intensity distribution. We propose a novel region-based active contour method that couples the gradient information and local regional statistics on multiple partitions, approximating the Couinaud liver segments.

The last focus of this research is to build a supervised classification using highly correlated image features over the segmented volume of interest in motion-corrected time series with chronic liver disease, measured as fibrotic burden. The colormap representation of voxel-wise predicted scores over the entire liver would facilitate the finding of suspicious regions. The contributions of this dissertation are to develop

- motion correction algorithm to register three-dimensional contrast-enhanced MR liver time sequences by the symmetric demons force based on local correlation coefficient and its implementation to GPU,

- motion correction algorithm to find the corresponding oblique and warped plane in a three-dimensional MRI to a two-dimensional histology image within allowable error range,

- segmentation algorithm to delineate the entire liver by an edge function-scaled region-based active contour on multiple partitions, with a new compactly-support edge function,

- and feature analysis to assess the level of remaining liver function and to estimate regional liver function using signal intensity and texture information.

CHAPTER I

INTRODUCTION

1.1 Motivation and Background

1.1.1 Motivation

In the United States, liver disease is the fourth leading cause of death during the most productive adult years. Hepatitis results from a variety of etiologies, all having the capacity to induce inflammation and fibrosis leading to chronic liver disease (CLD). CLD is a common cause of primary liver malignancy, which is becoming one of the more common malignancies overall. Figure 1 shows the progress of CLD. Patients with CLD and metastatic liver tumors commonly use cross-sectional imaging for a routine diagnostic testing. The ability to also measure the degree of CLD severity has been lacking in image-based tests. Consequently, clinicians have relied upon indirect measures derived from clinical status and blood or tissue tests using a biopsy that are neither highly sensitive nor specific to early disease or to small changes in disease

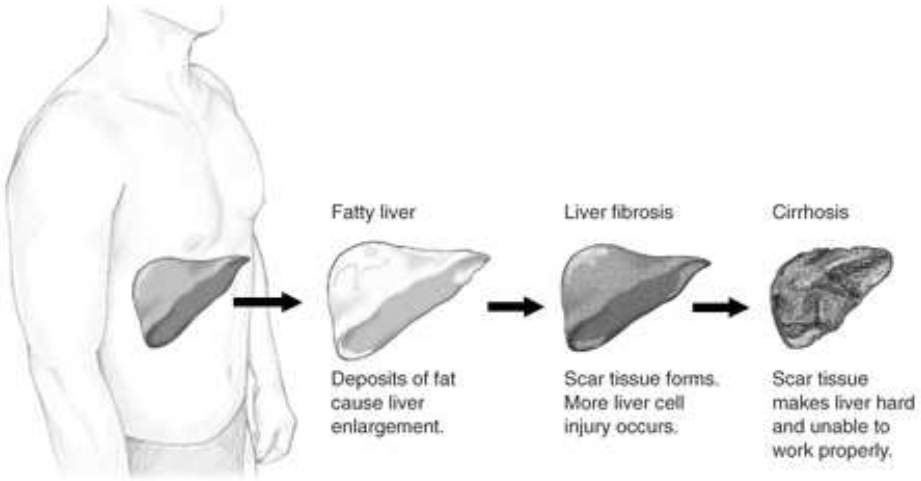

Figure 1: The progress of chronic liver disease.

progression or improvement. For this reason, we will focus on the improvement of automated MRI-based diagnosis.

1.1.2 Liver Motion

Organ motion can cause artifacts in abdominal imaging, including a liver for a magnetic resonance (MR) image, and lower the quality of analysis. The development of a strategy correcting motion requires a thorough knowledge and study of liver motion. Suramo et al. [1] suggested that a movement range of the liver is 55 mm during maximum respiration, 25 mm during normal respiration, 9 mm during suspended respiration, and 2 mm during suspended respiration with a bar placed above the abdomen. Danrad et al.[2] reported that the motion of the diaphragm and the liver is predominant in the superior-inferior (SI) direction with an average displacement ($\pm$SD) (quiet respiration) of 12$\pm$7 mm (range 7$\sim$28 mm) and 10$\pm$8 mm (range 5$\sim$17 mm), respectively. Blackall et al. [3] demonstrated the motion with the relationship between the diaphragm and the liver during the breathing cycle: In the superior surface of the liver, the large deformation from direct contact with the diaphragm occurs, and the inferior surface of the liver is in contact with the back of the body cavity and is compressed against the surface as the diaphragm descends. Blackall et al. also reported that liver motion measures 19$\pm$8 mm for shallow breathing and 37$\pm$8 mm for deep breathing. Herline et al. [4] observed liver motion in case of insufflations in interactive image-guided surgery and quantified an average motion of 2.5$\pm$1.4 mm. An average total liver motion secondary to the respiration in all patients is 10.8$\pm$2.5 mm. For the liver tumor, Shimizu et al. [5] indicated that the mean length of displacement is 21 mm in the cranio-caudal direction, 8 mm in the anterior-posterior direction, and 9 mm in the lateral direction. The focus of studies by Clifford et al. [6] and Rohlfing et al. [7] accounted for tissue deformation which the significant translation cannot compensate for. Clifford et al. showed that rigid-body translation is

Table 1: Hepatic rigid motion secondary to respiration (courtesy of [6]).

Study/date	Number of subjects	Cranio-caudal (mm) Quiet inspiration	Cranio-caudal (mm) Deep inspiration	Anterior-posterior (mm)	Lateral (mm)	Modality
Weiss (1972)[32]						
(using scintigraphy)	12	11 ± 3	12–75			Scintigraphy
(using fluoroscopy)	25	13 ± 5				Fluoroscopy
Harauz (1979)[33]	51	14				Scintigraphy
Suramo (1984)[34]	50	25	55			US
Korin (1992)[35]	15	13	39	2.5		MRI
Davies (1994)[27]	9	10 ± 8	37 ± 8			US
Herline (1999)[13]	2	10.8 ± 2.5				Optical tracking
Shimizu (1999)[37]	1	21		8	9	MRI
Shimizu (2000)[36]	6	10.6 ± 7.0		4.6 ± 1.6	5.2 ± 1.8	MRI
Rohlfing (2001)[38]	4	12–26		1–12	1–3	MRI

an average of 12∼26 mm in cranio-caudal shift, 1∼12 mm in anterior-posterior shift, and 1∼3 mm in lateral shift.

The error introduced by assuming rigid-body motion is 3 mm on average, which may be explained as non-rigid deformation. Only 18% of the liver recovers back to the same position. In other words, the liver does not reoccupy the same position at identical moments in the respiratory cycle, which is defined as motion with respect to surrounding tissue. Rohlfing et al. demonstrated that the most global motion is captured by rigid transformation, and residual deformation amounts to approximately 6 mm as a result of implementing a free-form deformation based on B-spline. Since above registration algorithm is based on control points, it tends to be sensitive in some non-regular or non-uniform regions. Normally, the error introduced by assuming rigid liver motion averages 3 mm. To date, other factors such as a needle pressure during a transjugular intrahepatic portosystemic shunt (TIPS) procedure or heartbeat may cause motion in the liver. 1 Hz oscillations along all axes are present and consistent with the cardiac rhythm. According to the study by Venkatraman et al. [8], the motion caused by needle insertion–2.7∼13.2 (7.4±3.9) mm in the cranio-caudal direction, 1.1∼2.8 (2.2±0.7) mm in the anterior-posterior direction, and 1.4∼3.1 (2.2±0.7) mm in the lateral direction–is not big compared to that caused by respiration–(3.9∼12.3

(7.3±3.0) mm in the cranio-caudal direction, 1.9∼3.6 (2.5±0.7) mm in the anterior-posterior direction, and 1.2∼2.5 (1.9±0.4) mm in the lateral direction. Since needle insertion is not involved in our imaging acquisition process, we will disregard motion caused by that factor.

As indicated in the above studies, the numerical results of liver motion is not exactly consistent since researchers conducted experiments on not only different subjects, but the number of subjects was also not the same. Also the inconsistency of results in studies depends on which methodology is used for estimating motion. Obviously, all the studies agree in some sense that liver motion consists of rigid body motion error because of a patient's respiration and relatively small tissue deformation.

1.1.3 Non-Rigid Image Registration: Demons

A representative algorithm of diffusing models, optical flow, is based on the assumption that the intensity of a reference image is identical to the intensity of a moving image, and the displacement is small. Therefore, this constraint is likely to fail to match images with slightly different intensities and relatively big displacements. To supplement these weaknesses, Thirion [9] introduced image matching method using demons forces as illustrated in Figure 2. The author got a general idea from the concept of diffusing models with a parallel with Maxwell's demons, which accounts for the paradox of the second law of thermodynamics.

The estimated displacement incremental field $\vec{u}$ computed at point P in S to match the corresponding point in M is

$$\vec{u} = \frac{(S-M)\vec{\nabla}S}{(\vec{\nabla}S)^2 + (S-M)^2}, \tag{1}$$

where $\vec{u} = (u_x, u_y, u_z)$, S is the static image, M is the moving image, $\vec{\nabla}S$ is the gradient of the static image, and $(\vec{\nabla}S)^2 = (\vec{\nabla}S)^T(\vec{\nabla}S)$. Afterwards, in [10], Cachier et al. improved the original demons algorithm in which non-rigid matching is placed on a

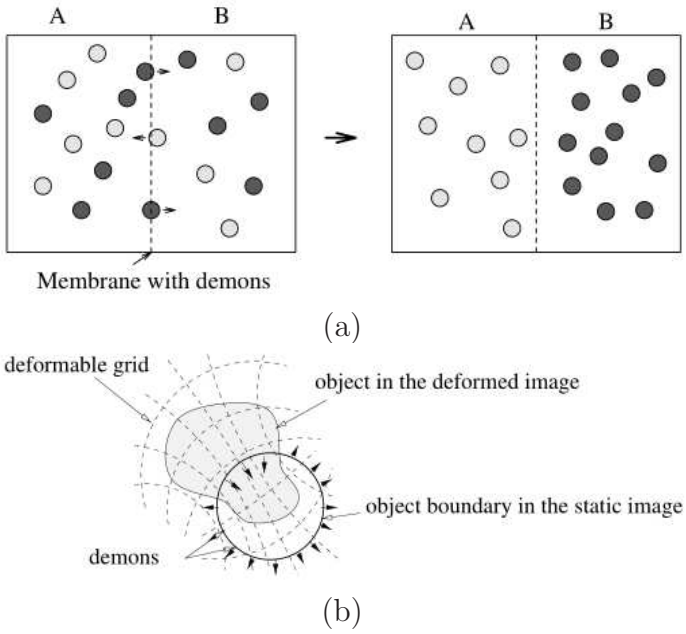

Figure 2: (a) Maxwell's demons and a mixed gas; (b) Diffusing models: the demons act as effectors along the contours of the static image (courtesy of [9]).

minimization framework and proved that the demons algorithm is an approximation of a second-order gradient descent. In addition, Cachier et al. derived a positive homogenization normalized factor α that allows the strength of demons forces to be adjusted adaptively in each iteration, and $\vec{u}$ is bounded by $\frac{1}{2\alpha}$. Thereby, the equation becomes

$$\vec{u} = \frac{(S-M)\vec{\nabla}S}{(\vec{\nabla}S)^2 + \alpha^2(S-M)^2}. \tag{2}$$

Next, to achieve accelerated convergence, Rogelj and Kovačič [11] and Wang et al. [12] hit on the novel idea from Newton's third law such that one force is the same in quantity, but the opposite in direction from the other force that is called 'active force'. Thus, the combined displacement field becomes

$$\vec{u} = \frac{(S-M)\vec{\nabla}S}{(\vec{\nabla}S)^2 + \alpha^2(S-M)^2} + \frac{(S-M)\vec{\nabla}M}{(\vec{\nabla}M)^2 + \alpha^2(S-M)^2}. \tag{3}$$

Obviously, the demons algorithm is attractive when we manipulate a huge size of image data because it is much faster and stabler in computation than parametric

registrations using B-spline or thin-plate-spline deformation. To date, studies about inverse consistent deformations [13, 14] have actively developed diffeomorphic registration on the frame of the demons algorithm. This diffeomorphic framework may not be required for small-scale and smooth deformation of the liver case, so we ignored this concept in our research.

1.1.4 Image Segmentation: Active Contours and Level Sets

Active contours, or called snakes, refer to a curve evolution to detect objects in a image. There are a couple of representative algorithms, a geodesic active contour and a region-based active contour.

The geodesic active contour (GAC) [15] is one that evolves in the normal direction by the motion of mean curvature and stops on the boundary with strong gradient magnitude. The speed of evolving the curve is characterized by an edge detector that is a positive and decreasing function g of the gradient of the image I,

$$g(I(x,y)) = \frac{1}{1+\alpha|\nabla G_\sigma(x,y) * I(x,y)|^p},\ p \geq 1, \tag{4}$$

where $G_\sigma(x,y) * I(x,y)$ is a smoothed image generated by the convolution of image I with the Gaussian $G_\sigma(x,y) = \sigma^{-1/2} e^{-|x^2+y^2|/4\sigma}$. The smoothing convolution can be substituted by a geometric heat equation that smoothes the image without smearing edges. α determines the shift of the edge function. Other choices of monotonic decreasing functions are proposed in a Perona and Malik type nonlinear diffusion equation [16]:

$$g(I(x,y)) = \frac{1}{e^{\alpha|\nabla G_\sigma(x,y) * I(x,y)|^2}}. \tag{5}$$

In Riemannian space the energy functional indicating the length of a curve is given by

$$E_{GAC}(C) = \int_0^L g(|\nabla I(C(q))|)ds = \int_0^1 g(|\nabla I(C(q)))|C'(q)|dq, \tag{6}$$

where ds is the Euclidean arc-length, which can be change changed into parametric form using $ds = |C'(q)|dq$. $C(q) : [0,1] \rightarrow \mathbf{R}^2$ is a parametrized, enclosed planar curve. To minimize the energy functional (6), the Euler-Lagrange equation is given by

$$C_t = g(I)\kappa\vec{N} - (\nabla g \cdot \vec{N})\vec{N}, \tag{7}$$

where κ is the curvature and $\vec{N}$ is the inward normal to the curve. We can deform the curve evolution (7) into a levelset representation according to $C_t = \beta\vec{N} \rightarrow \phi_t = \beta|\nabla\phi|$ and $\vec{N} = -\frac{\nabla\phi}{|\nabla\phi|}$:

$$\begin{aligned} \frac{\partial\phi}{\partial t} &= (g(I)\kappa + \nabla g \cdot \frac{\nabla\phi}{|\nabla\phi|})|\nabla\phi| \\ &= g(I)|\nabla\phi|\kappa + \nabla g(I) \cdot \nabla\phi, \end{aligned} \tag{8}$$

where

$$\kappa = div\left(\frac{\nabla\phi}{|\nabla\phi|}\right). \tag{9}$$

To increase the speed to convergence, we add the velocity constant ν, producing the final solution

$$\frac{\partial\phi}{\partial t} = g(I)|\nabla\phi|(\kappa + \nu) + \nabla g(I) \cdot \nabla\phi. \tag{10}$$

The Chan-Vese model of region-based active contours (CVRAC) [17] is a particular case of a minimal partition problem introduced by the Mumford-Shah functional [18]. Under the assumption that image I has two regions of piecewise constant intensities, the contour evolves to the boundary of objects in which the intensities inside and outside the contour are differentiated. Let C_{in} denote the interior region, and C_{out} the exterior region of the contour. The energy functional of CVRAC model is defined

as

$$
\begin{aligned}
&E_{CVAC}(c_1, c_2, C) \\
&= \lambda_1 \int_{C_{in}} |I(x,y) - c_1|^2 dxdy + \lambda_2 \int_{C_{out}} |I(x,y) - c_2|^2 dxdy \\
&+ \mu \cdot \text{Length}(C) + \nu \cdot \text{Area}(inside(C)),
\end{aligned} \tag{11}
$$

where c_1 and c_2 are two average intensities inside and outside the contour, respectively. $\lambda_1, \lambda_2 > 0$ are fixed parameters, and μ and ν control the smoothness of the zero level set and the propagation speed, respectively. In the levelset formulation, C is represented by the zero level set of Lipschitz function $\phi(x, y)$, and the inside and outside regions are denoted by the Heaviside function as illustrated in Figure 3.

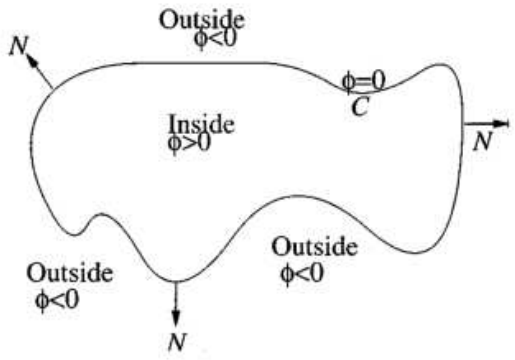

Figure 3: Definition of curve C in the level set representation (courtesy of [17]).

Let Ω be a bounded open subset of $\mathbf{R}^2$. The energy functional (11) in the level set formulation is

$$
\begin{aligned}
&E_{CVAC}(c_1, c_2, \phi) \\
&= \lambda_1 \int_{\Omega} |I(x,y) - c_1|^2 H(\phi(x,y)) dxdy \\
&+ \lambda_2 \int_{\Omega} |I(x,y) - c_2|^2 (1 - H(\phi(x,y))) dxdy \\
&+ \mu \int_{\Omega} |\nabla H(\phi(x,y))| dxdy + \nu \int_{\Omega} H(\phi(x,y)) dxdy,
\end{aligned} \tag{12}
$$

The average intensities can be expressed as

$$c_1 = \frac{\int_\Omega I(x,y) \cdot H(\phi(x,y))dxdy}{\int_\Omega H(\phi(x,y))dxdy}, \tag{13}$$

$$c_2 = \frac{\int_\Omega I(x,y) \cdot (1 - H(\phi(x,y)))dxdy}{\int_\Omega (1 - H(\phi(x,y)))dxdy}, \tag{14}$$

where $H(z)$ is the Heaviside function and $\delta(z)$ is the one-dimensional Dirac function,

$$H(z) = \begin{cases} 1, & \text{if } z \geq 0 \\ 0, & \text{if } z < 0, \end{cases} \quad \delta_0(z) = \frac{d}{dz} H(z). \tag{15}$$

The gradient descent associated with Euler-Lagrange equation for ϕ is

$$\frac{\partial \phi}{\partial t} = \delta_0(\phi)[-\lambda_1(I - c_1)^2 + \lambda_2(I - c_2)^2 + \mu\kappa - \nu]. \tag{16}$$

Because $\delta_0(\phi)$ has finite small local support in the level sets, to extend the evolution to all of the level sets, we can replace it by $|\nabla\phi|$ [19]. Thus, the global minimization of the level set for the CVRAC model is

$$\frac{\partial \phi}{\partial t} = |\nabla(\phi)|[-\lambda_1(I - c_1)^2 + \lambda_2(I - c_2)^2 + \mu\kappa - \nu]. \tag{17}$$

1.1.5 Image Analysis for Liver Disease Diagnosis

The study to find the way to evaluate the usefulness of a computer algorithm-based on signal intensity changes and textural features and classification method on imaging modalities such as MR, CT, and Ultrasonic is in progress by some researchers [20, 21, 22].

Contrast-enhanced perfusion MRI refers to the use of MRI to quantify hepatic perfusion parameters such as blood flow (rCBV) at the tissue level [23, 24, 25]. The

3-D gradient echo sequence performed in conjunction with parallel imaging is acquired with high temporal resolution. Concentration is estimated by mathematical models representing the relationship between signal intensity and concentration of contrast material. Resulting time-activity curves were fitted by using tracer kinetic modeling (single-input or dual-input, single-compartment or dual-compartment). Or model-free approach estimates parameters (hepatic perfusion index or portal venous perfusion index) derived from the initial slope of tissue concentration time curve. But, the remaining challenges are improving spatial and temporal resolution, accurate quantification of tissue contrast material, and validation of parameters obtained from fitting curves to kinetic models [26].

In 1973, Haralick [27] proposed a grey-level co-occurrence matrix (GLCM), which is also called the grey tone spatial dependency matrix, texture measurements have been a tool to represent the conditional joint probabilities of all pair wise combination of grey levels in the spatial window of interest given two parameters: interpixel distance (δ) and orientation (θ). The second order statistics computed from the texture of liver MR image included mean gray-scale value, standard deviation (SD), contrast, angular second moment, entropy, mean, and inverse difference moment of ROIs of all combination imaging data [20]. Those seven parameters from obtained textural features were processed by an artificial neural network with learning algorithm of back propagation comprising seven-unit input layer, six-unit hidden layer, and one-unit output layer, and it outputted a continuous number between 0 (absent) and 1 (present).

Multiple regression analysis was used to examine correlation between the seven numeric values of texture features by the finite difference method and the pathologic degree of hepatic fibrosis. Correlation coefficients and Area Under the Curve (Az) values were greatest with contrast-enhanced equilibrium phase images by the computer algorithm, whereas the values of equilibrium phase images by the radiologists'

interpretations were not so high. Reticular hyper-intensity because of delayed enhancement on gadolinium-enhanced equilibrium phase images was better recognized by the computer algorithm.

1.1.6 Potential Clinical Applications

The method developed here for contrast-enhanced MRI of liver can be extended to similar applications of other organs, including brain, cardiac, and breast imaging. For brain imaging, contrast-enhanced MRI permits better visualization of tumor, congenital abnormalities, vascular malformations, acute inflammatory lesions with early disruption of the blood brain barrier, acute ischemia and stroke. For cardiac imaging, perfusion imaging is often performed with contrast-enhanced MRI. For breast imaging, contrast-enhanced MRI is a tool for tumor detection with a sensitivity considerably higher than x-ray mammography or ultrasound.

Computer-aided diagnosis (CAD) system using contrast-enhanced MRI time series as shown in Figure 4 can assist clinicians in interpreting medical images comprehensively with increased throughput. The work in this dissertation research provides improvements in a number of aspects, including preprocessing, registration and feature analysis and is expected to benefit CAD in general.

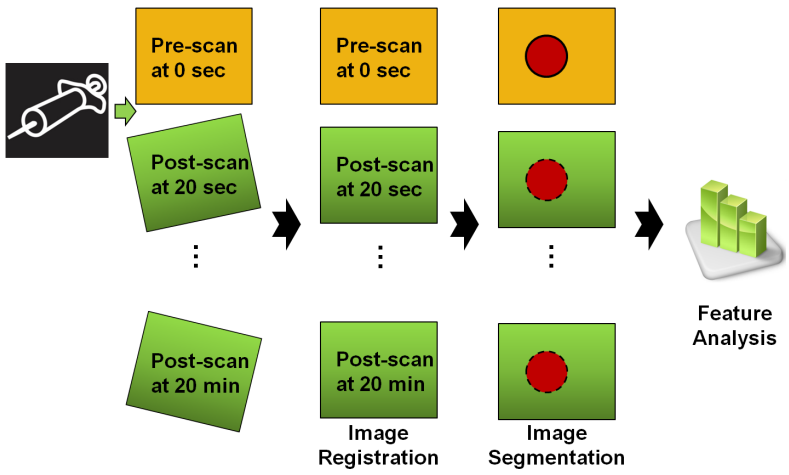

Figure 4: Computer-aided diagnosis system using contrast-enhanced MRI sequences.

1.2 Research Objective

The global objectives of this research are to develop a liver-specific magnetic resonance (MR) image registration and segmentation algorithms and to find highly correlated MR imaging features that help automatically score the severity of chronic liver disease (CLD). Our developed computer-aided diagnosis classifier measures the fibrotic burden on the histology. For a concise analysis of liver disease, time sequences of 3D MR images should be preprocessed through an image registration to compensate for the patient motion, respiration, or tissue motion. In addition, to improve the accuracy of the correlation between pathologic evaluations on surgical specimens and regions of interest (ROIs) of the MR image volume, it is necessary to find oblique and warped planes in the MR image volume corresponding to the histology slice images within an allowable error.

To register contrast-enhanced MR image volume sequences, we propose a novel version of the demons algorithm that is based on a bi-directional local correlation coefficient (Bi-LCC) scheme. This scheme improves the speed at which a convergent sequence approaches to the optimum state and achieves the higher accuracy. Furthermore, the simple and parallelizable hierarchy of the Bi-LCC demons can be implemented on a graphics processing unit (GPU) using OpenCL. To register the 2D histology image and the 3D MR image volume, we propose a similarity transformation followed by a non-rigid registration scheme using a liver segmentation and pairs of point landmarks selected by experts. To automate segmentation of the liver parenchyma regions, an edge function-scaled region-based active contour (ESRAC), which hybridizes gradient and regional statistical information, with approximate partitions of the liver was proposed.

A significant goal in grading liver disease is to assess the level of remaining liver function and to estimate regional liver function. On motion-corrected and segmented

liver parenchyma regions, for quantitative analysis of the hepatic extraction of liver-specific MRI contrast agent, liver signal intensity change is evaluated from hepatobiliary phases (3-20 minutes), and parenchymal texture features are deduced from the equilibrium (3 minutes) phase. To build a classifier using texture features, a set of training input and output values, which is estimated by experts as a score or a percentage of malignancy, trains the supervised learning algorithm using a multivariate normal distribution model and a maximum a posterior (MAP) decision rule. We will validate the classifier by assessing the prediction accuracy with a set of testing data.

1.3 Organization of Dissertation

The structure of the dissertation is outlined as follows:

- Chapter 2 presents the imaging protocols and contrast agent to be used for this research.
- Chapter 3 presents contrast-enhanced liver three-dimensional magnetic resonance (MR) image registration using bi-directional local correlation coefficient demons and its implementation on graphics processing unit using OpenCL. It also presents liver two-dimensional histology to three-dimensional MR image registration with experimental studies.
- Chapter 4 presents a new edge function scaled region-based active contour (ESRAC) and its application to an automate liver segmentation in contrast-enhanced MR image with experimental studies.
- Chapter 5 presents feature analysis, including signal intensity and texture feature analyses, and supervised learning algorithm using a multivariate normal distribution model and a maximum a posterior decision rule with test results.
- Chapter 6 provides a summary of the research performed and its key conclusions.

CHAPTER II

PROTOCOLS AND CONTRAST AGENT

The MR studies were performed on a 1.5 T scanner (Siemens Medical Solutions, Emory university, Atlanta, GA USA). Gadolinium (Gd)-based, contrast-enhanced, T1-weighted gradient echo protocol (iVIBE) was used to image the liver in 14 subjects to detect the presence of active and chronic changes in hepatic inflammation and fibrosis [28]. Each scan is 256 $\times$ 256 $\times$ 128 in size; the in-plane resolution is 1.4648 mm; and the slice thickness is 3 mm without a gap.

The imaging protocol consists of one pre-contrast (0 second) and seven post-contrast scans (20 seconds: arterial phase; 1 minute: portal-venous phase; 3 minutes: equilibrium phase; 5, 10, 15 minutes; 20 minutes: delayed phases or hepatocyte phase) after the administration of gadoxetate disodium (Gd-EOB-DTPA) contrast agent (Eovist; Bayer HealthCare, US) as illustrated in Figure 5. The Eovist is partially taken up by liver cells, thus enhancing healthy liver tissue while lesions with no or minimal hepatocyte function remain unenhanced and thus making this region of liver distinct in contrast uptake over time. Approximately 50% of the contrast agent injected is renally excreted, whereas the other 50% is transported to the liver cells and then excreted via the biliary system [29]. When a contrast agent is injected intravenously, the hepatic arterial system is enhanced during the first pass, whereas only minimal enhancement is registered in the parenchyma. These arterial or presinusoidal phase images (acquired approximately 15-25 sec after injection) are especially important for the detection of hypervascular malignancies of the liver, i.e. lesions which are predominantly supplied by the hepatic artery (HCC, FNH), and provide important information on the character of the lesion. Images of the portal-venous

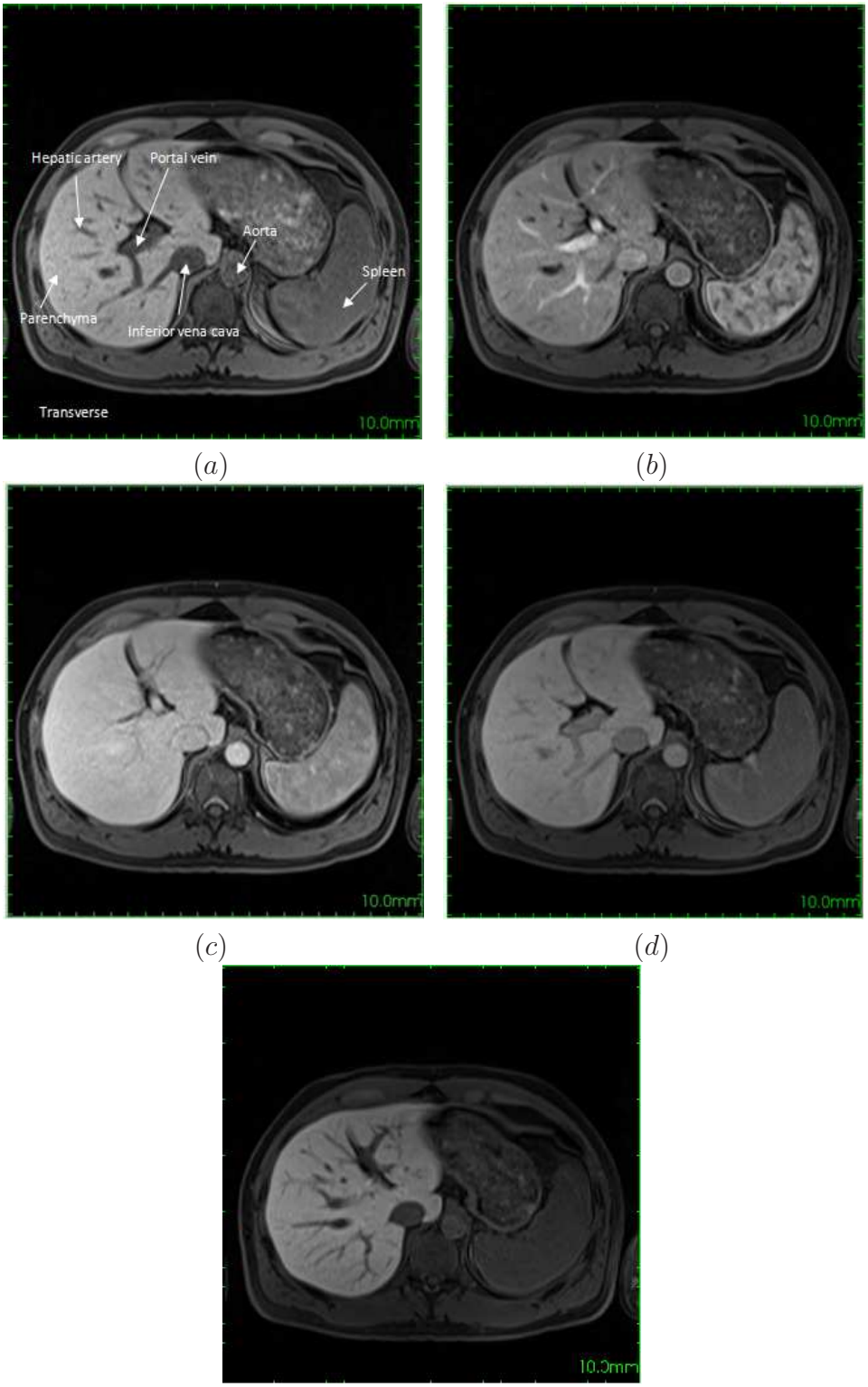

(a) (b) (c) (d) (e)

Figure 5: Liver perfusion: (a) pre-contrast phase (0 second); (b) arterial phase (20 seconds); (c) portal-venous phase (1 minute); (d) equilibrium phase (3 minutes); (e) delayed phase (20 minutes).

phase are acquired approximately 40-70 seconds after administration of the contrast agent, when the portal vein system and the hepatic veins are enhanced. These images show maximal parenchymal enhancement and maximal contrast differentiation between liver and hypovascular lesions. Images of the equilibrium phase are acquired 80-120 seconds after injection of contrast agent when it has already diffused into the interstitium. Contrast enhancement in the equilibrium phase is particularly prominent in edematous tissues, such as neoplasms and areas of inflammation. Images of the delayed phase (or hepatocyte phase) are acquired 20 minutes after injection. It provides additional morphological and functional information about lesion cell composition and increased liver-to-lesion contrast.

CHAPTER III

IMAGE REGISTRATION

3.1 Introduction and Related Works

Liver biopsy has been used as the gold standard for diagnosing liver disease or determining the response to therapy. However, because of its invasiveness and limited spatial localization, image-based, non-invasive methods have been developed to provide flexibility and better spatial coverage. Magnetic resonance imaging (MRI) is the most diagnostically comprehensive modality both for the evaluation of tumors and for the analysis of changes related to diffuse liver diseases, including accumulation of fat, iron or fibrotic changes related to chronic liver disease. One of the vital elements of liver MRI involves administration of a contrast agent followed by dynamic imaging to obtain dynamic enhancement information on liver tumors and diffuse liver disease characteristics. During the dynamic imaging, however, the liver moves and deforms due to voluntary and involuntary motion. The removal of motion artifacts is essential to obtaining accurate diagnostic information of the liver. A standard approach for dynamic liver imaging is to register post-contrast scans to the pre-contrast scan. The execution time of motion correction is an important factor to consider in practice since post-contrast liver MR image sequences typically consist of several scans, and motion correction for these scans needs to be completed within a few minutes for time-sensitive clinical applications.

In contrast to voluntary motion that can be corrected by simple rigid body motion correction algorithms, involuntary motion is subject to a limitation for employing suitable methods because of the lack of image features or landmarks in the liver MRI. Consequently, landmark-based parametric registrations are not available. Image

intensity-based parametric registrations using uniform or user-supplied control point grid with cubic B-spline or thin-plate spline radial basis expansion can have sensitive registration results. This is because there can exist local minima of similarity measure surrounding control points ([30, 31, 7, 32]). And computation time depends on the space of control point grid. Therefore, to overcome these drawbacks we will propose novel accelerated version of local correlation coefficient based demons algorithm satisfying accuracy and efficiency among various non-parametric algorithms.

3.2 Translation-only Rigid Motion Correction

Prior to applying a non-rigid registration, we employed a simple rigid registration scheme that inputs a starting translational transformation estimate T_0=$\{t_x, t_y, t_z\}$, and assumes that the transformation quantity is within the capture range of a registration measure. We evaluated the chosen similarity measure, normalized cross correlation (NCC), for a set of seven transformations $\mathbf{T}(T_0)$. We compared the starting estimate with increments and decrements of each of three translations in three-dimensional space. Then, the maximum of similarity measures among the set of seven transformations determined the next optimal transformation, T_1. The search for $\mathbf{T}(T_{n+1})$ was repeated until the similarity measure yielded no improvement. With coarse-to-fine strategy, more detailed optimization were performed with decreasing the step size–$[5, 2, 1]$ voxels in order.

3.3 Bi-directional Local Correlation Coefficient Demons

3.3.1 Local Correlation Coefficient Demons

Under the assumption that intensities of images are preserved during motion, the demons algorithm, based on the sum of squared differences (SSD) criterion, has been used for matching images. However, as pointed above, SSD is inappropriate for the case of images whose intensities are evolving, but correlated. For this reason, we used a local correlation coefficient (LCC) demons algorithm, introduced by [33], for

registering locally and affinely contrast-changing images. The LCC is defined as the sum of correlation coefficients centered at voxel p such as

$$LCC(S, M) = \sum_{p \in N^n} CC_p(S, M), \tag{18}$$

where $CC_p(S, M)$ is

$$CC_p(S, M) = \frac{\langle S, M \rangle_p}{\sigma_p(S)\sigma_p(M)}. \tag{19}$$

During the calculation of $CC_p(S, M)$, a Gaussian window (σ_{CC}) was used to weigh the voxels in the neighborhood of voxel p. Its isotropic and gradually decreasing weights from the center facilitates the computation of the local statistics–a local mean and a local variance–centered at voxel p. This computation is accomplished by a convolution with the Gaussian kernel as follows:

$$\overline{S}_p = (G_{\sigma_{CC}} * S)[p], \ \overline{M}_p = (G_{\sigma_{CC}} * M)[p] \tag{20}$$

$$\sigma_p^2(S) = \overline{S^2}_p - \overline{S}_p^2 = G_{\sigma_{CC}} * (S^2)[p] - (G_{\sigma_{CC}} * S)^2[p] \tag{21}$$

$$\sigma_p^2(M) = \overline{S^2}_p - \overline{M}_p^2 = G_{\sigma_{CC}} * (M^2)[p] - (G_{\sigma_{CC}} * M)^2[p] \tag{22}$$

$$\langle S, M \rangle_p = \overline{SM}_p - \overline{S}_p\overline{M}_p \tag{23}$$

$$= G_{\sigma_{CC}} * (SM)[p] - (G_{\sigma_{CC}} * S)[p](G_{\sigma_{CC}} * M)[p]. \tag{24}$$

In the SSD-based demons process minimizing the SSD between S and M, at each iteration the displacement incremental field becomes

$$u_{SSD} = \frac{(S(x-u) - M(x))\nabla S(x-u)}{(\nabla S(x-u))^\top \nabla S(x-u) + \alpha^2(S(x-u) - M(x))^2} \tag{25}$$

$$= \frac{-2E_{SSD}\nabla E_{SSD}}{(\nabla E_{SSD})^2 + 4\alpha^2(E_{SSD})^2}, \tag{26}$$

where $E_{SSD} = (S(x-u) - M(x))^2$ is a similarity measure at some point and $\nabla E_{SSD} = -2(S(x-u) - M(x))\nabla S$ is the gradient of the similarity with respect to the displacement field at some point. When this framework is applied to the LCC-based demons algorithm, the gradient-descent optimizing framework based on SSD criteria is replaced by the gradient-ascent optimizing framework based on LCC criteria to find its maxima. Thus, E_{SSD} is replaced by E_{LCC} and (-) sign by (+) sign as

$$u_{LCC} = \frac{2E_{LCC}\nabla E_{LCC}}{(\nabla E_{LCC})^2 + 4\alpha^2(E_{LCC})^2}. \tag{27}$$

3.3.2 Bi-directional Scheme

Because uni-directional registration lacks reciprocal consistency and may lead to inferior registration due to the asymmetry of the similarity measure, we introduce a bi-directional (symmetric) LCC demons algorithm by incorporating symmetric registration concept. In general, image registration methods proceed in one direction in which a static image is fixed and a displacement field u is updated for matching a moving image to the static image. Depending on the direction of image registration, the topological transformation would be different because of the asymmetry of a similarity measurement. To overcome the limitation of utilizing one directional force, symmetric image registration treats two images that are equally involved in the registration process by applying Newton's action and reaction law. The symmetric force applied to the moving image is

$$F^M(x) = F_M(x) + F'_S(x), \tag{28}$$

where $F_M(x)$ denotes a force which acts on image M in order to match it with image S, and $F'_S(x)$ denotes a reciprocal force of $F_S(x)$ which acts on image S in order to

match it with image M with $F'_S(x) = -F_S(x)$. Eq. (28) can be rewritten as

$$F^M(x) = F_M(x) - F_S(x). \tag{29}$$

The displacement incremental fields computed from the symmetric LCC demons forces corresponding to F_M and F_S become

$$u_M = \frac{2E_{LCC_M}\nabla E_{LCC_M}}{\|\nabla E_{LCC_M}\|^2 + 4\alpha^2(E_{LCC_M})^2}, \tag{30}$$

$$u_S = \frac{2E_{LCC_S}\nabla E_{LCC_S}}{\|\nabla E_{LCC_S}\|^2 + 4\alpha^2(E_{LCC_S})^2}, \tag{31}$$

where local energies E_{LCC_M} and E_{LCC_S} at p are defined as

$$E_{LCC_M} = E_{LCC_S} = CC_p(S, M) = \frac{< S, M >_p}{\sigma_p(S)\ \sigma_p(M)}. \tag{32}$$

The analytical gradient solutions of E_{LCC_M} and E_{LCC_S} at each point p are derived and are followed by their simplifications by dropping all the Gaussian convolutions as

$$\frac{\partial E_{LCC_M}(x)}{\partial u_{M,p}} = \frac{\partial CC_p(S(x - u_M), M(x))}{\partial u_M} \tag{33}$$

$$= -\Bigg[M_p G_{\sigma_{CC}} * \frac{1}{\sigma_p(M)\sigma_p(S)} - S_p G_{\sigma_{CC}} * \frac{< S, M >_p}{\sigma_p(M)\sigma_p^3(S)} + G_{\sigma_{CC}} * \left(\frac{< S, M >_p \overline{S}_p}{\sigma_p(M)\sigma_p^3(S)} - \frac{\overline{M}_p}{\sigma_p(M)\sigma_p(S)}\right)\Bigg]\nabla S_p \tag{34}$$

$$\approx \frac{-1}{\sigma_p(S)\sigma_p(M)}\left((M - \overline{M}_p) - (S - \overline{S}_p)\frac{< S, M >_p}{\sigma_p^2(S)}\right)\nabla S, \tag{35}$$

$$\frac{\partial E_{LCC_S}(x)}{\partial u_{S,p}} = \frac{\partial CC_p(S(x), M(x-u_S))}{\partial u_S} \tag{36}$$

$$= -\Bigg[S_p G_{\sigma_{CC}} * \frac{1}{\sigma_p(S)\sigma_p(M)} - M_p G_{\sigma_{CC}} * \frac{< S, M >_p}{\sigma_p(S)\sigma_p^3(M)}$$

$$+ G_{\sigma_{CC}} * \left(\frac{< S, M >_p \overline{M}_p}{\sigma_p(S)\sigma_p^3(M)} - \frac{\overline{S}_p}{\sigma_p(S)\sigma_p(M)}\right)\Bigg]\nabla M_p \tag{37}$$

$$\approx \frac{-1}{\sigma_p(S)\sigma_p(M)}\left((S-\overline{S}_p) - (M-\overline{M}_p)\frac{< S, M >_p}{\sigma_p^2(M)}\right)\nabla M. \tag{38}$$

The simplified derivative of correlation coefficient is called SLCC from this point. The mappings of each image coordinate x_M and x_S to a global coordinate X are $X = x_M + u_M(x_M)$ and $X = x_S + u_S(x_S)$. Even though symmetric displacement fields $u_M(x_M)$ and $u_S(x_S)$ in the image coordinates are taken into account, in practice the static image S is fixed, but only moving image M is updated for iterations. To merge $u_S(x_S)$ into $u_M(x_M)$ in the x_M coordinate system, we consider the static image coordinate x_S as the global coordinate X and multiply u_S by the inverse Jacobian of transformation X with respect to x_M, which is then added by $u_M(x_M)$ as shown in Eq. (39). Thus, the displacement incremental field in the global coordinate system is given by

$$u = u_M - J^{-1} * u_S, \text{ where } J = \frac{\partial X}{\partial x_M} = I + \frac{\partial u_M(x_M)}{\partial x_M}. \tag{39}$$

Computing Jacobian matrix for each voxel is computationally expensive. The small scale deformation of in-vivo objects, including the tissue of the liver, are nearly-incompressible due to the high water content ([34, 35, 36, 37, 38, 39, 40, 41]) such that $J = \frac{\partial X}{\partial x_M} \approx I$. Thus, Eq. (39) can be further simplified to

$$u = u_M - u_S \tag{40}$$

$$= \frac{2E_{LCC_M}\nabla E_{LCC_M}}{\|\nabla E_{LCC_M}\|^2 + 4\alpha^2(E_{LCC_M})^2} - \frac{2E_{LCC_S}\nabla E_{LCC_S}}{\|\nabla E_{LCC_S}\|^2 + 4\alpha^2(E_{LCC_S})^2}. \tag{41}$$

3.3.3 Anisotropic Gaussian Filter-based Approach

$$G_\sigma(\vec{r}) = \frac{1}{\left(\sqrt{2\pi}\sigma\right)^3} e^{\frac{\|\vec{r}\|^2}{2\sigma^2}} \tag{42}$$

is a Gaussian smoothing filter with a standard deviation σ. One of disadvantages of the demons algorithm is the absence of constraints on the displacement, and it does not necessarily preserve the topology of the object. To reduce the unsmooth displacement from noise, the displacement field is smoothed by Gaussian filtering. The classical SSD-based demons algorithm presented by [42] included the Gaussian filtering to fluid-like regularize the displacement incremental field (σ_{fluid}) and to diffusion-like regularize the total displacement field ($\sigma_{diffusion}$). And the computation of local correlation in the LCC demons algorithm is also Gaussian filtering based (σ_{CC}). Note that in anisotropic voxel size, the filtering needs to be anisotropic and is obtained when scaling differently in the x-, y-, and z-direction. The directional scaling depends on the physical voxel size (δ_i) in the direction i and is defined as

$$\sigma_i = \frac{\sigma}{\delta_i}, \tag{43}$$

where σ is a standard deviation of the Gaussian filtering. Given anisotropic scalings, we can build three one-dimensional separate recursive filter approximating the Gaussian filter ([43, 44]).

3.3.4 Algorithm

In each iteration, multiple terms (e.g., a local mean and a local variance) are updated to compute displacement incremental fields via Eq. (30) and Eq. (31). The application of the inner Gaussian filter (with σ_{fluid}) is performed using

$$t \leftarrow G_{\sigma_{diffusion}} * \left\{ t + G_{\sigma_{fluid}} * Eq.(41) \right\}, \tag{44}$$

where t_n is the displacement field. The updated deformation or transformation field (i.e., a three-dimensional displacement field added to a three-dimensional regular grid) interpolates the moving image with a tri-linear scheme.

$$M(x) \leftarrow M\left(x + t(x)\right). \tag{45}$$

Steps given by Eq. (41), Eq. (44), and Eq. (45) repeats until the mean of L^2 norm of displacement field is smaller than given threshold, or the iteration reaches the maximum number, in our case 10^{-2} and 150, respectively.

[9] did not describe how one chooses parameters for a given application, which turns out in practice to be a delicate matter ([45]). Based on three-dimensional simulations using mathematically deformed phantom liver images, we found optimized combinations of parameters, α, σ_{CC}, σ_{fluid}, and $\sigma_{diffusion}$ detailed in Section 3.4.1.

3.4 Simulation

The proposed method was evaluated using simulations. Simulated image was obtained by mathematically deforming a phantom image with a characteristic of a divergence-free flow and affinely, locally changing intensities of the phantom image so that it meets the condition of the contrast-enhanced MR image. The deformation follows the divergence-free condition, $div\ u = 0$, from the assumption that liver tissue is nearly incompressible. The assumption is valid over the entire liver volume, including a few extra voxels surrounding the boundary of the liver. The determinant of the Jacobian matrix of the deformation (referred to as Jacobian, J) was set to one assuming volume-preserving or incompressible. [46] expanded the Jacobian as

$$J = det\frac{\partial t}{\partial r} = det(Id + \frac{\partial u}{\partial r}) = 1 + tr\frac{\partial u}{\partial r} + detr_2\frac{\partial u}{\partial r} + det\frac{\partial u}{\partial r}, \tag{46}$$

where $detr_2$ represents the sum of the principal minors. The third and fourth terms of the expansion are negligible compared to the first two terms for a spatially smooth displacement field. Thus,

$$J \approx 1 + tr\frac{\partial u}{\partial r}. \tag{47}$$

Since $tr\frac{\partial u}{\partial r} = div\ u$, and if divergence-free condition is satisfied, Eq. (47) can be expressed as $J = 1$, i.e., the proposed deformation is approximately incompressible.

We used a deformation model satisfying the divergence-free condition as follows: let $\Omega \subset \Re^3$ denote the domain of the model and the center point $(P_x, P_y, P_z) \in \Omega$ move by Δ in the z direction, and let (u_x, u_y, u_z) denote the displacement field.

$$u_x = \Delta \cdot \frac{(x-P_x)(z-P_z)}{x^2+y^2}\left[1 - exp^{-\frac{(x-P_x)^2+(y-P_y)^2}{2\sigma^2}}\right] exp^{(-\frac{(z-P_z)^2}{2\sigma^2})} \tag{48}$$

$$u_y = \Delta \cdot \frac{(y-P_y)(z-P_z)}{x^2+y^2}\left[1 - exp^{-\frac{(x-P_x)^2+(y-P_y)^2}{2\sigma^2}}\right] exp^{(-\frac{(z-P_z)^2}{2\sigma^2})} \tag{49}$$

$$u_z = \Delta \cdot exp^{\left(-\frac{(x-P_x)^2+(y-P_y)^2+(z-P_z)^2}{2\sigma^2}\right)} \tag{50}$$

satisfying $\lim_{(x,y)\to\ (P_x,P_y)} u_x = 0$ and $\lim_{(x,y)\to\ (P_x,P_y)} u_y = 0$ in which σ represents how far the deformation lies from the point (P_x, P_y, P_z). This formula is symmetric and circular for x, y and z axes. For an oblique direction d, let orthonormal vectors $\hat{i}$, $\hat{j}$ and $\hat{k}$ represent the unit vectors of a local coordinate system centered at P where $\hat{k} = \frac{d}{\|d\|}$. For a given point r, the corresponding local coordinates are $x = (r-p)\cdot\hat{i}$, $y = (r-p)\cdot\hat{j}$ and $z = (r-p)\cdot\hat{k}$. By using the local coordinates and $\Delta = \|d\|$, one can evaluate the displacement component given by Eq. (48), Eq. (49), and Eq. (50) and finally obtain the displacement vector at point r as $u = u_x\hat{i} + u_y\hat{j} + u_z\hat{k}$. A way to determine unit vectors $\hat{i}$ and $\hat{j}$ is given by the following algorithm.

(1) Select the minimum of $|k_x|$, $|k_y|$, $|k_z|$. If $|k_x|$ is the minimal, then $\hat{t} = (1, 0, 0)$. If

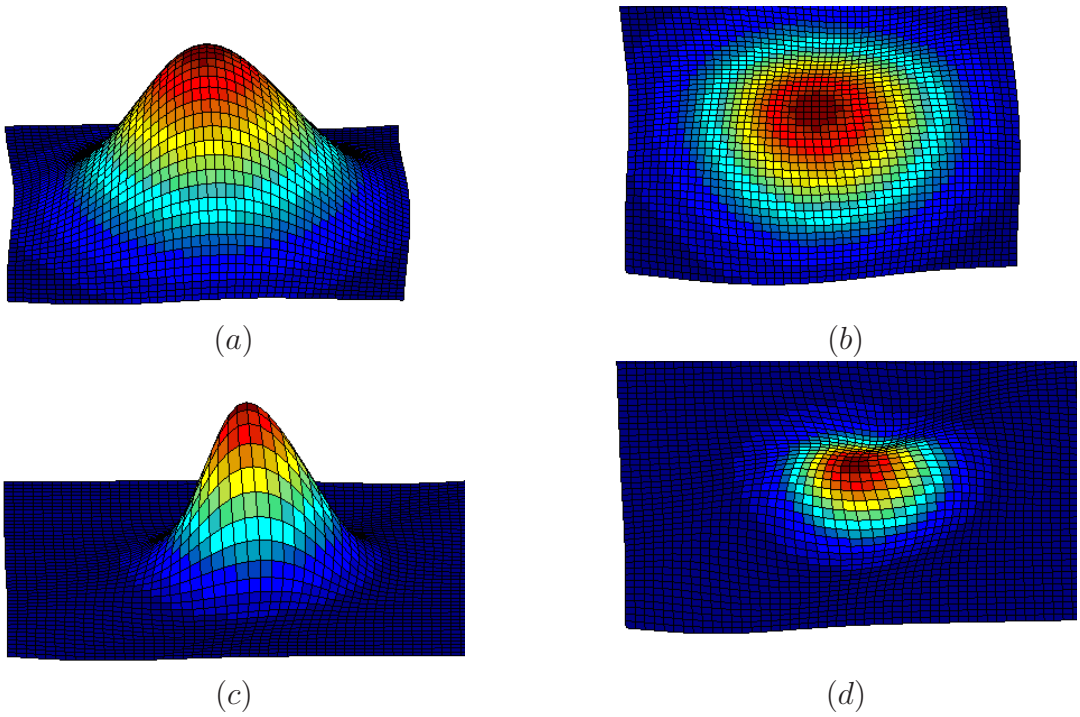

Figure 6: 3-D divergence-free deformation field caused by the center point's movement by $\Delta = 10$ mm in the z direction: global motion with $\sigma = 60$ in (a) and (b), and local motion with $\sigma = 30$ in (c) and (d) are synthesized.

$|k_y|$ is the minimal, then $\hat{t} = (0, 1, 0)$. If $|k_z|$ is the minimal, then $\hat{t} = (0, 0, 1)$.

(2) $\hat{i} = \frac{\hat{t} \times \hat{k}}{\|\hat{t} \times \hat{k}\|}$

(3) $\hat{j} = \hat{k} \times \hat{i}$

The resultant displacement field is divergence-free and is centered at point p. Besides, it points in the direction d and has a magnitude of $\|d\|$ at point p. The Jacobian determinant calculated from the given deformation field deviated from one within $\pm 3\%$, in agreement with the observation of [47]. Figure 6 depicts global and local deformation fields generated by 10 mm movement of the central point in z-direction with scalings of 60 and 30.

Intensities of the liver image scanned at multiple times before and after contrast administration are not preserved due to uptake of a contrast agent within the liver, with patterns, based upon morphology and time-course of the uptake, reflecting specific disease. And inhomogeneities arise from imperfection of static magnetic field

and RF coil. To ascertain the intensity changing relationship between pre- and post-contrast scans, we compared the intensities of pre-contrast and post-contrast scan which was corrected for translation-only motion over the liver parenchyma region x_p. Figure 7 (a) illustrates the fittings of sets of intensities at corresponding voxels for one patient, which is shown affinely correlated. For delayed phase (20 min after injection) of three healthy and three unhealthy patients, multiplicative and additive factors range from 0.56 to 2.25 and from -56 to 136, respectively. To obtain the normalized affine model, mean values are selected as the coefficients of the global intensity changing profile in the liver parenchyma. In addition, local enhancement, which depends on the geometry, is established by a subtraction of the affine model from the real data followed by nonlinear regression to a gamma distribution model as shown in Figure 7 (b). The normalized local enhancement model centered at point r is given as $\hat{I}^{post}(x) = 12.9(||x-r|| + 23.2)^{0.44} exp^{-0.008*||x-r||} - 48.5$, and thereby the total intensity changing profile becomes $I^{post}(x_p) = 1.41 I^{pre}(x_p) + 96 + \hat{I}^{post}(x)$. For the vessels in the liver, hepatic artery and portal vein supplying oxygenated blood to the liver and hepatic vein draining de-oxygenated blood from the liver are segmented separately as seen in Figure 8. The intensity model for the region of hepatic artery and portal vein x_{hp} is deduced as $I^{post}(x_{hp}) = I^{pre}(x_{hp}) + 140 + \hat{I}^{post}(x)$ and for the region of hepatic vein x_v is $I^{post}(x_v) = I^{pre}(x_v) + 100 + \hat{I}^{post}(x)$. The pre-scan image of one normal patient and its deformed image in accordance with above characteristics will be used in the following simulations.

3.4.1 Parameter Optimizations of Uni-LCC Demons

The LCC demons method uses four parameters; α, σ_{CC}, σ_{fluid}, and $\sigma_{diffusion}$, whose specifications are not given in the literature. In this section, we describe how to optimize parameters for the Uni-LCC demons with exact derivative in Eq. 33 based on various comparisons by simulating images.

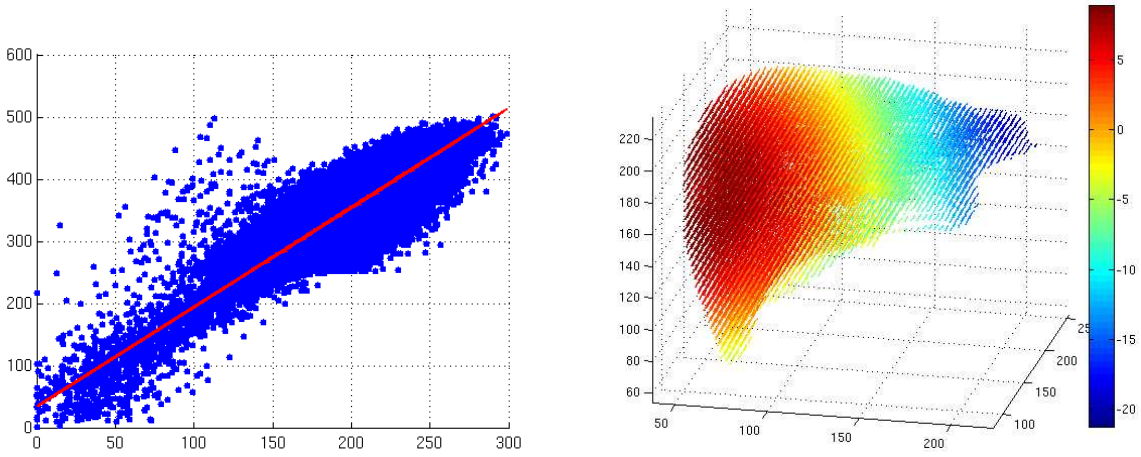

(a) (b)

Figure 7: Global relationship of intensity between pre- and post-contrast scans (a) and local intensity enhancement modeling (b) of the liver parenchyma.

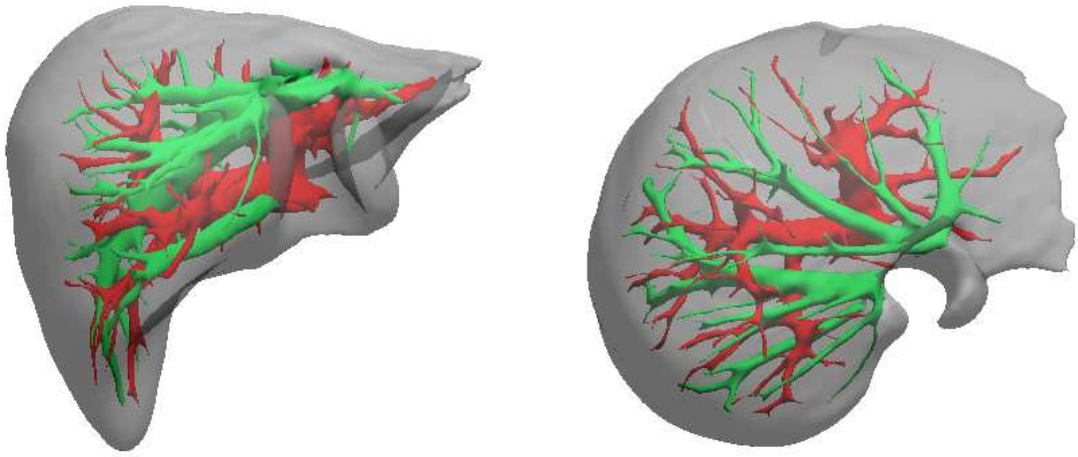

(a) (b)

Figure 8: Vessels in the liver: hepatic artery and portal vein (red); hepatic vein (green) in the front (left) and top (right) views.

The parameter α, which is not present in the original demons formulation ([42]), was introduced by [48], and it was named as a homogenization factor. The purpose of α is to control the maximal displacement, which is bounded by $\frac{1}{2\alpha}$. The term is closely related with how fast the algorithm converges. Note that if α is set very small for the purpose of speed, it can lead to unstable convergence. First, we defined a normalized local correlation coefficient (NLCC) as

$$NLCC = \frac{LCC(S,M)}{n} = \frac{\sum_{p=1}^{n} CC_p(S,M)}{n}, \tag{51}$$

where n is the total number of voxels of which correlation coefficients are computed. Using the phantom simulation image that displaced $\Delta = 10$ mm in the z direction with $\sigma = 60$ mm, NLCCs changes for three possible choices of $\alpha = 0.25, 0.5, 1$, with other fixed parameters, were compared as shown in Figure 9. While the convergence with $\alpha = 0.25$ showed the steepest increase in NLCC in the early state but exposed a lack of stability in the steady state. The NLCC curves at $\alpha = 0.5$ show not only the most stable increase but also the largest convergence. The bigger value $\alpha = 1$ converges with the slower rate. These results are supported by theoretical computation of maximal bound of each case as 2, 1, and 0.5 mm. Since the smallest edge of a voxel is 1.46 mm, slightly smaller bound than the size can thwart both unstability and lagging in the convergence; thus, α was set as 0.5.

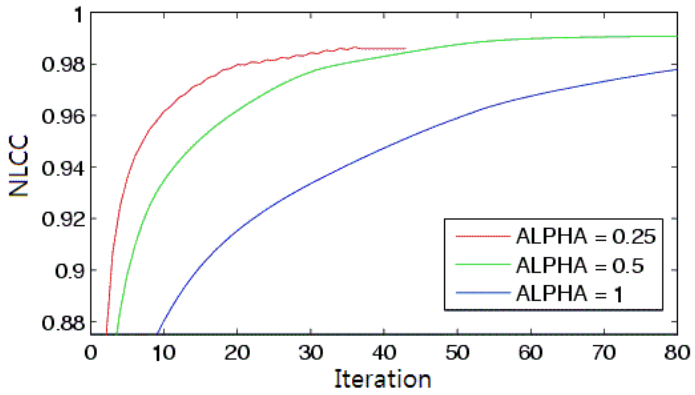

Figure 9: NLCC curves in terms of homogenization factor α.

After the setup of α, we performed tests to search for the optimized σ_{CC} among a set of possible choices $\{1, 2, 3, 4, 5\}$. As a result, NLCCs had values that were very proximate to each other with a difference on the order of 10^{-2}. A mean displacement error (MEANE), which is the root mean square between the true and estimated displacements, was used for optimization of remaining parameters, assuming that MEANE must be close to zero. While we optimized σ_{CC}, the parameters σ_{fluid} and $\sigma_{diffusion}$ were set to 3. According to the results in Table 2, $\sigma_{CC} = 2$ mm recovered the deformation field with the least MEANE. Note that if the image is affected by motion artifacts or pathologic severity, suitably larger σ_{CC} will give more stability to the computed local statistics.

Table 2: Mean displacement error in terms of σ_{CC}.

σ_{CC}	**1**	**2**	**3**	**4**	**5**
MEANE (mm)	**0.319**	**0.303**	**0.335**	**0.377**	**0.428**

Next, the scaling parameters σ_{Fluid} and $\sigma_{Diffusion}$ of the spatial smoothing filters were determined. Due to analogous roles of two filterings, optimization was not separately performed, but finite and suggestive candidates for remaining parameters were evaluated with the fixed σ_{CC}. Among the permutations of $\{3, 4, 5\}$, $\sigma_{CC}/\sigma_{Fluid}/\sigma_{Diffusion} = 2/5/3$ mm produced the lowest MEANE as shown in Table 3.

Table 3: Mean displacement error in terms of combinations of σ_{Fluid} and $\sigma_{Diffusion}$ with the fixed σ_{CC} of 2.

$\sigma_{Fluid}/\sigma_{Diffusion}$	**3/3**	**3/4**	**3/5**
MEANE (mm)	**0.306**	**0.337**	**0.418**
$\sigma_{Fluid}/\sigma_{Diffusion}$	**4/3**	**4/4**	**4/5**
MEANE	**0.296**	**0.333**	**0.417**
$\sigma_{Fluid}/\sigma_{Diffusion}$	**5/3**	**5/4**	**5/5**
MEANE	**0.290**	**0.329**	**0.416**

3.4.2 Exact LCC Demons vs. Simplified LCC (SLCC) Demons

The CC derivative in Eq. (33) was simplified to reduce computation complexity. In the previous study by [33], the authors mentioned SLCC performs slightly better than LCC in the tests of brain MRI, which was contrary to their prediction. In this section, we will confirm the influence of the derivative simplification in liver MRI. The qualitative measurement is to inspect the overlap between the reference and estimated vessel masks recovered by registration. The quantitative measurement is to assess the MEANE and volume of error (VOE) defined as

$$\text{VOE } (\%) = 100 \cdot \left(1 - \frac{V_S \bigcap V_R}{V_S \bigcup V_R}\right), \tag{52}$$

where V_S is the estimated volume mask and V_R is the reference volume mask. The measurements are evaluated separately for each of hepatic vein (VOE_v), hepatic artery with portal vein (VOE_{hp}), and parenchyma (VOE_p). In Figure 10, the left two columns compare the performance between the Uni-LCC demons and Uni-SLCC demons algorithms. The areas pointed by arrows, in which the simplified version cannot recover as much as the exact version, show the difference clearly. In Table 4, the Uni-LCC yielded better performance by an average MEANE of 0.085 mm, VOE_v of 2.75%, VOE_{hp} of 2.6%, and VOE_p of 0.3% than the Uni-SLCC. The comparison in opposite-directional registration showed the similar tendency. For computation time, the Uni-LCC took 7.2 seconds, but the Uni-SLCC 4.3 seconds. Thus, the simplification of the CC derivative sacrifices accuracy to some degree in the case of liver MRI simulation, with the reduction of computation time by 40%.

3.4.3 Contribution of Bi-directional Scheme

In this section, the influence of bi-directional scheme on the performance of LCC demons algorithm is discussed. Tests were performed on the Uni-LCC demons, inverse

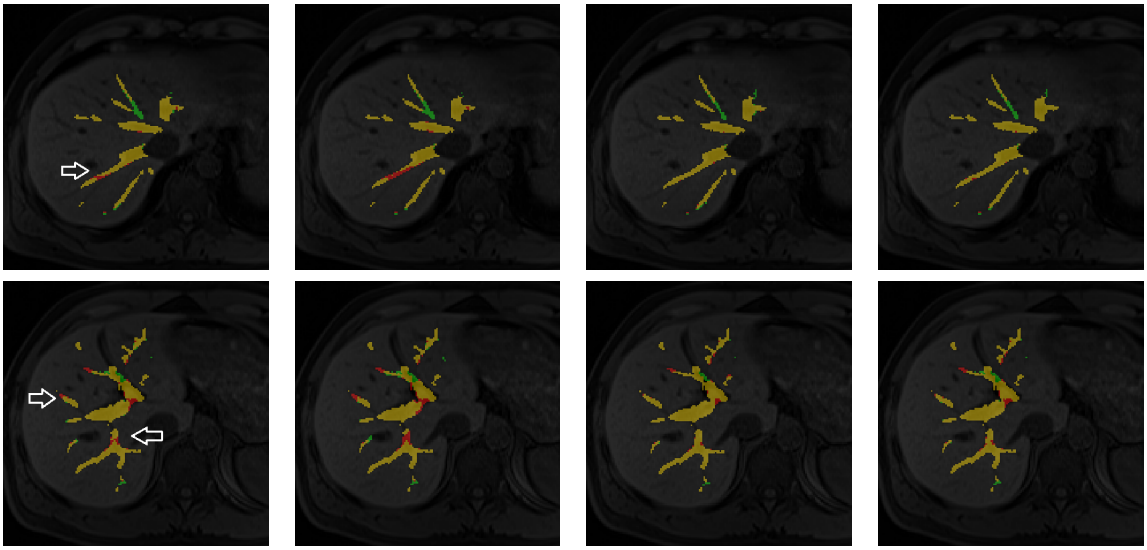

(a) (b) (c) (d)

Figure 10: Visual inspection of registration on hepatic vein (top) and combined hepatic artery and portal vein (bottom) using (a) exact Uni-LCC demons, (b) simplified Uni-LCC demons, (c) exact Bi-LCC demons, and (d) simplified Bi-LCC demons. Overlap of reference and estimated masks (yellow), only reference mask (red), and only estimated mask (green) are indicated. Note the difference in the area pointed by arrows.

Table 4: Quantitative results of simulations with (a) global and (b) local deformation: mean displacement error and volume error in hepatic vein, combination of hepatic artery and portal vein, and liver parenchyma. An asterisk indicates registration in the opposite direction.

	Uni-LCC	Uni-SLCC	Uni-LCC*	Uni-SLCC*	Bi-LCC	Bi-SLCC
MEANE (mm)	0.366	0.461	0.299	0.392	0.298	0.338
VOE_v (%)	11.6	14.3	9.8	12.6	8.1	8.8
VOE_{hp} (%)	11.9	15.0	10.2	13.7	8.0	9.4
VOE_p (%)	0.8	1.1	0.9	1.1	0.8	1.0

(a)

	Uni-LCC	Uni-SLCC	Uni-LCC*	Uni-SLCC*	Bi-LCC	Bi-SLCC
MEANE (mm)	0.428	0.503	0.403	0.488	0.324	0.378
VOE_v (%)	18.5	21.3	17.6	20.9	13.0	14.9
VOE_{hp} (%)	17.7	19.8	16.7	19.4	12.7	14.3
VOE_p (%)	1.2	1.5	1.5	1.7	1.0	1.4

(b)

Uni-LCC demons, and Bi-LCC demons, with their simplified versions. With the unidirectional method, we checked both directions of registration. On the grid recovery in Figure 11, the Bi-LCC demons algorithm leads to closer matching than the Uni-LCC demons algorithm. In this grid, the maximum displacement error was measured: the Uni-LCC demons method produced 2.216 mm, which is larger than the average voxel size 1.976 mm; the Bi-LCC demons algorithm yielded 1.395 mm, which is a subvoxel size. As for registration of vessels in Figure 10, the Bi-LCC demons and its simplified version improved vessel recovery rather than the Uni-LCC demons. Table 4 shows that the Bi-LCC demons exhibited improvements by an average MEANE of 21%, VOE_v of 4.5%, VOE_{hp} of 4.45%, and VOE_p of 0.1%, in the global and local deformations, compared to the Uni-LCC demons. For reference, note that the visual differences between the Bi-LCC and Bi-SLCC methods are not as noticeable as the Uni-LCC and Uni-SLCC methods.

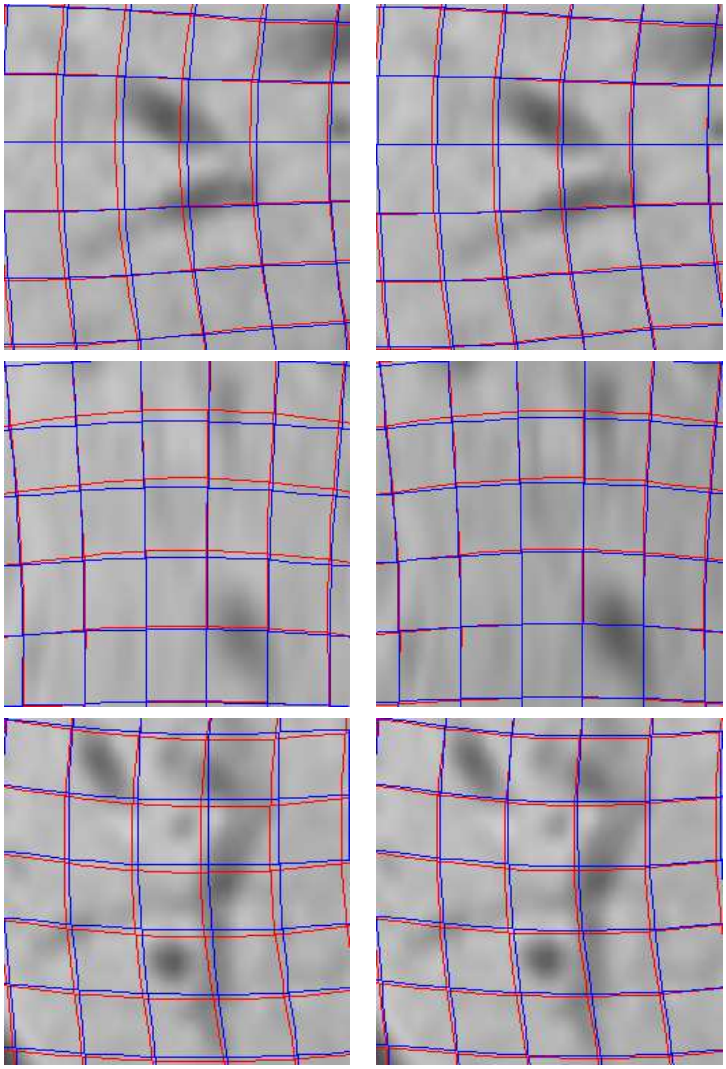

Figure 11: Grid comparisons between the true deformed grid (red curve) and estimated deformed grid (blue curve) from methods by the Uni-LCC demons algorithm (a), and by the Bi-LCC demons algorithm (b) for three local regions.

Figure 12 presents a comparison of computational efficiency. Up to the convergence, the Uni-LCC demons algorithm iterated 79 times while the Bi-LCC demons algorithm iterated 45 times. And their respective simplified versions iterated 91 times and 52 times, which was reduced by 43%. As for the runtime per iteration, the uni-scheme and the bi-scheme consumed 7.2 seconds and 9.8 seconds, and the simplified ones consumed 4.3 seconds and 4.4 seconds, respectively. So, if taking the runtime

per iteration into account for computing the entire runtime, as one of Uni-LCC was assumed 1, the Uni-SLCC was 0.69, the Bi-LCC was 0.78, and the Bi-SLCC was 0.40. Thus, the Bi-SLCC reduced the runtime by 60%.

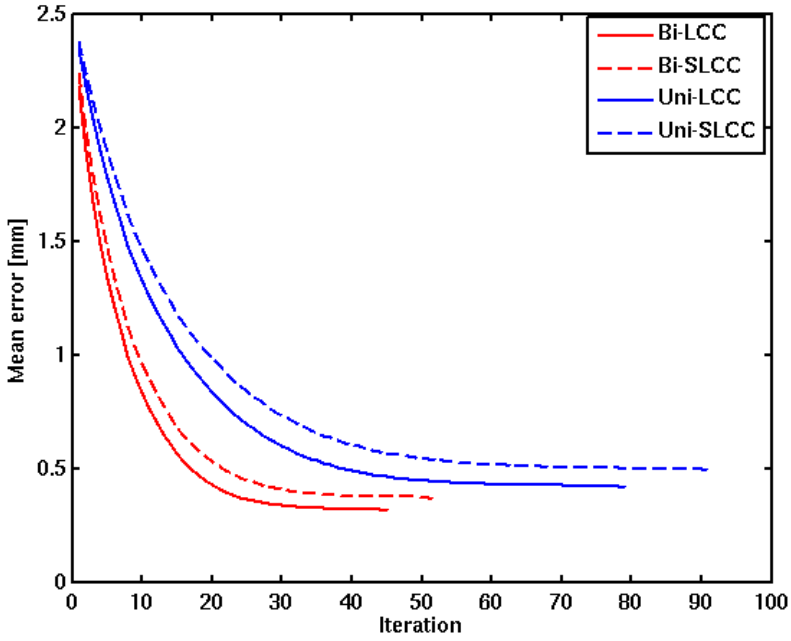

Figure 12: Comparison of the convergence rate among the Uni-LCC, Bi-LCC, and their simplified versions.

3.5 Application to Patient Data

We compared a boundary matching of pre- and post-contrast images registered by the Uni-LCC and Bi-LCC demons, respectively. A checkerboard, which shows alternate squares from two images, was used for assessing the quality of the boundary matching. Figure 13, the boundary mismatching of the Uni-LCC demons was found mainly around the left lobe of the liver, the ends of superior, and inferior regions. However, the Bi-LCC demons resulted in good boundary matching. The results from the simplified versions were not shown here because there is no distinct difference from the exact versions in the checkerboard.

A misalignment of vessel branch points or critical surface points was measured. As shown in Figure 14, with the fixed reference points in the pre-contrast image,

their correspondences in the registered images were identified for each patient. The points evaluated were located in the sharp edge of the left lobe, the crack between the left and right lobes, or the vessel branch. The mean of the L^2 misalignment error measured 2.17 mm in the Bi-LCC demons, but 7.44 mm in the Uni-LCC demons.

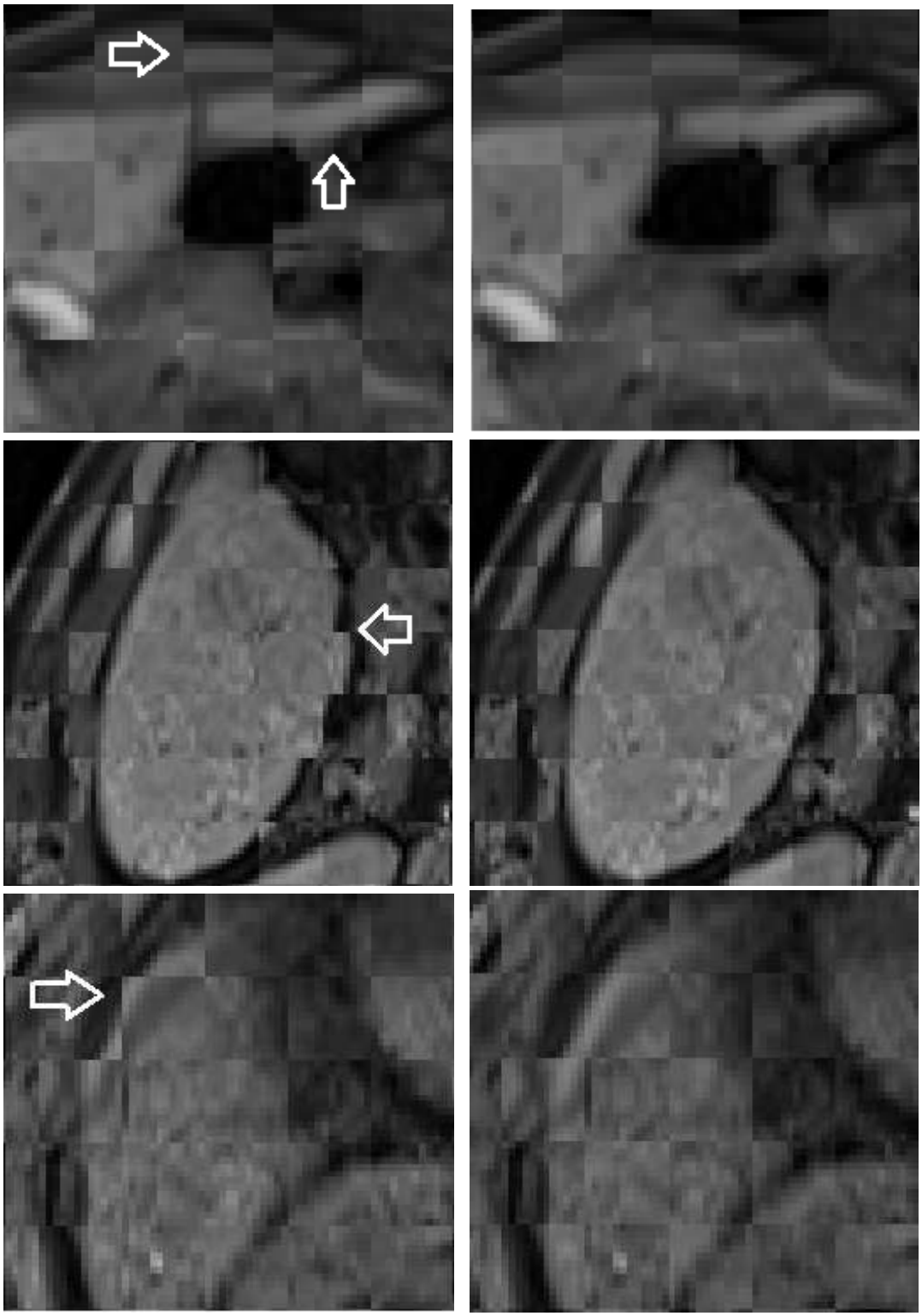

(a) (b)

Figure 13: Comparison of checkerboard between (a) the Uni-LCC and (b) Bi-LCC demons. The arrows distinguish the difference well. The boundary matching degree of the pre- and registered post-contrast images is visually inspected.

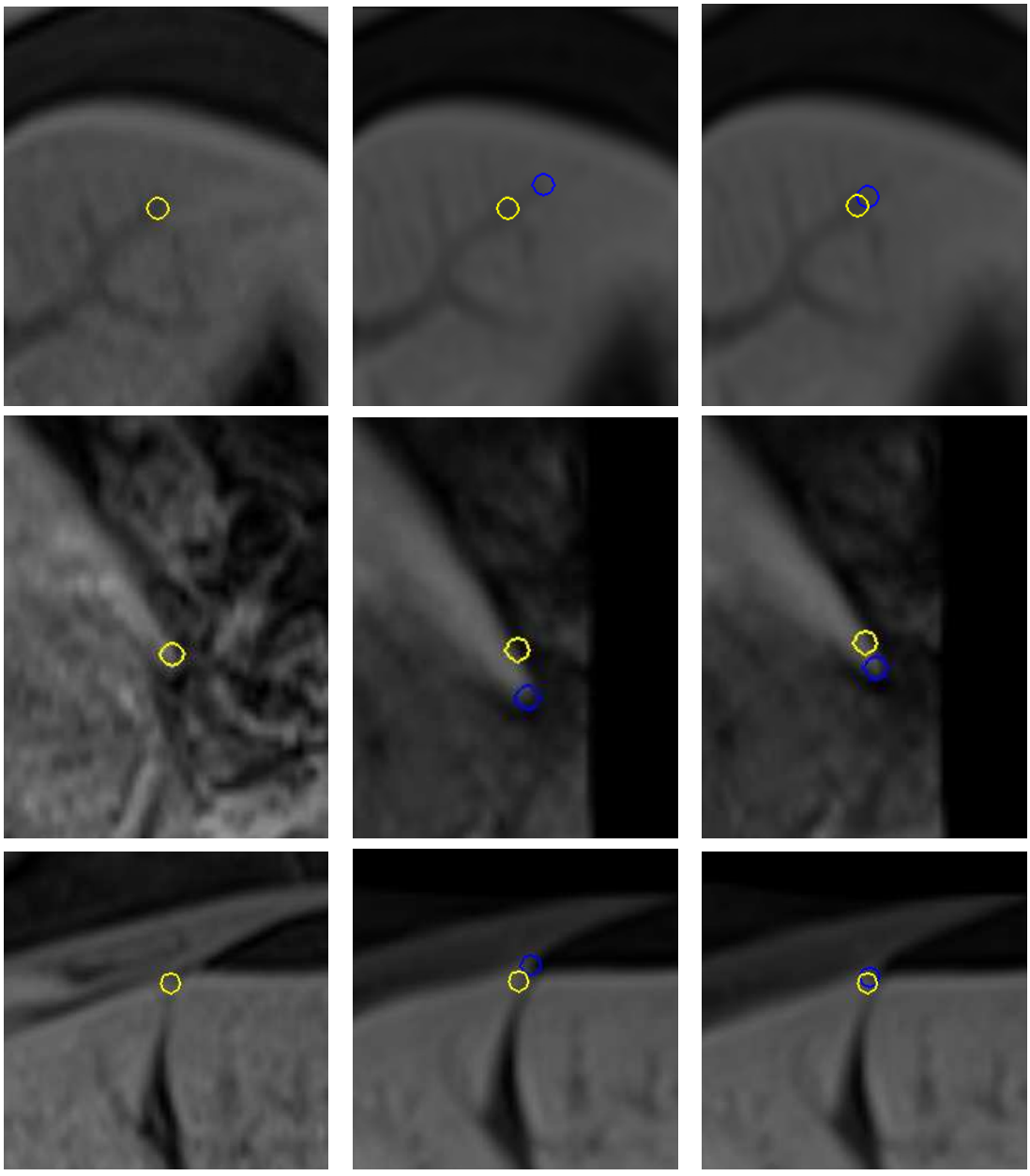

(a) (b) (c)

Figure 14: Misalignment of vessel branch points or critical surface points: the reference points (yellow) and the corresponding points (blue) in reference image (a); registered image by the Uni-LCC demons (b); registered image by the Bi-LCC demons (c).

Myriad studies in the past have ascertained hepatic motion in various ways. We also analyzed hepatic motion resulting from the translation-only and Bi-LCC demons methods for each patient as shown in Figure 15: average shift of 4.5±1.7 mm in the

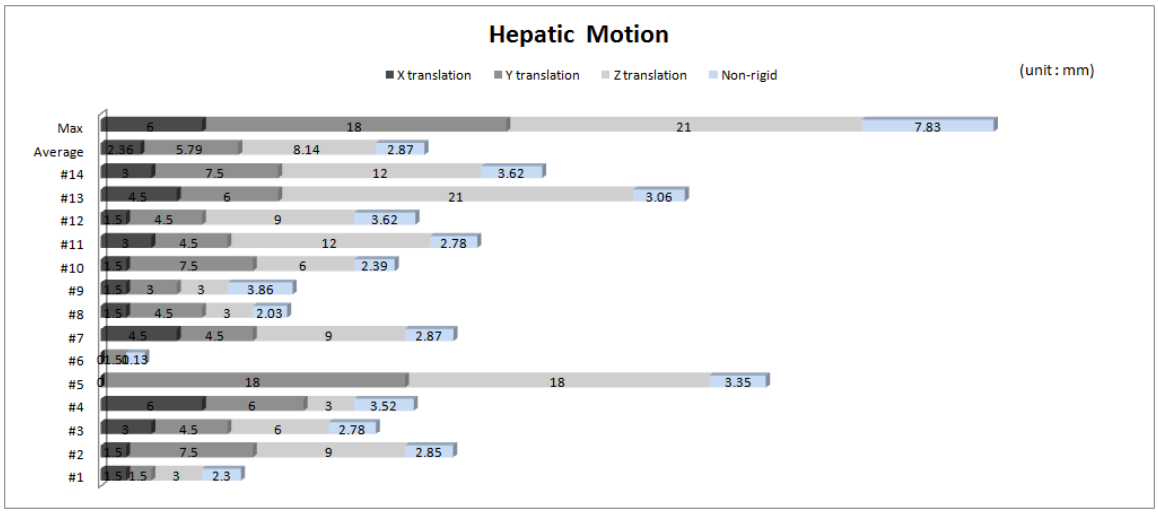

Figure 15: Hepatic rigid and non-rigid motion for 14 subjects.

lateral, 7.5±4 mm in anterior-posterior, and 18±6 mm in cranio-caudal directions. These sizes of hepatic rigid motion agree with the estimates from previous studies by [5] and [6] to some extent. Non-rigid registration by Bi-LCC demons algorithm resulted in maximum motion of 7.83 mm and an average motion of 2.87±0.7 mm. These values are approximately similar with the previous result, 3 mm reported by [6] and [7]. It is worth noting that the liver can move locally as much as 10 mm, justifying the use of 10 mm displacement in the simulation.

3.6 Graphics Processing Unit (GPU)-based Implementation Using OpenCL

In contrast to other registration algorithms, Bi-LCC demons algorithm is computationally fast enough on the order of sub-hour that they need to be executed in less than a minute for clinical use. A graphics processing unit (GPU) normally has 100+ processing elements (scalar cores), large on-board memory space (1+ GB), and a high bandwidth (25+ times faster than the bandwidth between a central processing unit (CPU) and main memory) in a data transfer. Because of highly parallel structure, the GPU device has been applied to general numerical processing beyond graphics issues. The image registration field is also not an exception from adaptations of GPU.

For example, in [49, 50], the authors studied a compute unified device architecture (CUDA) implementation of an original demons algorithm. However, a limitation of CUDA is that it is platform, vendor, or hardware-specific while open computing language (OpenCL) provides a capability of a diverse mix of parallel CPUs, GPUs, and other processing units [51].

OpenCL implements a relaxed version of the data parallel programming and implicit model: a programmer specifies the size of workitems in a workgroup and the size of total workitems. The division into workgroups is automatically managed by the OpenCL implementation. Figure 16 illustrates the system of MR liver image registration using GPU which consists of the two programs, "translation-only registration" and "Bi-LCC demons algorithm," and each program has kernels necessary for its implementation.

Input images such as segmented, fixed, and moving images are written into the buffers in the global memory of the device. The output image of each program is saved back to the host memory. Note that the rigid-body transformed moving images are additionally written into image objects for utilizing hardware interpolation.

A few main techniques applied to our method facilitate the use of well developed GPU resources: pre-compilation, hardware interpolation, and parallel reduction operation. First, in contrast to CUDA in which programs are compiled with an external tool before execution, the OpenCL compiler is invoked at runtime. To pre-compile OpenCL, programmers can use the clGetProgramInfo() API call to retrieve a compiled binary and save it for later use. Then, along with the clCreateProgramWithBinary() call, we can create an OpenCL program object directly from the pre-compiled binary. Second, an image object is used to store a two- or three-dimensional texture, frame-buffer, or image. The built-in image function, "read_imagef," reads a sampled or interpolated value at a non-integer coordinate of the image object with either a nearest neighbor or a linear option. In the kernel, after elements of input are read

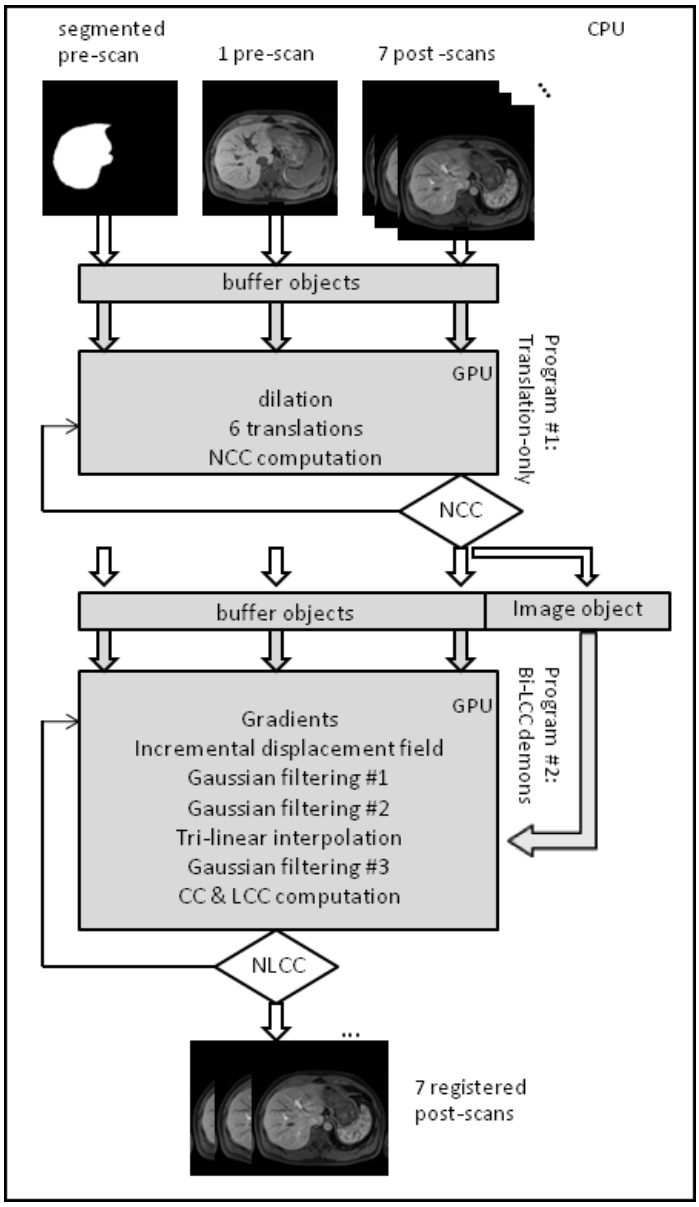

Figure 16: GPU-based liver image registration system.

from the image object, their hardware-interpolated elements are written back to the buffer object, which stores the updated elements of the moving image. Third, when reducing an array of values to a single value in parallel such as NCC or SLCC, the strategy of parallel reduction is very important for effective processing. The details about conflict-free sequential addressing and complete unrolling techniques involved

in parallel reduction are presented in software development kit (SDK) guides provided by NVIDIA corp. In addition, page-locked memory transfers attain the highest bandwidth (+5 GB/s) between a host and a device, and cached memory (constant or texture memory) is useful for storing frequently-loaded and small data such as Gaussian kernels.

Including our GPU, the mobile GPU models before the Fermi architecture of NVIDIA or 6xxx level of ATI do not support a double precision floating-point format. We will validate the use of a single precision floating-point datatype only available in our GPU throughout a comparison of resulting displacement fields using the single and double datatype. Hardware interpolation offered by GPU will be also confirmed. The computer used in the test is ASUS Notebook with Intel Core2 Duo CPU P8700 @ 2.53GHz and 6 GB of main memory in Window 7. The NVIDIA GTX 260M mobile GPU supporting OpenCL 1.0 and compute capability 1.1 is integrated. The GPU has 14 compute units (multi-processors) with 8 processing elements (scalar cores) each, or 112 processing elements in total and a performance of 462 GFLOPS. The programming tool is Microsoft Visual Studio 2008 in which C/C++ programs were built in a release mode.

As shown in Figure 17, the mean and maximum errors from the known displacement field are smaller than or equal to the average of voxel size, 1.98 mm. And the local deformation has a larger error since three parameters in the Bi-LCC demons algorithm are optimized to be fitted into the globally deformed situation. In Figure 18, a comparison with the result using the CPU double datatype exhibited that the float datatype with the hardware interpolation in the GPU exhibits slightly bigger, but an allowable error than the algorithmic interpolation in the CPU with the runtime reduction by 16.1%.

Table 5 illustrates the contribution of each technique introduced for the speedup

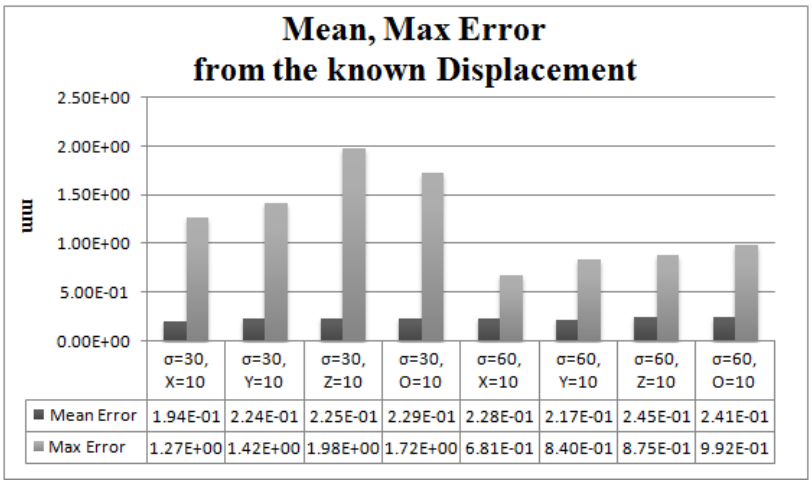

Figure 17: Simulation results: the mean and max error in the resulting displacement from the known displacement satisfying divergence-free condition are specified for eight cases.

of GPU implementation using real liver subjects. Above all, we can notice the significance of parallel reduction in which all work-items need to be busy and escape data conflict. Table 6 indicates that the GPU implementation outperforms the CPU implementation by approximately 50 times in computation time. For GPU, it measures 1.76 sec for translation-only registration and 56 sec for Bi-LCC demons registration, i.e. 57.76 sec for one postscan and 6.7 minutes for seven postscans. On the other hand, for CPU, it measures 4.03 sec for translation-only and 46.5 minutes for Bi-LCC demons registration, i.e. 46.5 minutes for one post-scan and 5.4 hours. Note that the Gaussian filtering is the most expensive process because this kernel has the most GFLOP per iteration. In particular, the kernel of gradient computation has a relatively subnormal factor, for the kernel has an if-statement checking boundary, and the divergent branches inside warps interfere a fast data flow on the GPU. The visual inspection through a checker board display was performed as shown in Figure 13. The arrows point out the biggest changes between before and after translation-only registration and Bi-LCC demons registration to the real liver subject.

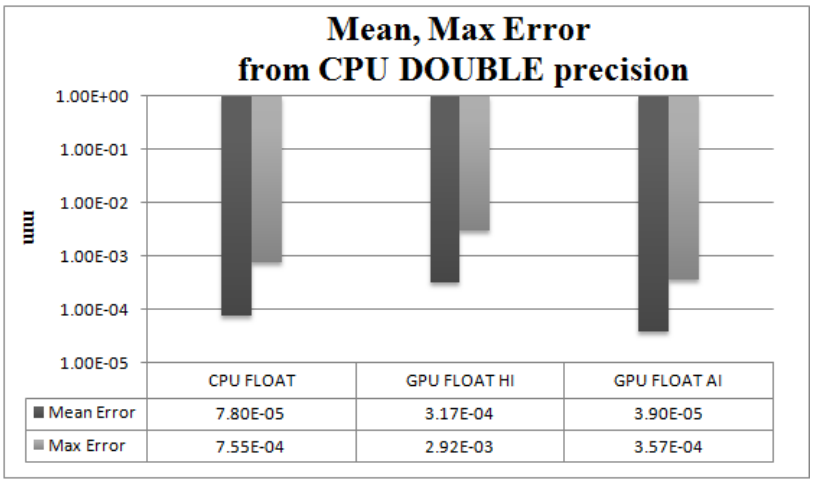

Figure 18: Simulation results: the precision error resulted from the use of float datatype and hardware interpolation in GPU implementation is negligible.

Table 5: Speedup factors as each technique is employed over one unemployed in GPU programming.

GPU resources	Speedup Factor (%)
Pre-compilation	3.7
Hardware interpolation	16.1
Parallel reduction	51.2

Table 6: The comparison of the run time for each kernel in CPU vs. GPU.

Run time	CPU(sec)	GPU(sec)	Speedup(x)
Gradient	0.28	0.029	9.7
Incremental displacement	1.03	0.013	79.2
Three Gaussian filterings	21.79	0.36	60.5
Tri-linear interpolation	1.62	0.039	41.5
LCC\SLCC	0.32	0.0060	53.3
Miscellaneous (Multply, Add, ...)	2.90	0.11	25.7
One iteration	27.94	0.56	49.9
100 iterations	46.5 min	56 sec	50.0
Translation-only	4.03 sec	1.76 sec	2.3

3.7 Conclusion

We have presented a bi-directional local correlation coefficient (Bi-LCC) demons method for motion correction of contrast-enhanced liver MRI with the potential for clinical applications. With three-dimensional simulations using mathematically manipulated phantom images, we optimized the four parameters of the LCC demons algorithm, α, σ_{CC}, σ_{fluid}, and $\sigma_{diffusion}$, from some sets of available alternatives. By introducing a bi-directional scheme, the Bi-LCC demons, compared to the uni-directional LCC demons and simplified versions, could achieve faster convergence to the steady-state and higher accuracy such that the average error is subvoxel size. In applying this method to 14 clinical MRI studies, the performance was verified using a checkerboard and quantifications such as a misalignment of vessel branch points or critical surface points.

3.8 Liver 2D Histology – 3D MR Image Registration

It is important to adjust for non-uniformity of disease severity throughout the liver; characteristically the liver shows marked regional differences in disease severity within individual patients. To improve the accuracy in correlation between pathologic tissue evaluation on specimens obtained from different regions of the explanted whole liver, representing different degrees of CLD severity, and ROIs of MR image, it is desirable to find the corresponding oblique and warped plane in a MR volume within allowable error range. Figure 19 illustrates two different modalities and dimensions of the liver image to be considered in this part. The reasons why this task is challenging are as follows:

1. Correlating in vivo liver MR images with histology images of the sectioned explanted liver is difficult since the liver geometry changes dramatically when the flexible liver is no longer supported by its surrounding anatomic structures. Additional

deformations occur because of the loss of tissue distension from blood pressure and tissue relaxation when the liver specimen is cut [52].

2. The histology image has only in-plane pixel information (2D) in contrary to MR image that has both in-plane and out-of-plane pixel information (3D). In addition, the physical scales (sizes) of pixel in the histology image are unknown in contrast to MR image.

3. Finding the correspondence in intensities or anatomical structures between two modalities is so indefinite in image processing perspective that we can not apply multi-modality image registration by a maximization of mutual information or object feature-based registration.

However, in spite of these obstacles, the liver boundary shape and a set of point landmarks selected by experts can be used for matching the 2D histology to the 3D MR image.

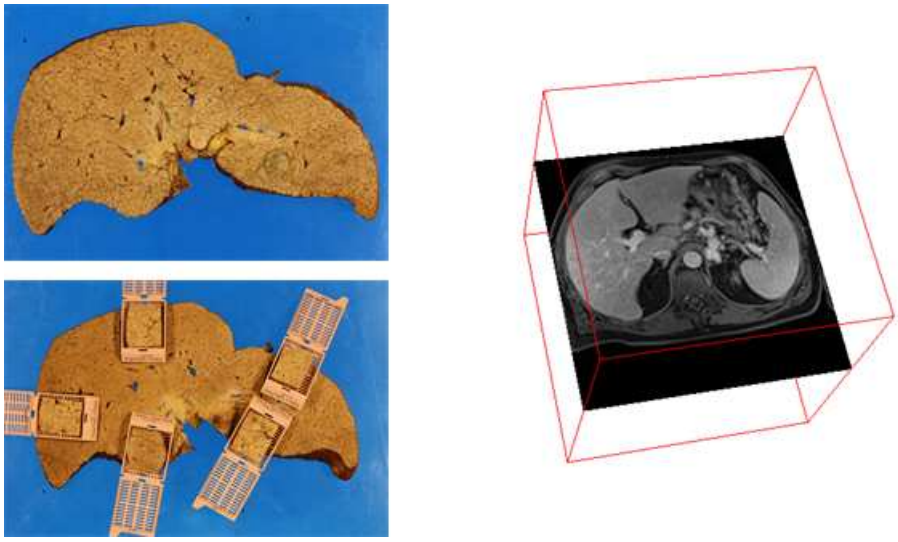

Figure 19: Liver 2D histology image and 3D MR image volume of one subject.

3.8.1 Initialization by Similarity Transformation

Using our developed software as shown in Figure 20, we get similarity transformation matrix S, based on a given set of manually selected point landmarks between the 2D

histology image and the 3D MR image. We assume that the grid in the 2D histology image is homogeneous and regular, and all the z coordinates in the 2D histology image are zero. Similarity transformation, including uniform scale, rotation, and translation, is used as the initialization step for nonrigid registration to find the closest solution. The closed-form solution for the transformation parameters that optimally aligns two point sets in the least squares sense was introduced in [53]:

$$S(\vec{r}) = sR \cdot \vec{r} + \vec{t}, \tag{53}$$

where $S(\vec{r})$ denotes the similarity transformation of $\vec{r}$, s the uniform scale scalar, R the rotation matrix, and $\vec{t}$ the translation vector. Once the elements of similarity transformation are computed, the initial similarity transformed grid that matches each pixels of histology to MRI can be obtained. For convenience when computing directional gradients, we build the similarity transformed 3D MR image volume by stacking slices parallel to the 2D initial transformation grid under assumption that the slice thickness of the histology image is homogeneous with the in-plane pixel size. We consider the original coordinate system of MR image volume as a world coordinate system (WCS) and the similarity transformed coordinate system of MR image volume as a local coordinate system (LCS).

At the final step to generate the non-rigidly registered image, to escape the rescaling error existent in the similarity transformed 3D MR image volume, the transformation field in the LCS must be converted to one in the WCS for using the original MR image volume. The way to recover the transformation field in the WCS is as follows:

Figure 20: A software to help experts to extract point landmarks.

$$\begin{bmatrix} x' \\ y' \\ z' \\ 1 \end{bmatrix} = S_h \cdot \begin{bmatrix} x \\ y \\ z \\ 1 \end{bmatrix} = T_h \hat{S}_h R_h \cdot \begin{bmatrix} x \\ y \\ z \\ 1 \end{bmatrix} = \begin{bmatrix} 1 & 0 & 0 & t_x \\ 0 & 1 & 0 & t_y \\ 0 & 0 & 1 & t_z \\ 0 & 0 & 0 & 1 \end{bmatrix} \begin{bmatrix} s & 0 & 0 & 0 \\ 0 & s & 0 & 0 \\ 0 & 0 & s & 0 \\ 0 & 0 & 0 & 1 \end{bmatrix} \begin{bmatrix} r_{11} & r_{12} & r_{13} & 0 \\ r_{21} & r_{22} & r_{23} & 0 \\ r_{31} & r_{32} & r_{33} & 0 \\ 0 & 0 & 0 & 1 \end{bmatrix} \cdot \begin{bmatrix} x \\ y \\ z \\ 1 \end{bmatrix}. \tag{54}$$

Here, in the homogeneous coordinate expression, S_h is a similarity transformation matrix that consists of the translation T_h, the uniform scaling $\hat{S}_h$, and the rotation R_h. The basis vectors of S_h are the column vectors of $T_h \hat{S}_h R_h$. The transformed coordinate, $(x', y', z', 1)^{\mathsf{T}}$ can be represented with the linear combination of basis vectors of S_h since those are linearly independent.

$$\begin{bmatrix} \mathbf{T}_x \\ \mathbf{T}_y \\ \mathbf{T}_z \\ 1 \end{bmatrix} = \begin{bmatrix} \vec{q} & \vec{v} & \vec{w} & \vec{r} \end{bmatrix} \begin{bmatrix} 1 & 0 & 0 & u'_x \\ 0 & 1 & 0 & u'_y \\ 0 & 0 & 1 & u'_z \\ 0 & 0 & 0 & 1 \end{bmatrix} \begin{bmatrix} \vec{q} & \vec{v} & \vec{w} & \vec{r} \end{bmatrix}^{-1} \begin{bmatrix} x' \\ y' \\ z' \\ 1 \end{bmatrix}, \tag{55}$$

where $(\mathbf{T}_x, \mathbf{T}_y, \mathbf{T}_z)^\intercal$ is the transformation field in the WCS, $(u'_x, u'_y, u'_z)^\intercal$ the displacement field in the LCS, and $(x', y', z')^\intercal$ the initialized field by similarity transformation.

3.8.2 Incorporating Point Landmarks to 2D-3D Segmented Image-based Registration

A way to incorporate point landmarks into intensity-based registration was proposed in [54] in which the energy to be minimized between two binary segmented images $I : \Re^2 \to \Re$ and $J : \Re^3 \to \Re$ is defined as

$$E(C_1, C_2, \mathbf{T}) = S(I, J, C_1) + \sigma \left\| C_1 - \mathbf{T} \right\|^2 + \sigma\gamma \left\| C_2 - \mathbf{T} \right\|^2 + \sigma\lambda R(\mathbf{T}). \tag{56}$$

In this energy, $C_1 : \Re^2 \to \Re^3$ is a dense vector field demonstrating a set of correspondences between pixels of the segmented image I and J according to the intensity similarity measure, and $C_2 : \Re^2 \to \Re^3$ is a sparse vector field demonstrating a set of correspondences between a few point landmarks in I and their matching points in J, and $\mathbf{T} : \Re^2 \to \Re^3$ is the estimated transformation. σ is related to the level of noise in the image, λ is the smoothing strength, and γ is the relative strength of the geometric features compared to the intensity information. An efficient way minimizing Equation (56) is to minimize it alternatively w.r.t C_1 and $\mathbf{T}$.

(1) Find correspondences C_1 by minimizing $S(I, J, C_1) + \sigma \left\| C_1 - \mathbf{T} \right\|^2$.

Here, the *Gâteaux derivative* of $S(I, J, C_1) = \frac{1}{2} \left\| J_{C_1} - I \right\|_{L_2}$ with respect to C_1 is approximated to $f(x, y, C_1(x, y)) = (I(x, y) - J_{C_1}(x, y))\nabla_3 J_{C_1}(x, y)$ in which ∇_3 includes the third dimensional gradient of J around C_1.

(2) Find the transformation $\mathbf{T}$ by minimizing $\left\| C_1 - \mathbf{T} \right\|^2 + \gamma \left\| C_2 - \mathbf{T} \right\|^2 + \gamma R(\mathbf{T})$. The unique and explicit solution is a combination of convolution and splines [55] as the following:

$$\mathbf{T}(x) = K * C_1(x) + \sum_{i=1}^{p} \alpha_i K(x - p_i), \tag{57}$$

where the radial basis function K is a classical Gaussian kernel, independently on each component of the vector without Poisson effect in our case, and $\alpha_i \in R$ are coefficients found by solving a set of linear equations. To obtain α_i, the linear system can be rewritten as

$$\left(\frac{1}{\gamma}Id + W\right)\alpha = \beta, \tag{58}$$

$$W = (K(x_i - x_j)) = \begin{pmatrix} K(x_1 - x_1) & K(x_1 - x_2) & \cdots & K(x_1 - x_p) \\ K(x_2 - x_1) & \ddots & & \vdots \\ \vdots & & \ddots & \vdots \\ K(x_p - x_1) & \cdots & \cdots & K(x_p - x_p) \end{pmatrix}, \tag{59}$$

$$\beta = ((C_2(x_1) - K * C_1(x_1)), \ldots, (C_2(x_p) - K * C_1(x_p)))^{\mathtt{T}}. \tag{60}$$

3.8.3 Application of Spatially Varying (Inhomogeneous) Diffusion Equation

In Equation (56), the regularization part $\lambda R(\mathbf{T})$ is implemented with applying Gaussian smoothing to the dense displacement field and Gaussian radial basis function to the sparse displacement field. The weighting parameter λ that controls the smoothness is determined by the variance of Gaussian kernel. The regularization equally influences on all the image domain if using the homogeneous variance.

However, it is desirable that in vicinity of point landmarks, the smoothing effect of C_1 on $\mathbf{T}$ is reduced gradually. Thereby, the displacement field adjacent to point landmarks is more influenced by the sparse vector field C_2 defined by corresponding point landmarks. To implement this concept, we propose that the Gaussian smoothing to the dense displacement field $K * C_1(x)$ is replaced by the spatially varying (inhomogeneous) diffusion equation as follows:

$$\frac{\partial}{\partial t}C_1(x, y, t) = \nabla \cdot (D(x, y)\nabla C_1(x, y, t)), \tag{61}$$

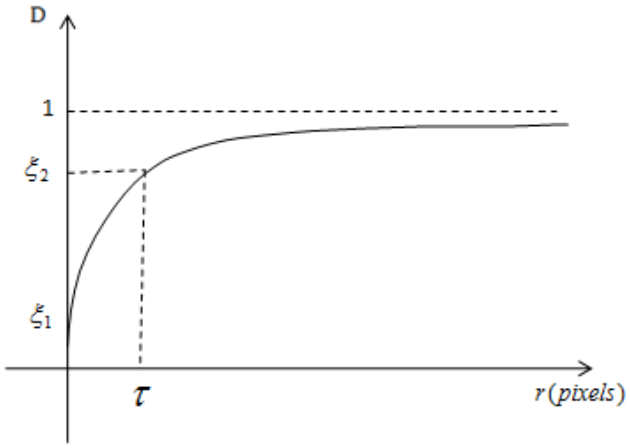

Figure 21: Varying diffusivity dependent on Euclidean distance r from the nearest point landmark.

where $D(x, y)$ is a diffusion conductance or diffusivity. If $D(x, y)$ is constant and independent of x and y, Equation (61) leads to a linear diffusion equation with a homogeneous diffusivity, so called a heat equation, which can be simplified to Gaussian convolution.

Our inhomogeneous diffusivity $D(r(x, y))$ is dependent on x and y as follows:

$$D(r(x,y)) = -\frac{\tau(1-\xi_2)(1-\xi_1)}{r(\xi_2-\xi_1)+\tau(1-\xi_2)} + 1, \; D \in \Re^{M\times N}, \tag{62}$$

where $r(x, y)$ denotes $min_i \sqrt[2]{(x-x_i)^2+(y-y_i)^2}$, and (x_i, y_i) is the position of i-th point landmark in the histology image. The diffusivity decreases to ξ_1 as the distance to the nearest point landmark decreases, and the maximum diffusivity is confined to 1. The input τ to the function is assigned to the output ξ_2. Empirically we determined $\xi_1 = 0$, $\xi_2 = 0.5$, and $\tau = 20$ pixels. The numerical scheme to solve the inhomogeneous diffusion equation was introduced by Frangakis [56].

3.8.4 Results

This section will exhibit qualitative and quantitative comparisons of our proposed method using the inhomogeneous diffusivity with the method using the homogeneous

diffusivity on real subjects. The qualitative comparison includes the boundary matching and the deformed transformation grid with point landmarks (Figure 22, 24, and 23). The quantitative comparison includes the sum of squared differences (SSD) and the closeness between transformed coordinates at point landmarks in the histology image after the registration is completed and corresponding landmarks of the MR image volume (Table 7). In Figure 22, the registration with the inhomogeneous diffusivity produced generally more acceptable boundary matching results than the registration with the homogeneous diffusivity. In Figure 24, we can see that the transformation was adjusted in vicinity of point landmarks, which resulted in the improved matching. And the numeric results in Table 7 verify a justification for a use of the inhomogeneous diffusivity regularization.

Table 7: Numeric results of a sum of squared difference (SSD) and an average of point landmark differences for inhomogeneous vs. homogeneous diffusivity.

Pat	Measures	Inhomogeneous diffusivity	Homogeneous diffusivity
Pat ♯1	SSD	0.01421	0.02183
	Avg. of point distances	4.1638	6.6323
Pat ♯2	SSD	0.02801	0.06109
	Avg. of point distances	2.5895	5.1400
Pat ♯3	SSD	0.02316	0.05228
	Avg. of point distances	6.9145	12.1460
Pat ♯4	SSD	0.01618	0.02811
	Avg. of point distances	10.5672	13.3777

Also, for a reliable verification, some of those point landmarks are utilized just for verifying the proposed method separately from being utilized for registering images.

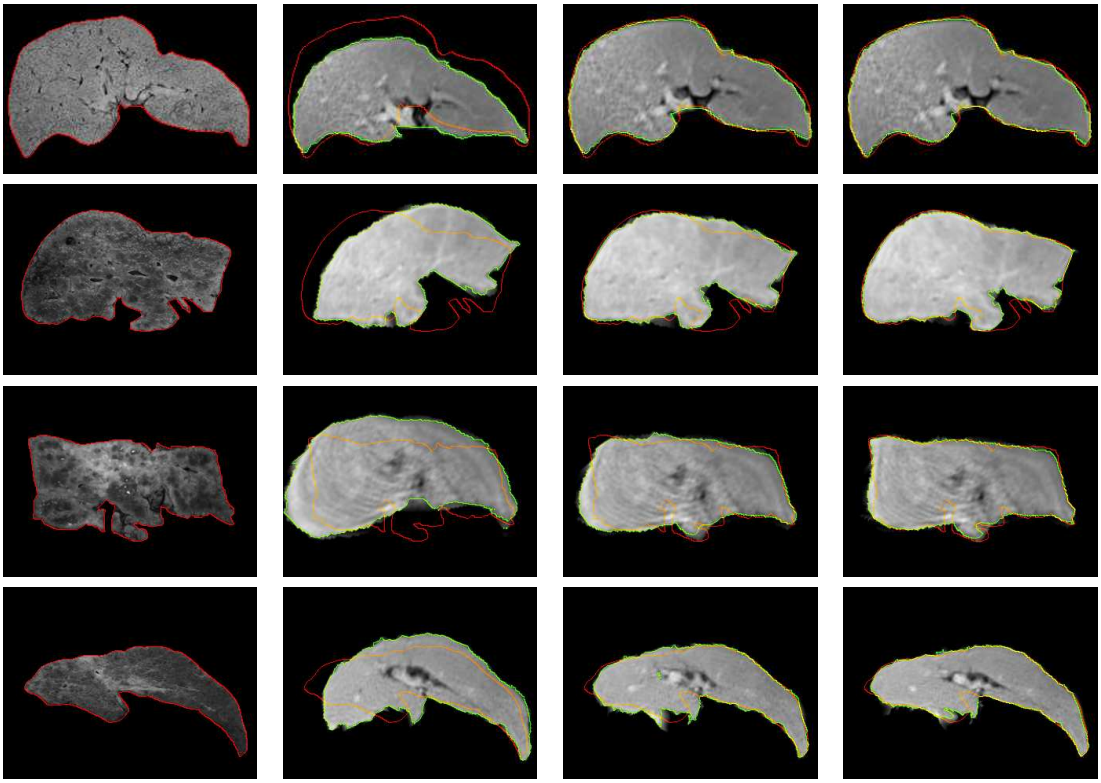

Figure 22: Image results for four real subjects: (a) column indicates the histology image, (b) column indicates the initialized MR image by the similarity transformation, (c) column indicates the resulting image after the non-rigid registration with the homogeneous diffusivity, and (d) column indicates the resulting image after the non-rigid registration with the inhomogeneous diffusivity.

3.8.5 Conclusion

we presented a method for registration of 2D gross pathology image and 3D MRI of the liver. Registration of liver histology and MR images is an important first step required for optimized analysis of the correlation between histologic tissue evaluation on specimens and corresponding ROIs of MR image. Given manually selected multiple point landmarks, the method is initialized with similarity transformation. The following non-rigid registration combines liver segmentation and point landmarks using a spatially-varying diffusion. Tests on real cases show accurate alignment of histology and MRI.

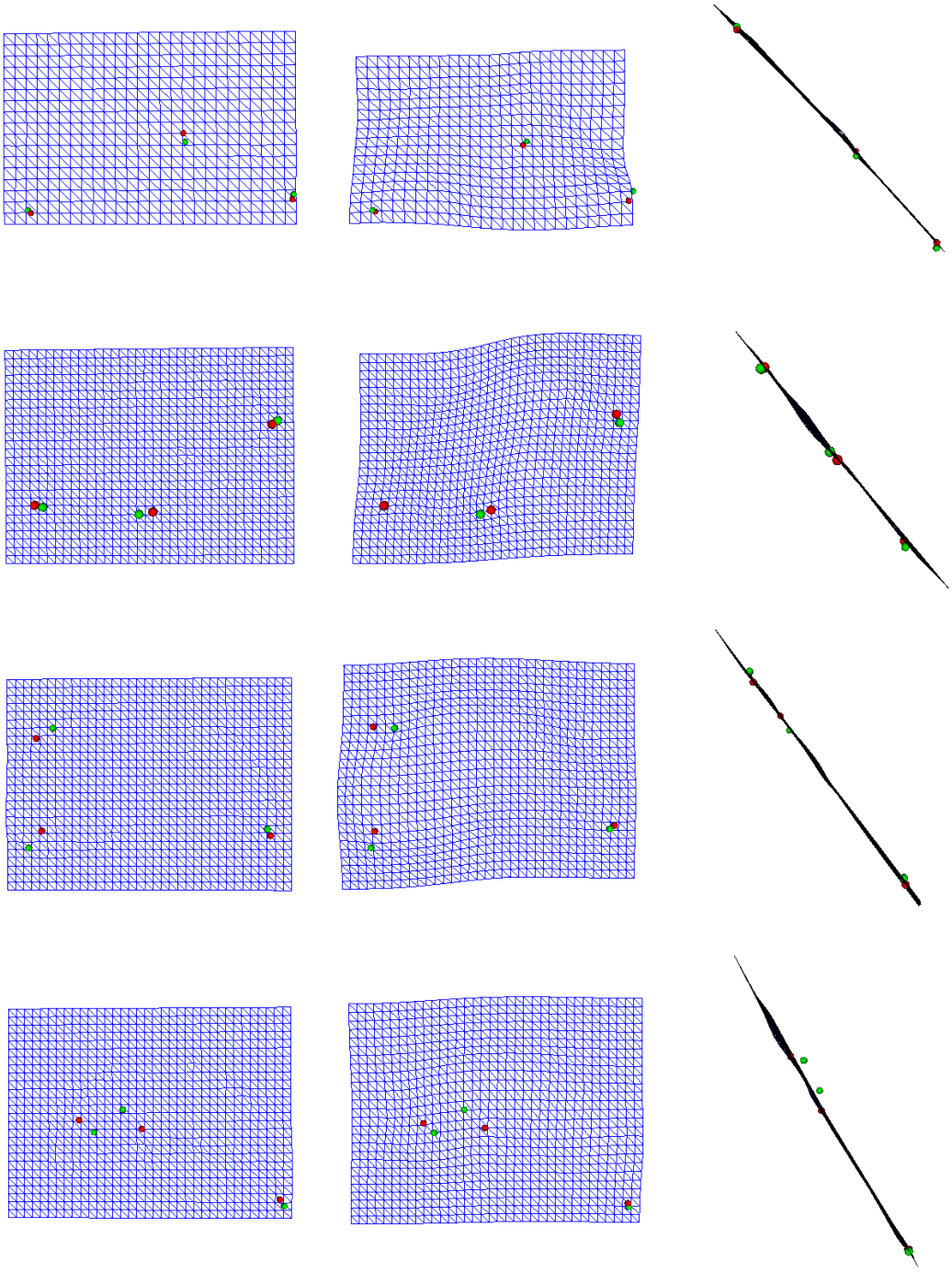

(a) (b) (c)

Figure 23: Results of grid and points using the homogeneous diffusivity for four patients: (a) a front view after similarity transformation, (b) a front view after non-rigid registration, and (c) a side view after non-rigid registration. Note that in the side view (c) of the last patient, some of control points are not matching in out-of-plane.

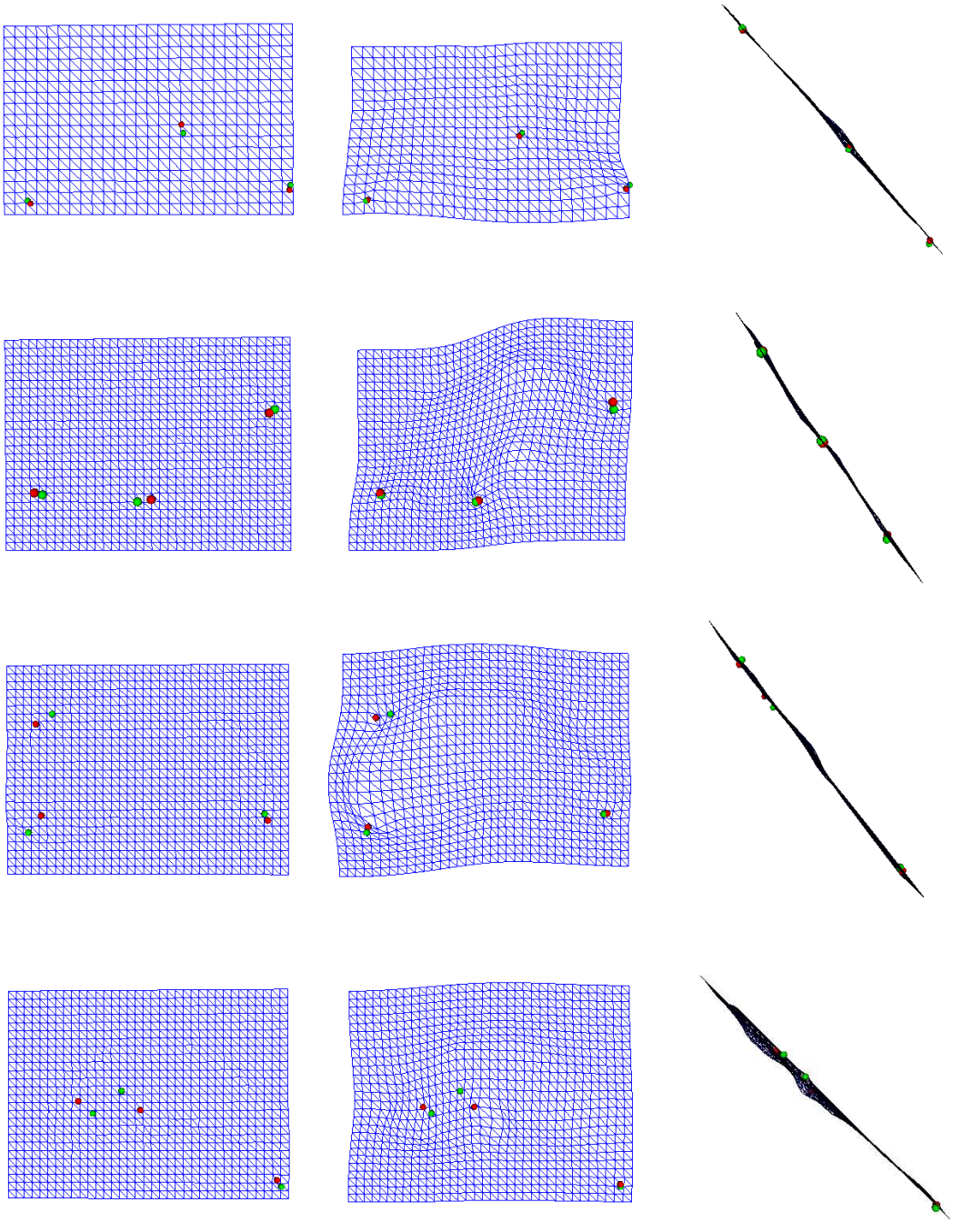

(a) (b) (c)

Figure 24: Results of transformed grids and point landmarks using the inhomogeneous diffusivity for four patients: (a) a front view after similarity transformation, (b) a front view after non-rigid registration, and (c) a side view after non-rigid registration. The green and red points indicate the point landmarks of MR images and histology images, respectively.

CHAPTER IV

IMAGE SEGMENTATION

4.1 Introduction and Related Works

For a non-invasive, image-based analysis using the assessment of texture features or contrast uptake time curves, magnetic resonance imaging (MRI) is now being used for supplementing biopsies, which are suboptimal, invasive procedures. MRI is the most diagnostically comprehensive modality for both the evaluation of tumors and the analysis of changes related to diffuse liver diseases. Liver segmentation in contrast-enhanced MRI is an essential pre-processing task for defining and localizing the volume of interest (VOI). Visual delineation by humans is both time consuming and error prone, so the automation of the process has become a necessity.

Because of the geometric proximity of the liver to its surroundings and inhomogeneous intensity distribution, liver segmentation is extremely complicated. The liver consists of left and right lobes constructed around a central vein perfusing into the left and right hepatic veins. It also contains the hepatic artery and the portal vein engaged in main blood supplies. Exteriorly abdominal organs responsible for urinary and digestive functions such as the kidney, the pancreas, and the spleen are located close to the liver. Therefore, because of the weak organ boundaries, poor gradient information, and indistinct intensity, MRI cannot easily distinguish the liver from the other organs. In addition, an inhomogeneity of intensity arises from imperfections of the image acquisition process, including inhomogeneities of the static field and radio frequency transmission and reception [57], the position of the imaged object, and the partial contrast uptake.

Although representative algorithms in computed tomography (CT) scans [58] can

be used for segmentation, we need to analyze the properties of each one and ascertain its availability for contrast-enhanced liver MRI. For example, shape-constrained segmentation using a statistical shape model [59, 58, 60] or atlas-matching using B-splines [61] require extensive training sets and landmarks resulting from the high variation of the shape of the liver. The region growing method [62] can lead to leakage into adjacent organs because of a lack of topological constrains, and the use of fixed confidence intervals for the intensity distribution cannot guarantee segmentation of the entire liver region with varying intensity. Another algorithm, the graph-cut method [63], is a highly interactive refinement process that adds or removes individual segmented regions. However, these are only a few of the methodologies that relate to the MRI. One algorithm, shown to be feasible and efficient, is to perform region-growing on a partitioned probabilistic model [64] which divides the liver into eight parts based on its various local intensity statistics. Improved active contour methods for perfusion analysis [65] have employed multiple initialization, multiple step fast marching method (FMM), and level set methods (LSM) to overcome leakage and over-segmentation problems; and then the convex hull (CH) algorithm combined partial segmentations.

The active contour, which uses level set representation, is state-of-the-art technology in segmentation. It is advantageous because its resulting contours facilitate labeling without an additional process of connecting boundaries and because it allows the merging and splitting of multiple contours. Unfortunately, the classic active contour methods such as edge-based geodesic active contour or region-based active contour methods, which use either gradient or regional statistics, are insufficient for ill-conditioned images. A unified approach to mitigating this problem is geodesic active regions [66], which extract the boundary attraction from the geodesic active contour framework and compute the regional attraction by maximizing a posteriori frame partition probability. However, a limitation of this method is that a priori

information about the optimal number of partitions is unknown, and the liver in contrast-enhanced MRI may not have a Gaussian mixture profile that discriminates it from surrounding organs. Consequently, segmentation results might contain non-liver regions imaged in the intensity range overlapping with the liver. Another coupled active contour method using a prior shape and intensity profile [67] is also insufficient because it has to account for the wide variation in the liver shape.

Therefore, we will present a simple new coupling active contour method with level set representation that requires boundary and regional mean intensity information but not a prior probabilistic information or a shape model. This method, the edge function-scaled region-based active contour (ESRAC), will be discussed with 3-D experimental studies using contrast-enhanced liver MRI.

4.2 Edge Function-Scaled Region-based Active Contour (ESRAC)

Unlike geodesic active contour (GAC) model, Chan-Vese region-based active contour (CVRAC) model can detect the target whose boundaries are not necessarily defined by a gradient or very smooth boundaries. However, the CVRAC by itself cannot work well in cases in which the regional statistics cannot bisect the image into the target and the non-targets, including background. In contrast-enhanced abdominal MRI, for example, the liver may not be only object intensity-enhanced by the uptake of contrast agent, but the kidney also can be enhanced because of the partial uptake of the material. Or, the malfunctioning of liver cells may impede transport of contrast agent, leading to little contrast-enhancement. To overcome this limitation, we can use other information such as the curvature or texture statistics, which are not robust to general cases. Unlike the classical active contour models, GAC and CVRAC, which take either the gradient or regional statistics into account to detect the boundary of the target, the novel active contour model, ESRAC, incorporates both in a simple

way. We first define the edge function-scaled fitting term,

$$F_1(c_1, C) + F_2(c_2, C) = \lambda_1 \int_{C_{in}} g(I(x,y))|I(x,y) - c_1|^2 dxdy + \lambda_2 \int_{C_{out}} g(I(x,y))|I(x,y) - c_2|^2 dxdy, \tag{63}$$

where $g(I(x,y))$ is the edge detector characterized as (5). By adding the geodesic constraints, this fitting term is regularized, and thereby the energy functional for the ESRAC model becomes

$$E_{ESRAC}(c_1, c_2, C) = F_1(c_1, C) + F_2(c_2, C) + \mu \cdot \text{Length}_R(C) + \nu \cdot \text{Area}_R(inside(C)), \tag{64}$$

where $\text{Length}_R(C)$ and $\text{Area}_R(C)$ are the length of contour and the area inside the contour in the Riemannian space, respectively, as defined in (6) in the GAC model. The associated Euler-Lagrange equation for level set ϕ deduces

$$\frac{\partial \phi}{\partial t} = |\nabla \phi| \Bigg[\underbrace{-\lambda_1 g(I)(I - c_1)^2 + \lambda_2 g(I)(I - c_2)^2}_{\text{region-based term}} + \underbrace{\mu \left(g(I)(\kappa + \nu) + \nabla g(I) \cdot \frac{\nabla \phi}{|\nabla \phi|} \right)}_{\text{edge-based term}} \Bigg]. \tag{65}$$

By coupling the GAC model and the CVAC model, the ESRAC model does not have the limitations of these models. Figure 25 helps explain the interaction. On the top images, in which the intensities change very smoothly, only the edge-based term does not prevent the evolution around the estimated boundary because the strong gradient, which turns the edge function to zero, does not exist. However, the edge-based term causes the region-based term to adversely react to the gradient descent flow, and the total gradient descent flow becomes zero around the boundary

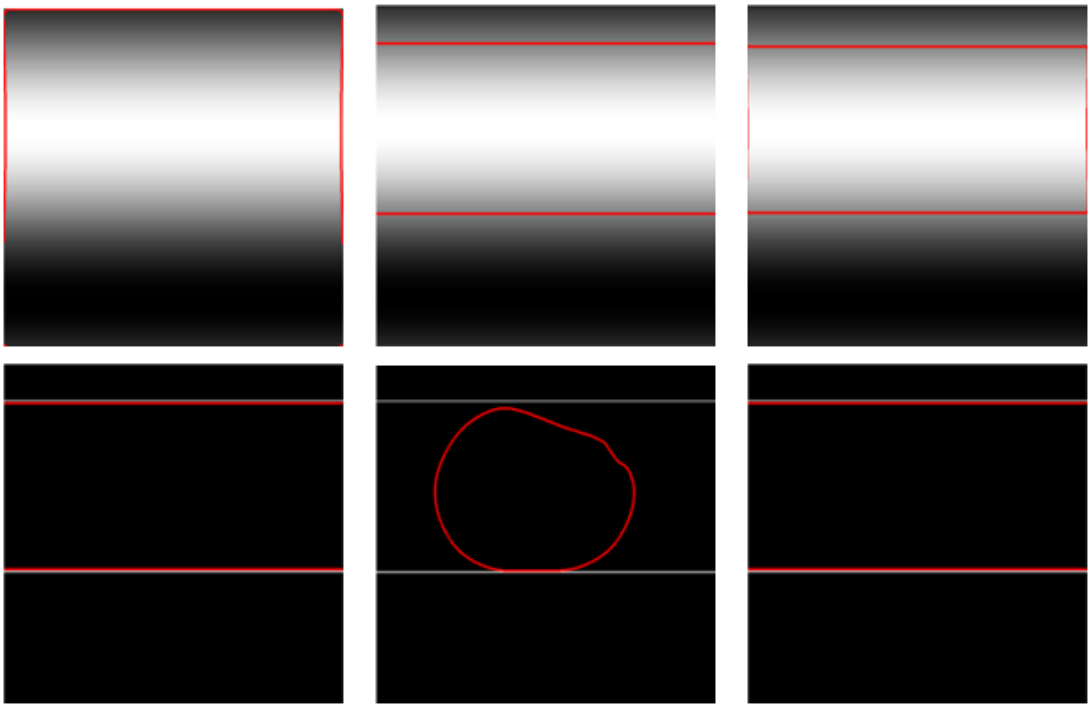

Figure 25: Image illustrating a hybridization of the ESRAC model. The images on the top have no strong edge, but they are able to differentiate the target in the upper center by an intensity criterion. The images on the bottom have a strong edge, but the target from the background exhibits no intensity difference: the GAC model (left); the CVRAC model (center); the ESRAC model (right). The enclosed red curve indicates the final evolution of the contour.

as the simulation in the top right image. We can also assume another boundary case, as illustrated in the bottom images, in which the mean intensity of the target region in the upper center is not distinct from the outside of the boundary. Little gradient descent flow is led by a region-based term, so the contour fails to diffuse in the simulation on the bottom center. Nevertheless, the edge-based force supports the gradient descent flow by the region-based force, so the contour expands up to the boundary. The ESRAC model that uses the coupled forces arising from the edge-based term and the region-based term succeeds in both boundary cases.

Edge functions become monotonically decreasing and asymptotically positive zero as the gradient goes to infinity as follows: $g(I(x,y)) = (1+\alpha|\nabla G_\sigma(x,y) * I(x,y)|^2)^{-1}$ and $g(I(x,y)) = (e^{\alpha|\nabla G_\sigma(x,y)*I(x,y)|^2})^{-1}$, which respectively correspond to left two plots in Figure 26. Because of its open bound in the interval of $[0,\ \infty)$, numerically setting it up to stop propagating the curve at a desired gradient threshold using the functions becomes an issue. Although the L^2 norm of the gradient has been generally used as a function variable, it is anisotropic despite the intensity change being equivalent in any direction. For example, if the intensity changes on the horizontal, vertical, and diagonal boundaries in two-dimensional space from 0 to 255, then the numerical gradients using the finite difference method are $(0, \frac{255}{2})^T$, $(\frac{255}{2}, 0)^T$, and $(\frac{255}{2}, \frac{255}{2})^T$, whose L^2 norms of the gradients are $\frac{255}{2}$, $\frac{255}{2}$, and $\sqrt{2}\frac{255}{2}$, respectively. Anisotropy of the L^2 norm can cause segmentation errors. A good alternative is to use the L^∞ norm, which is the absolute maximum of the vector elements. Thus, a new compactly-supported edge function with L^∞ norm is given by

$$g(I(x,y)) = (1 - \alpha|\nabla G_\sigma * I(x,y)|_\infty^2)_+^2, \tag{66}$$

where $f = (1-r)_+^2$ indicates that the function f is zero if r is greater than 1. This function is continuous and differentiable at $r = 1$, so it belongs to class C^1. The

threshold α is an inverse of the lowest squared L^∞ norm that make Equation (66) zero, $\alpha = \frac{1}{|\nabla G_T|^2_\infty}$.

4.3 Application to Contrast-Enhanced Liver MRI

In total, contrast-enhanced liver MRI sequences consisting of pre-contrast (0 second after injection), arterial (20 second), portal-venous (1 minute), equilibrium (3-4 min), and delayed phases (20 min) are acquired in the clinical routine. The post-contrast scans are corrected for motion to match to the pre-contrast scan in intensity-based rigid and non-rigid manner [68]. Approximately 50% of the contrast agent injected is renally excreted, whereas the other 50% is transported to the liver cells and then excreted via the biliary system [29]. The dual enhancement and geometric proximity of the kidney and the liver make segmentation of the liver so demanding.

4.3.1 Liver Partitioning

The signal quality of contrast-enhanced liver MRI can be affected by inhomogeneities of the static magnetic field and localized contrast uptake. One way to mitigate this problem is to separate the liver into multiple partitions and compute the regional statistics for each partition in the ESRAC model. According to Couinaud liver segments, the liver can be divided into eight functionally independent partitions in which the plane defined by the portal vein divides the liver superiorly and inferiorly, and the right, middle, and left hepatic veins divide into four segments in the periphery. Due to the difficulty of categorizing according to the portal and hepatic veins in MR imaging, we linearly divide the image by a set of fixed orientations, as illustrated in Figure 28 (c) and (d), from the center of the aorta detected in every slice where the circular Hough transform algorithm [69] can detect the circular shape of the aorta with a specific diameter in the arterial phase, shown in Figure 28 (b). The plane on which the superior and inferior regions are divided is approximated as the central plane of the aorta. To apply this partitions into the ESRAC model, we construct a

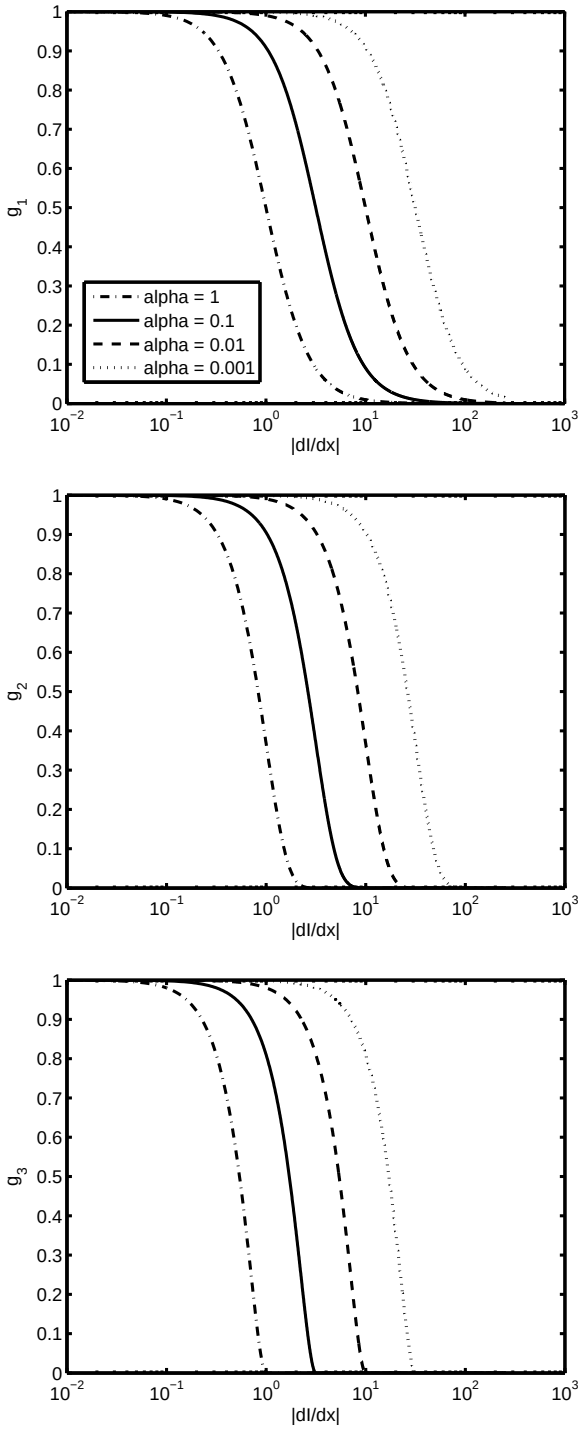

Figure 26: Edge functions on the left: $g_1(I(x,y)) = (1 + \alpha|\nabla G_\sigma(x,y) * I(x,y)|^2)^{-1}$**; on the middle:** $g_2(I(x,y)) = (e^{\alpha|\nabla G_\sigma(x,y) * I(x,y)|^2})^{-1}$**; and on the right:** $g_3(I(x,y)) = (1 - \alpha|\nabla G_\sigma * I(x,y)|^2)_+^2$**. Note that the X axis is log-scaled.**

label array $L(x, y)$, consisting of integer elements 1 to M, to represent the M exclusive partitions. And a mask $T(L(x, y), k)$ corresponding to the k-th partition is given by

$$T(L(x,y),k) = \begin{cases} 1, & \text{if } L(x,y) = k; \\ 0, & \text{otherwise.} \end{cases} \tag{67}$$

$$\begin{aligned} & E_{p-ESRAC}(c_1^k, c_2^k, C) \\ = & \sum_{k=1}^{M} \Bigg[\lambda_1 \int_{C_{in}} T(L(x,y),k) g(I(x,y)) |I(x,y) - c_1^k|^2 dxdy \\ & + \lambda_2 \int_{C_{out}} T(L(x,y),k) g(I(x,y)) |I(x,y) - c_2^k|^2 dxdy \Bigg] \\ & + \mu \cdot \text{Length}_R(C) + \nu \cdot \text{Area}_R(inside(C)), \end{aligned} \tag{68}$$

where c_1^k and c_2^k denote average intensities inside and outside the contour in the k-th partition, respectively, which is shown in Figure 27. The associated level set is given by

$$\begin{aligned} \frac{\partial \phi}{\partial t} = |\nabla \phi| \Bigg\{ & \sum_{k=1}^{M} T(L,k) \Big[-\lambda_1 g(I)(I - c_1^k)^2 + \lambda_2 g(I)(I - c_2^k)^2 \Big] \\ & + \mu \Bigg(g(I)(\kappa + \hat{\nu}) + \nabla g(I) \cdot \frac{\nabla \phi}{|\nabla \phi|} \Bigg) \Bigg\}. \end{aligned} \tag{69}$$

4.3.2 Seed Initialization

To initialize a seed region, thresholding of $[200, \infty]$ is applied to the delayed phase image. Then to remove isolated segments and unnecessary connections from surrounding objects, including the kidney, the stomach, or the pancreas, we perform a finite iteration of 3-D erosion using the sphere structure with a five-voxel radius to the obtained binary image. Then, from the eroded binary mask, the largest connected

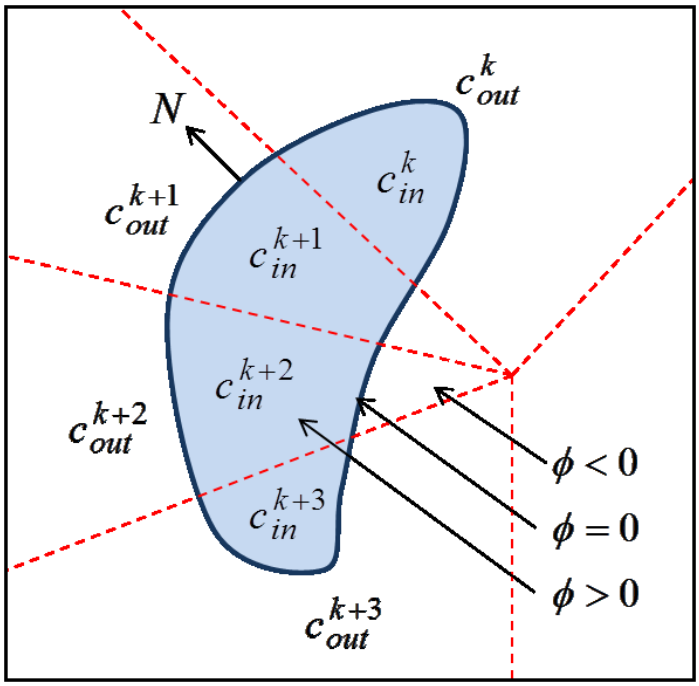

Figure 27: The level set representation of p-ESRAC: the zero level set ϕ_0 is more evolved by the local statistics in multiple partitions.

3-D region is chosen as the initial seed.

4.3.3 Segmentation using ESRAC

Upon visual inspection, the kidney appears to be most enhanced in the arterial phase and then decreases with time while the liver keeps enhanced up to the delayed phase for normal subjects. However, in the case of abnormal subjects, the uptake of a contrast agent to the liver cells does not function, and the signal decreases after peaking in the early phase; therefore, the contrast between the liver and the kidney is not strong in the delayed phase. To deal with this problem, our knowledge of the boundaries between the liver and surrounding organs: the boundaries of the liver against the kidney and the abdominal wall are clear in the arterial and delayed phases, respectively. To incorporate this knowledge into the ESRAC model, we compute element-wise maxima of L^{∞} norms of the gradient in the Gaussian-smoothed arterial and delayed phases for each voxel, as shown in Figure 29, and the regional statistics

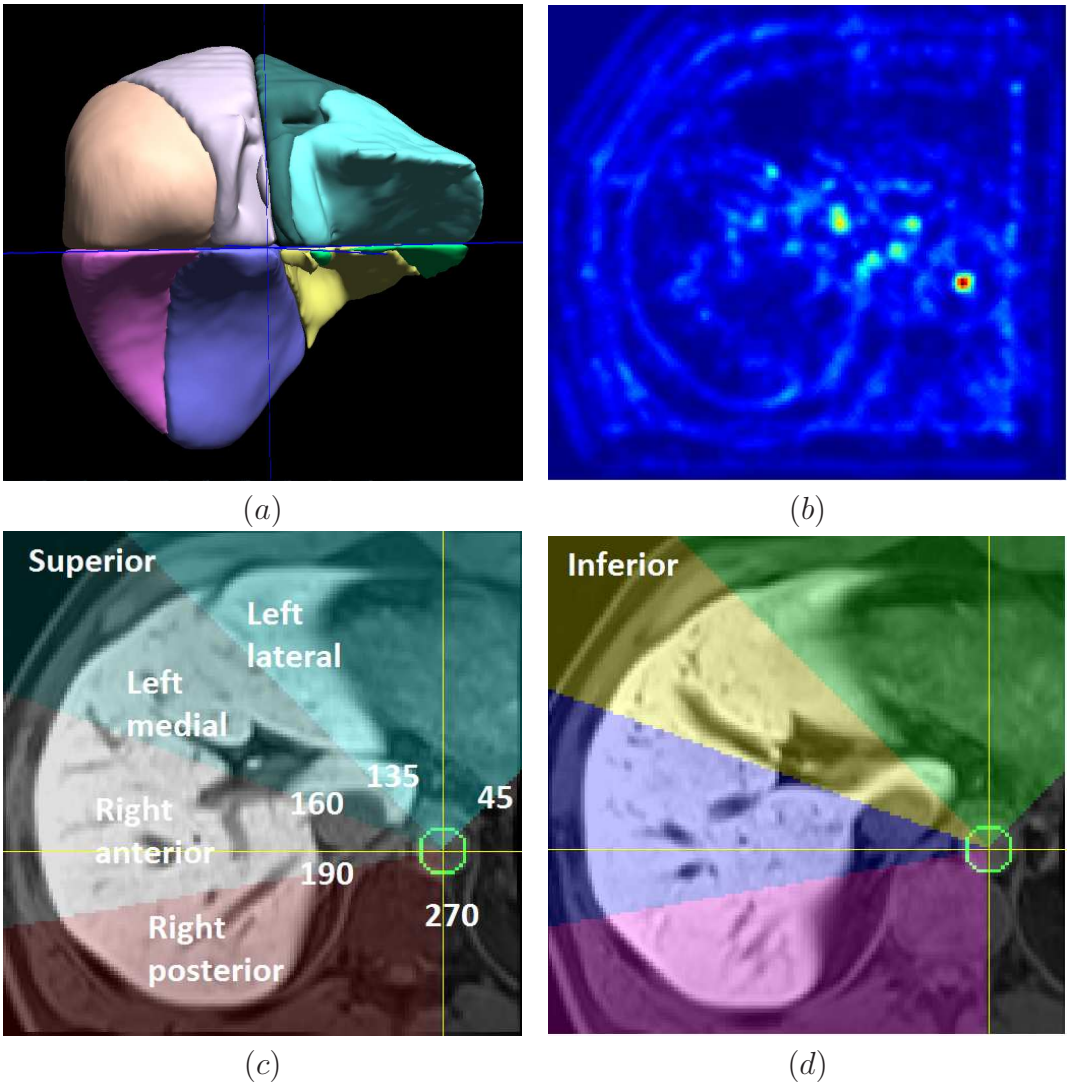

Figure 28: Partition of the liver: (a) eight functionally independent partitions of the liver, (b) accumulation map of the circular Hough transform for detecting the aorta in the arterial phase, (c) and (d) subdivision of the liver by a set of fixed angles from the center of the detected aorta in the superior and inferior parts, respectively.

in the partitioned liver only in the delayed phase. Prior to segmentation, resampling to isotropic voxel size is necessary for the smooth evolution of the contour, and then downsampling is recommended to reduce computation time. This active contour is iteration-based, so it is repeated until the mean of the absolute difference between the current and previous level sets in the entire image domain is smaller than 5×10^{-4}. The maximum iteration was set as 10^3 times. The sigma of the Gaussian smoothing was 0.5, and the threshold α in Equation (66) was 10^{-2}.

4.3.4 Iterative Morphological Operation

After completing the segmentation, iterative morphological operations (IMO) is performed to acquire the enclosed and smooth segmented volume. First, the filling operation removes the elongated holes generated by the high gradient around the vessels, and then closing operation smoothes out the uneven surface of the segmented volume. Then for each iteration, the IMOs are performed in axial, coronal, and saggittal planes and repeat until the volume of non-zero voxel undergoes no change.

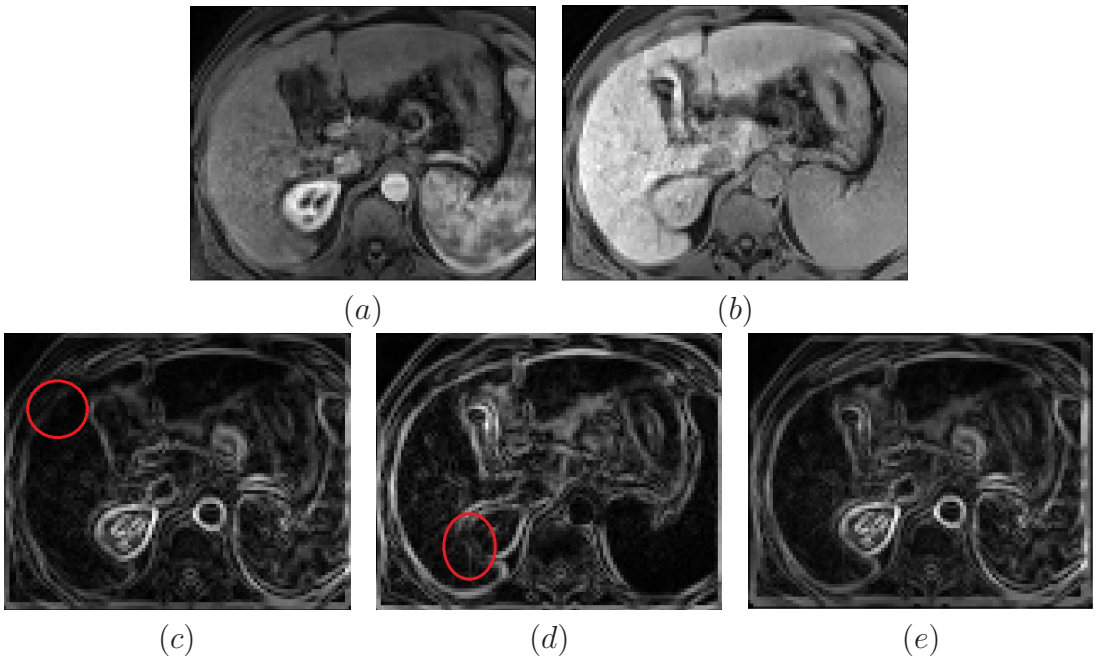

Figure 29: Computation of the gradient: (a) motion-corrected image at the arterial phase; (b) motion-corrected image at the delayed phase; (c, d) the L^∞ norm of the gradient at the arterial and delayed phases, respectively; (e) the element-wise maxima of L^∞ norms at two phases. The red circles indicate regions where the gradient is not large enough at each phase. The combination of (c) and (d) yielded a better gradient image in (e).

4.4 Experimental Results

For all of the subjects, a reference volume was delineated manually to use it as gold standard for evaluating the performance of the segmentation. It was initiated by thresholding, and then modified by removing the extra volume or filling in gaps manually in the BrainSuite graphic tool [70]. Using the same initial seeds that had been generated automatically, we quantified the accuracy of the segmentation using the following metrics: the dice similarity coefficient (DSC), the true-positive rate (TPR), the false-positive rate (FPR), the relative volume difference (RVD), the volumetric overlap error (VOE), all defined below, and the average symmetric surface distance (ASSD), which computes the average distances of the closest voxel along the reference and segmented borders. The R^2 coefficient, which is the square of the correlation

coefficient of the volumes between the reference and segmented regions, was also evaluated. The larger absolute values of DSC, TPR, and R^2 and the smaller absolute values of FPR, RVD, VOE, and ASSD correspond to higher segmentation accuracy.

Metric	Definition
DSC	$\frac{V_S \bigcap V_R}{.5*(V_S+V_R)}$
TPR	$\frac{V_S \bigcap V_R}{V_R}$
FPR	$\frac{V_S \bigcap V_R^c}{V_R}$
RVD	$\frac{V_S - V_R}{V_R}$
VOE	$1 - \frac{V_S \bigcap V_R}{V_S \bigcup V_R}$

where V_S and V_R denote the segmented and the reference volumes, respectively.

4.4.1 Validation of Partitioned ESRAC (p-ESRAC)

To validate the partition of the liver, the ESRAC is incorporated with the computed regional statistics of the eight independent partitions, the so-called "partitioned ESRAC" (p-ESRAC), and compared it with the ESRAC. In Figure 30, signal inhomogeneity appeared over the liver, particularly where the left lobe region (a,b) or the hypodense leison region (c) was lower in intensity than other regions. Therefore, for ESRAC, these regions were not included in the contour since the higher mean intensity of the remaining region inside the contour impeded the evolution of the contour in the low-signal region. By contrast, the p-ESRAC model, affected just by the local mean computation of the partition, including the vulnerable regions, performed better in the contour evolution. As for the quantifications covering the 14 subjects, Table 8 showed that the p-ESRAC slightly outperformed the ESRAC in most measures except for the FPR; for the p-ESRAC, the average DSC (with the standard deviation) was 93.9($\pm$1.6)%, TPR 92.5($\pm$3.1)%, FPR is 4.5($\pm$3.2)%, RVD is $-$3.0($\pm$5.5)%, VOE is 11.5($\pm$2.8)%, ASSD is 1.8($\pm$0.6)%, and R^2 0.9696. For the ESRAC, the average DSC (with the standard deviation) was 93.8($\pm$1.7)%,

TPR 92.1(±3.6)%, FPR 4.2(±2.9)%, RVD −3.7(±5.8)%, VOE is 11.7(±2.9)%, ASSD 1.9(±0.6)%, and R^2 0.9673. The lower FPR indicates less over-segmentation, suggesting that the p-ESRAC tends to segment slightly larger than the ESRAC, but with a negligible area outside the reference.

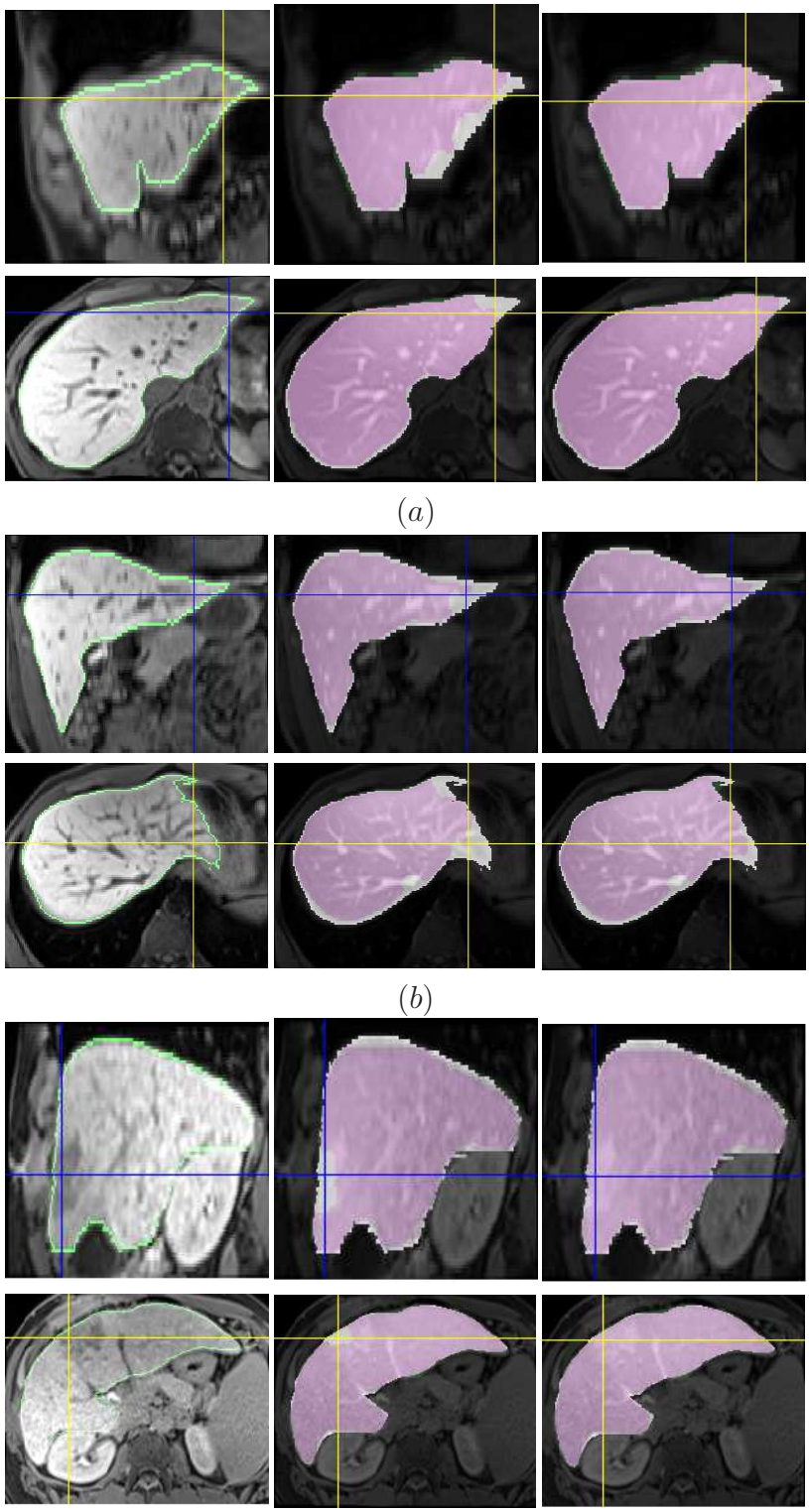

Figure 30: Visual comparison between the p-ESRAC and the ESRAC for three subjects. The left column shows the original image in the delayed phase with the reference contour (green). The middle and the right columns show the segmented region (pink) resulting from the ESRAC and the p-ESRAC with the reference region (white), respectively.

4.4.2 Comparison of the p-ESRAC with Other Techniques

To confirm that existing methods are not as adaptive as our method for contrast-enhanced liver MRI, we compared ESRAC and p-ESRAC with other automated segmentation techniques, including region growing (RG), geodesic active contour (GAC), and Chan-Vese region-based active contour (CVRAC) methods. In the RG algorithm [71], similar neighboring pixels are merged, starting from manually or automatically selected seeds from the region of interest. The absolute threshold level was 5% of the difference between the maximum and the minimum of the image. The initial value of the region mean was updated at every iteration. (Other techniques are already mentioned in the background section.) Figure 31 shows that the RG was prone to leakage to neighboring objects, including the kidney, which were separated from the liver by a small intensity. By taking advantage of the gradient response between the liver and the kidney, which was relatively evident, the GAC managed to partition the kidney from the entire liver; leakage to background, however, was still inevitable. Even though the CVRAC showed better results than previous methods, substantially curbing over-segmentation, the leakage-to-kidney problem still occurred and needs to be addressed. Our p-ESRAC method worked exceptionally well in most cases, significantly improving the over-segmentation problem.

In most measures, the ESRAC yielded superior quantitative results over the other methodologies. Based on measurements of the FPR, over-segmentation decreased. However, the ESRAC produced lower TPR than the CVRAC because the gradient of the voxels close to the boundaries of a target was high, so the constraint of gradient scaling. As a result, the FPR that accounted for over-segmentation of the ESRAC decreased more than that of the CVRAC. However, the TPR increased a little at a risk of being under-segmented around the border. Figure 4.4.3 shows that the volume of the reference and the segment using the p-ESRAC are most linearly correlated, R^2 =0.9696, and the slope of the regression model is closest to one, 0.9555.

In Table 8, note that the p-CVRAC and the p-RG (for reference, the p-GAC does not exist) increased the TPR. In other words, under-segmentation was corrected by the p-CVRAC and the p-RG more significantly than it was by their original methods from 97.9 to 99.2 and from 74.8 to 93.1, respectively. However, the FPR of the p-CVRAC and the p-RG underwent a greater increase than their original methods from 31.3 to 52.5 and from 13.5 to 59.1, respectively. This finding indicates an even greater risk of over-segmentation. Therefore, after the incorporation of the partition scheme into the computed regional statistics in the CVRAC and the RG, their overall performance was worse than that of ESRAC.

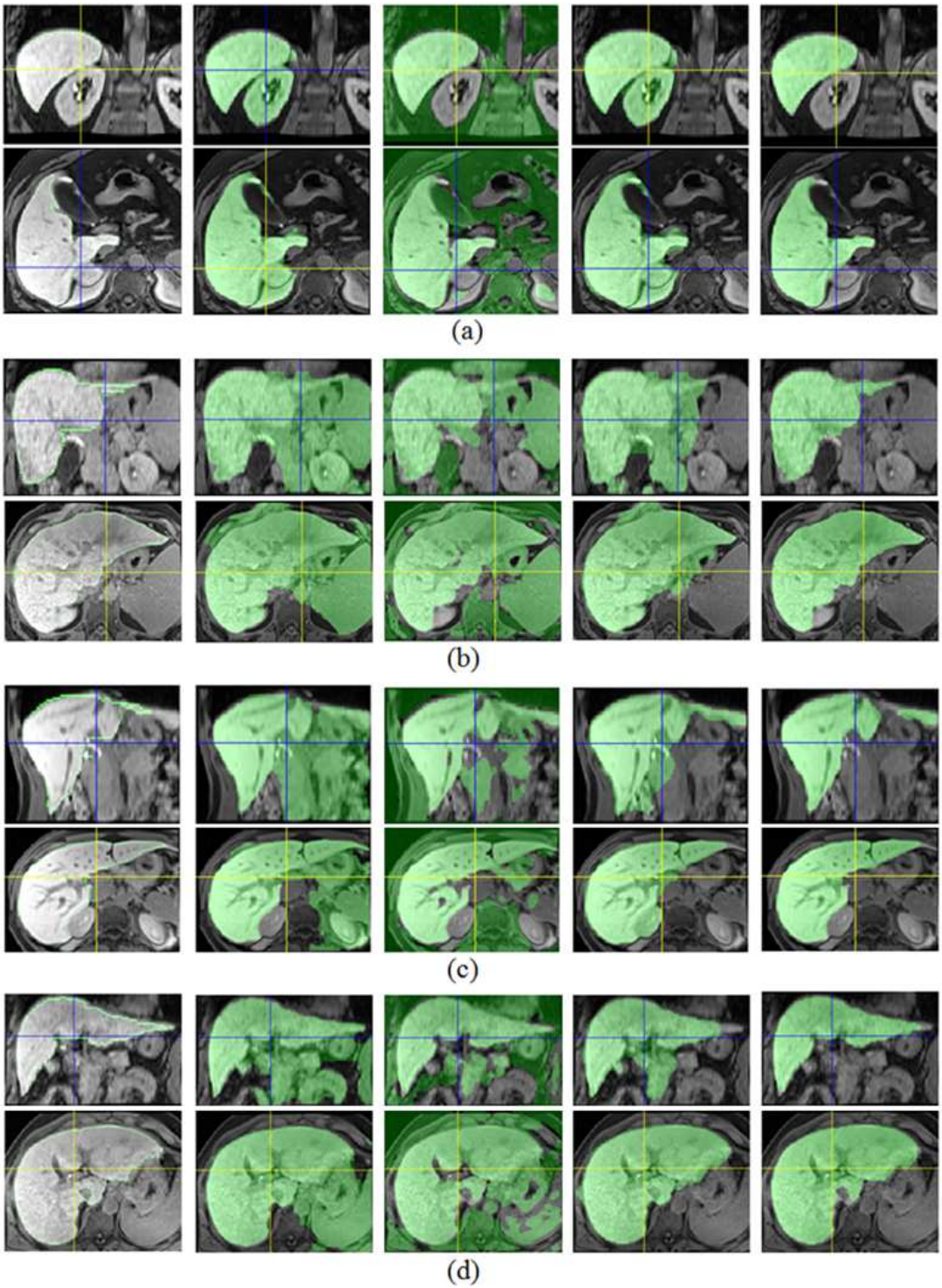

Figure 31: Visual comparisons among four segmentation algorithms. The original image and reference contour (green) at the delayed phase in the first column, the segmented regions resulting from varying segmentation methods. The results are shown in the coronal (top) and axial (bottom) planes, and the green mask indicates the computed segmented region.

Table 8: The average and standard deviation of the quantitative measures–the dice similarity coefficient (DSC), the true-positive rate (TPR), the false-positive rate (FPR), the relative volumetric difference (RVD), the volumetric overlap error (VOE), the average symmetric surface distance (ASSD)–for 14 real subjects were evaluated using the four automated segmentation methodologies.

		DSC (%)	TPR (%)	FPR (%)	RVD (%)	VOE (%)	ASSD (mm)	R^2
p-ESRAC	avg	93.9	92.5	4.5	-3.0	11.5	1.8	0.9696
	std	1.6	3.1	3.2	5.5	2.8	0.6	
p-CVRAC	avg	80.7	99.2	52.5	51.7	31.1	4.8	0.5266
	std	11.3	1.1	44.8	45.1	14.7	3.2	
p-RG	avg	77.5	93.1	59.1	52.2	34.0	3.2	0.6282
	std	16.5	5.4	60.9	63.0	22.1	2.5	
ESRAC	avg	93.8	92.1	4.2	-3.7	11.7	1.9	0.9673
	std	1.7	3.6	2.9	5.8	2.9	0.6	
CVRAC	avg	86.8	97.9	31.3	29.1	22.2	3.5	0.5578
	std	10.0	3.9	35.1	35.8	13.9	2.8	
RG	avg	79.4	74.8	13.5	-11.7	33.4	5.6	0.6070
	std	8.4	13.9	20.3	29.5	11.6	2.8	
GAC	avg	43.8	90.4	327.0	317.4	69.0	2.4	0.4284
	std	22.9	5.3	221.2	223.9	22.0	0.9	

4.4.3 Computation Time

In this study, we used an Intel Xeon CPU X5355 @ 2.66GHz with 16 GB of main memory in Linux OS. The overall process of evaluating the p-ESRAC model included detecting aorta, initializing seeds, resampling, downsampling, implementing the active contour and iterative morphological operations. Completing all the computations took 12 minutes, 7.8 minutes of which was taken by implementing the active contour for 700 iterations and applying the downsampling by a factor of 2. By contrast, manual segmentation took around 30 minutes for one subject, so by employing the automated p-ESRAC model, the segmentation time decreased by 35%.

4.5 Conclusion

Because of the dual enhancement and geometric proximity of the kidney and the liver, segmentation of the liver is an extremely difficult, complex task. This paper proposes a novel edge function-scaled region-based active contour (ESRAC) algorithm

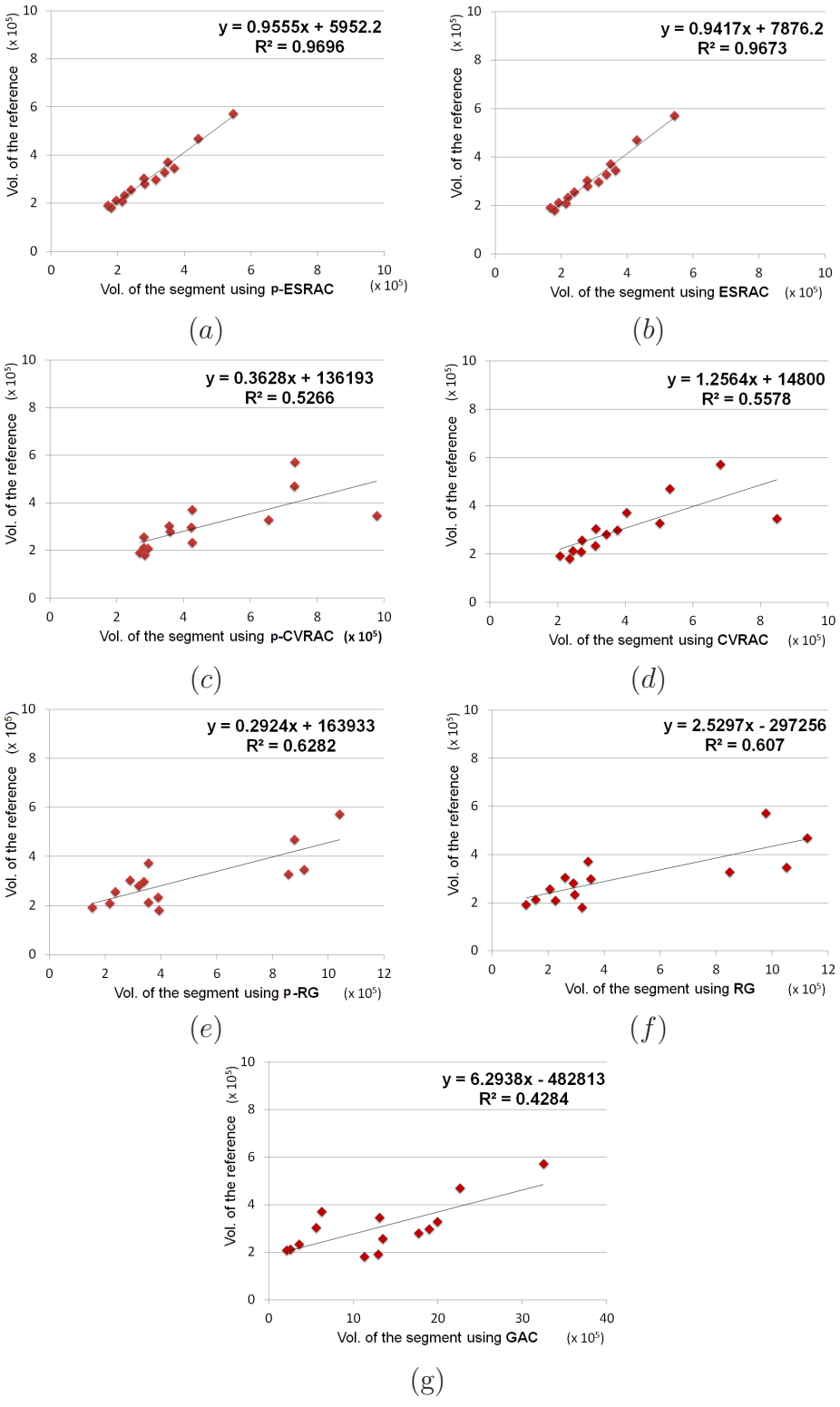

Figure 32: Linear regression models and R^2 coefficients between the segmented volume resulted from using (a) p-ESRAC, (b) ESRAC, (c) p-CVRAC, (d) CVRAC, (e) p-RG, (f) RG, and (g) GAC methods and the reference volume for 14 subjects.

to resolve the leakage-to-kidney, under- and over-segmentation problems. We applied automated multiple partitions of the liver because of inhomogeneous intensity distribution and verified this approach through qualitative and quantitative evaluations with manually-segmented reference volumes of 14 real subjects. The experimental results revealed that compared to other techniques, the ESRAC model considerably reduced over-segmentation, including the leakage of the kidney, and decreased the false-positive rate to 4.2($\pm$2.9)%. Furthermore, its partitioned version (p-ESRAC) decreased under-segmentation and increased the true-positive rate to 92.5($\pm$3.1)%. Based on further quantitative metrics, the p-ESRAC resulted in even more accurate segmentation than the region growing, Chan-Vese region-based active contour, or geodesic active contour methods. Therefore, despite the atypical shape and inhomogeneous intensity of the target (i.e., the liver) and its weak boundary conditions (i.e., its surroundings), the p-ESRAC is a promising automated technique for MR imaging.

CHAPTER V

FEATURE ANALYSIS

A significant purpose in grading liver disease is to assess the level of remaining liver function and estimate regional liver function. On motion-corrected and segmented liver parenchyma regions, quantification of the concentration of liver-specific MRI contrast agent is performed. Liver signal intensity change is evaluated from the hepatobiliary phase (3-20 minutes after injection), and parenchymal texture features are deduced from the equilibrium phase (3 minutes after injection). To build a classifier using texture features, the highly correlated image features are selected first, based on distance criteria, and training feature vectors with the known degree of malignancy were used to train a supervised learning algorithm. Maximum-a-posterior (MAP) decision rule determines which group the test data belong to. The classifier is validated by assessing the prediction accuracy using leave-one-out cross-validation.

5.1 Signal Intensity Analysis

Hepatic contrast agent is taken up to various degrees by functioning hepatocytes, and the paramagnetic property of the contrast agent shorten the longitudinal relaxation time (T1) of the liver. This shortening effect of T1 causes varying increase of signal intensity in T1-weighted MRI. There are representative approaches to quantify the hepatic function. First, qualitative method measures the shape of the signal intensity curve. And semi-quantitative methods are used to measure indices that describe one or more parts of signal intensity curves such as uptake slope, max amplitude, and the washout area under curve. Lastly, a true quantitative method is used to measure indices from contrast medium concentration changes using pharmacokinetic modeling, including measuring relaxation rate or contrast concentration. Due to the constraints

of low temporal resolution in the range of dynamic phase and MRI-related unknown parameters, enabled quantitative methods are very limited.

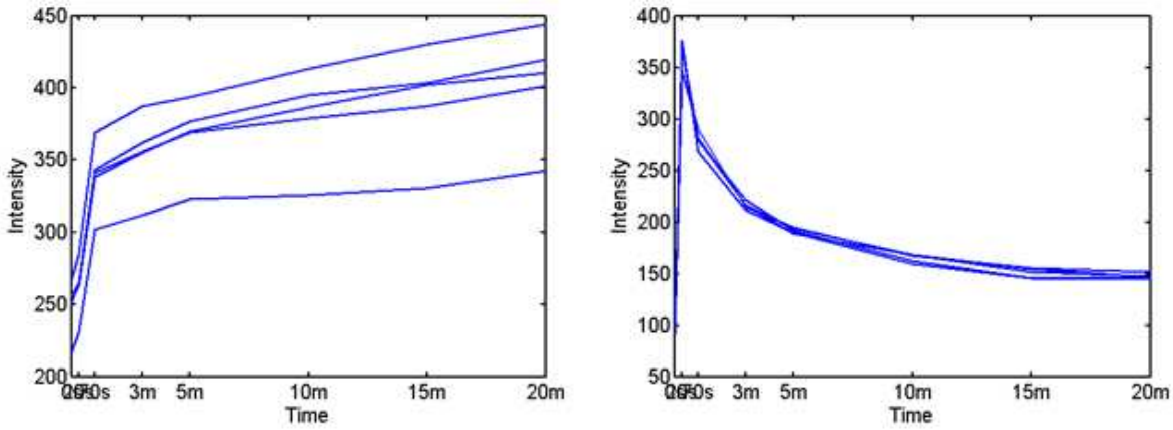

(a) (b)

Figure 33: Signal Intensity Curve for selected ROIs in (a) parenchyma and (b) aorta.

Hepatobiliary-specific contrast agent such as gadoxetate disodium (Gd-EOB-DTPA, Eovist or Primovist, Bayer HealthCare) allows data acquisition in the hepatocyte phase at 20 minutes after injection of contrast agent in addition to the usual dynamic phase examination. Figure 33 illustrates the signal intensity in time series for five ROIs in the liver parenchyma and the aorta, which supplies the blood to the hepatic artery. For a computation of the slope at the hepatobiliary phases (3-20 minutes), the mean signal intensity points over the liver parenchyma are subtracted by the signal intensity at the start of the hepatobiliary phase (3 minutes), and then normalized with division by the peak of aorta signal as follows:

$$\text{The normalized subtract intensity} = \frac{S_k - S_{3\text{ min}}}{S_{\text{aorta peak}}}. \tag{70}$$

The mean slope can be approximated as the hypotenuse of a rectangled triangular geometry with the same area as the sum of trapezoidal areas, A_1 through A_4 time division as Equation (71). If the signal intensity increases monotonously, the computed mean slope is positive. Otherwise, the computed mean slope is close to zero or less

than zero.

$$\text{The mean slope in hepatobiliary phases} = \frac{\sum_{p\in\Omega}^{N}\left\{\frac{2}{(20-3)^2}, \sum_{k=1}^{4} A_k\right\}}{N} \tag{71}$$

where A_k is the area of k-th trapezoidal division in the signal intensity curve, which is illustrated in Figure 34. p indicates the voxel in the liver parenchyma region and N is the number of the voxels of interest.

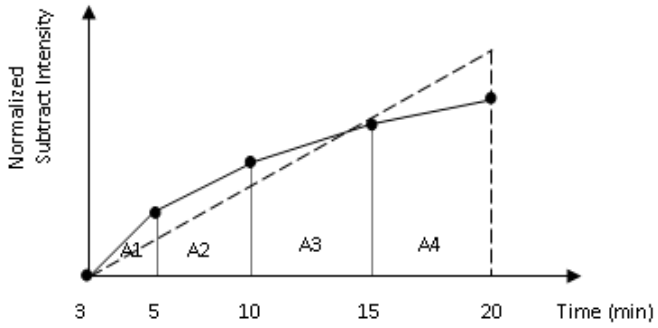

Figure 34: Computation of mean slope in hepatobiliary phases (3-20 minutes).

5.1.1 Experimental results

For 14 real patients with known pathologic scores, the signal intensity curves were compared and the mean slope was computed as well. As a result, in Figure 35, it is deduced that functioning hepatocyte and excretion of the contrast agent through the biliary pathway differs between healthy and unhealthy groups.

Quantitative results of the mean slope are shown in Figure 36 (a) where the normal group, including the mild case, is differentiated from the abnormal group based on the specific quantity. Student's t-test analysis (b) with options of one-tailed distribution, unpaired two-sample, unequal variance had the p-value of 0.0039 which results in the rejection of the null hypothesis at the significance level of 0.05; this result is statistically significant. Also, strong correlation (c) of 0.8186 was demonstrated

between the mean slope and the degree of fibrosis, which indicates the usefulness of assessing the progress of liver fibrosis.

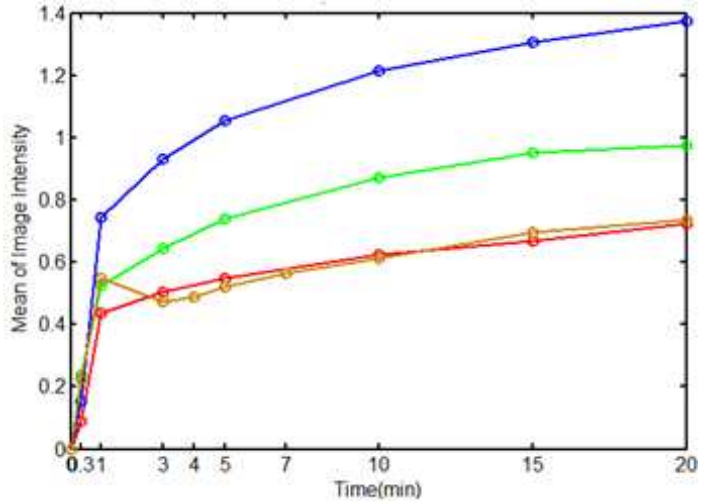

(a)

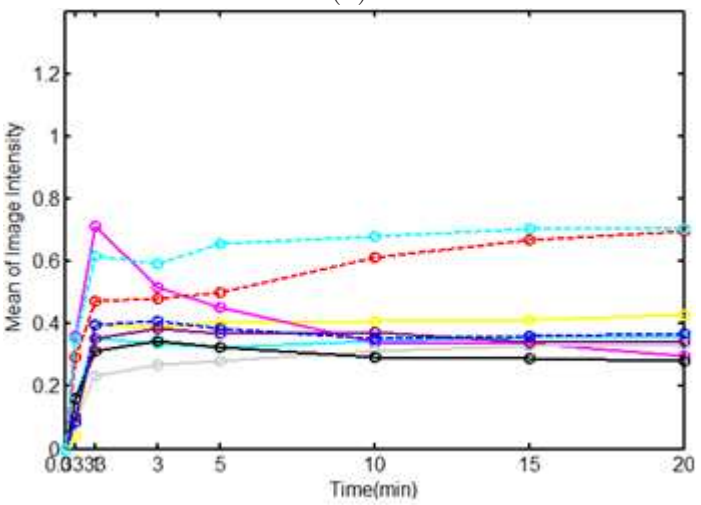

(b)

Figure 35: Signal intensity curve of (a) a healthy group and (b) an unhealthy group with CLD.

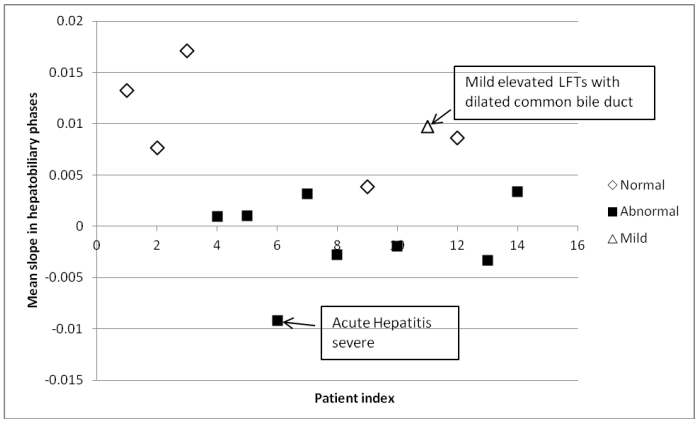

(a)

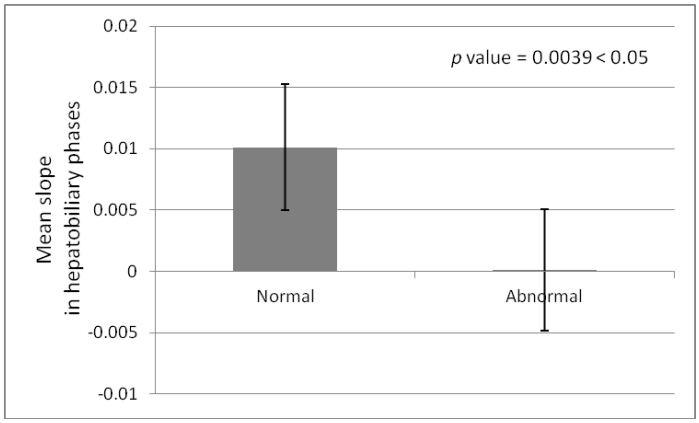

(b)

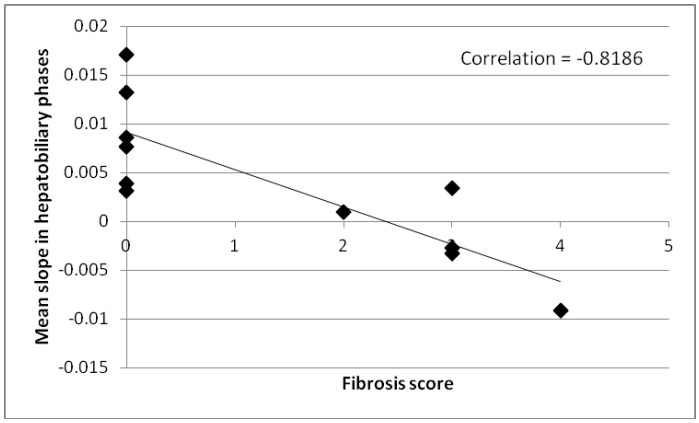

(c)

Figure 36: Quantitative results of signal intensity analysis: (a) Distribution of mean slope, (b) T-test between healthy and unhealthy groups, and (c) Correlation of the degree of liver fibrosis and the mean slope.

5.2 Texture Feature Analysis

Based on prior studies [72, 73], the magnitude of liver inflammation would correlate with the degree of abnormally increased enhancement at the arterial phase that appears as irregular wedge-shaped liver patterns. Also, linear patterns of abnormal enhancement at the interstitial phase would correlate with hepatic fibrosis. To extract those linear or wedge-shaped features on the MR image, we will use the Gabor filter [74] to perform edge detection with frequency and orientation variabilities. The complex Gabor function in the space domain is

$$g(x, y) = s(x, y)w_r(x, y), \tag{72}$$

where $s(x, y)$ is a complex sinusoidal known as a carrier, and $w_r(x, y)$ is a 2D Gaussian-shaped function known as an envelope.

The complex sinusoidal is defined as follows:

$$s(x, y) = exp\left(j\left(2\pi\left(u_0 x + v_0 y\right) + P\right)\right), \tag{73}$$

where (u_0, v_0) and P denote the spatial frequency and the phase of a sinusoidal, respectively. The Gaussian envelop is

$$w_r(x, y) = K\, exp\left(-\pi\left(a^2\left(x - x_0\right)_r^2 + b^2\left(y - y_0\right)_r^2\right)\right), \tag{74}$$

where K scales the magnitude of the Gaussian envelope, (x_0, y_0) is the position in which the envelop has a peak amplitude, a and b are scaling parameters of the envelop, and r stands for a rotation operation. The Gabor filter is applied in eight different orientations, and the combination of symmetric and anti-symmetric filtering yields the Gabor energy. It is followed by non-classical receptive field inhibition [75] that reduces influence of stimuli in the surroundings and enhanced the linear structure. A

normalized weighting function w_σ is defined as

$$w_\sigma(x,y) = \frac{1}{\|H(DoG_\sigma)\|_1} H(DoG_\sigma(x,y)), H(z) = \begin{cases} 0, & z < 0 \\ z, & z \geq 0 \end{cases} \tag{75}$$

where $DoG_\sigma(x,y)$ is the difference of Gaussian functions as follows:

$$DoG_\sigma(x,y) = \frac{1}{2\pi(4\sigma)^2} e^{-\frac{x^2+y^2}{2(4\sigma)^2}} - \frac{1}{2\pi\sigma^2} e^{-\frac{x^2+y^2}{2\sigma^2}}. \tag{76}$$

Anisotropic non-CRF inhibition was applied by computing an inhibition term for each orientation as a convolution of the Gabor energy with the weighting function.

The first texture feature (f_1) is obtained by computing the ratio of the number of structure pixels to the total number of pixels, including the number of non-structure pixels in the resulting image as follows:

$$\text{linear structure ratio } f_1 = \frac{N_S}{N_S + N_B}, \tag{77}$$

where N_S is the number of structure voxels and N_B is the number of non-structure voxels. Figure 37 illustrates the process of computing the linear structure.

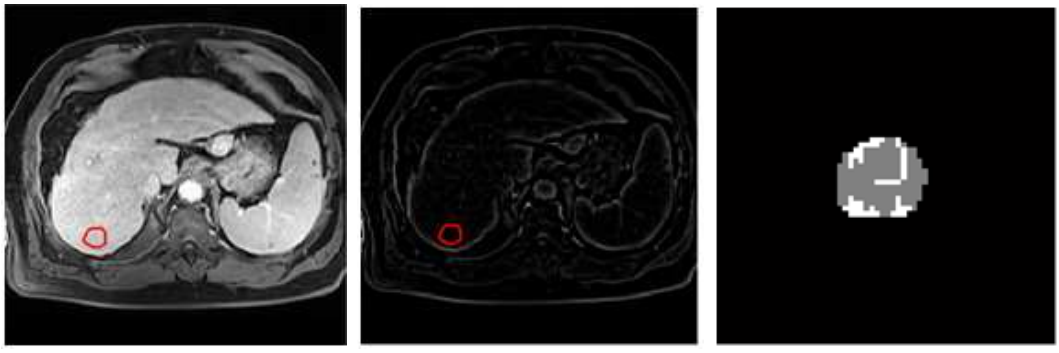

Figure 37: Extracting linear or wedge-shaped structures using the Gabor filtering and non-CRF inhibition.

The rest of texture features are generated from the grey level co-occurrence matrix (GLCM) which is a popular statistical method examining textures that incorporate

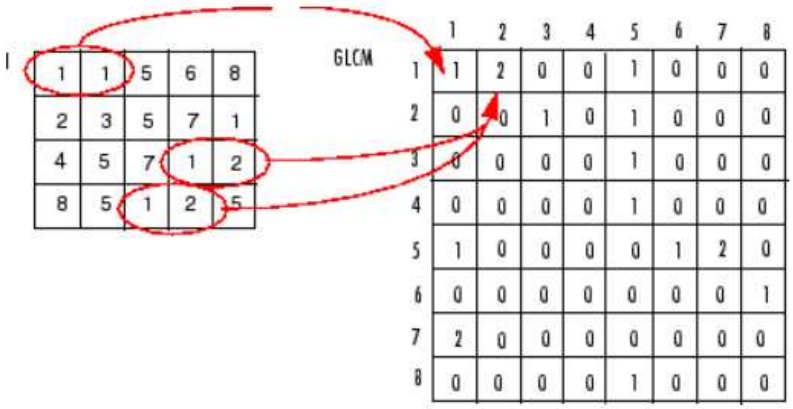

Figure 38: GLCM calculation in 2-D image (courtesy of MATLAB).

the spatial relationship of neighboring pixels. The GLCM functions characterize the texture of an image by calculating how often pixel pairs with specific values and in a specified spatial relationship occur in an image.

The two-dimensional GLCM is computed with a radius of one to three pixels and a set of 0, 45, 90, and 135 degrees from the central pixel of a 16×16 window moving within the image, and then is used for computing local statistical measurements. Next, they are applied with a Gaussian window centered on the centroid of the ROI to obtain global statistics. Thereby, the remote points should have less influence than points located near the center of the Gaussian window. The mean of twelve sets of weighted GLCM is computed for each ROI. We independently ranked key features by class separability criteria, such as fisher score, and the most significant features among the second order statistics of interest are

$$\text{Entropy } f_2 = -\sum_i \sum_j p(i,j)\, log\left(p(i,j)\right), \tag{78}$$

$$\text{Dissimilarity } f_3 = \sum_i \sum_j |i-j|\, p(i,j), \tag{79}$$

$$\text{Inverse difference (homogeneity) } f_4 = \sum_i \sum_j \frac{p(i,j)}{1+|i-j|}, \tag{80}$$

$$\text{Sum average } f_5 = \sum_{i=2}^{2N_g} i * p_{x+y}(i), \tag{81}$$

$$\text{and variance } f_6 = \sum_i \sum_j (i-\mu)^2 p(i,j), \tag{82}$$

where p is the normalized GLCM, $p_{x+y}(k) = \sum_i \sum_j p(i,j)$ with $i+j=k$, and N_g is the number of grey levels.

5.3 Classification

Using six features described in 5.2, we will construct the supervised classifier using a multivariate normal distribution model and a maximum a posteriori (MAP) decision rule. The multivariate normal distribution model is the one-dimensional (univariate) normal distribution generalized to higher dimensions (N) as follows:

$$p(\mathbf{x}|w_i) = \frac{1}{(2\pi)^{\frac{N}{2}} \left|\hat{\mathbf{\Sigma}}_\mathbf{i}\right|^{\frac{1}{2}}} exp\left(-\frac{1}{2}(\mathbf{x}-\hat{\mu}_\mathbf{i})^T \hat{\mathbf{\Sigma}}_\mathbf{i}^{-1}(\mathbf{x}-\hat{\mu}_\mathbf{i})\right), \tag{83}$$

where $\hat{\mu}_\mathbf{i}$ is an N-vector, $\hat{\mathbf{\Sigma}}_\mathbf{i}$ a symmetric and semi-definite $N \times N$ covariance matrix, and $\left|\hat{\mathbf{\Sigma}}_\mathbf{i}\right|$ the determinant of $\hat{\mathbf{\Sigma}}_\mathbf{i}$ for the class w_i. The parameters $\hat{\mu}_\mathbf{i}$ and $\hat{\mathbf{\Sigma}}_\mathbf{i}$ are determined by using a set of training data with known output values, e.g., severity degrees of fibrosis in our case. According to Bayes' theorem, the posterior probability can be represented as

$$p(w_i|\mathbf{x}) = \frac{p(w_i)\,p(\mathbf{x}|w_i)}{p(\mathbf{x})}. \tag{84}$$

Because the denominator of Equation (84) is not dependent on the class w_i, we can simplify the equation as

$$p\left(w_i|\mathbf{x}\right) = p\left(w_i\right) p\left(\mathbf{x}|w_i\right). \tag{85}$$

The logarithm of the MAP estimator using the multivariate normal distribution model is computed as

$$\hat{i}_{MAP}(\mathbf{x}) = arg_i max \left\{ ln\left(p\left(w_i\right)\right) - \frac{N}{2} ln\left(2\pi\right) - \frac{1}{2} ln\left|\hat{\mathbf{\Sigma}}_\mathbf{i}\right| - \frac{1}{2}\left(\mathbf{x} - \hat{\mu}_\mathbf{i}\right)^T \hat{\mathbf{\Sigma}}_\mathbf{i}^{-1} \left(\mathbf{x} - \hat{\mu}_\mathbf{i}\right) \right\}. \tag{86}$$

Next, we will validate this classifier by assessing the prediction accuracy. To reduce variability, multiple rounds of a cross-validation, called a rotation estimation, will be performed using different partitions, and the validation results will be averaged over the rounds. One round of the cross-validation involves partitioning a sample of data into complementary subsets, performing the analysis on one subset called the training set, and validating the analysis on the other subset called the validation set or testing set.

5.3.1 Experimental Results

It is known that the degree of liver fibrosis is a predictive factor for the occurrence of hepatocellular carcinoma, so called HCC. The detection and accurate staging of hepatic fibrosis or cirrhosis can be found by paying attention to the reticular enhancement patterns over the liver parenchyma due to delayed enhancement on equilibrium phase images. Figure 39 shows the computed linear structure ratio for selected ROIs with true fibrosis scores, which resulted in a strong correlation between them.

The features, including the linear structure ratio and the GLCM features, are sorted by the Fisher criterion in Table 9, and the most significant six features are selected for building learning models.

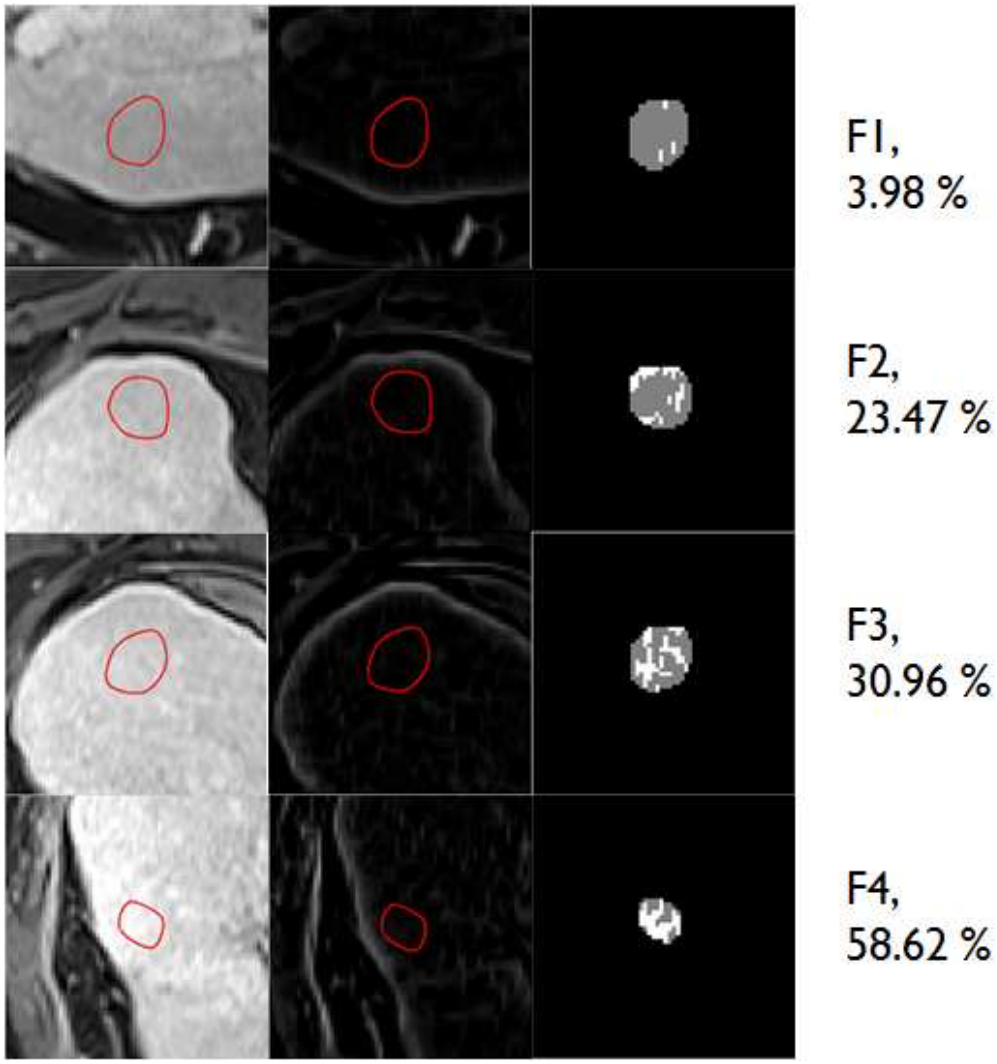

Figure 39: Reticular enhancement patterns related to the degree of liver fibrosis.

Table 9: Supervised feature selection using Fisher score. The feature with asterisk indicates the selected feature.

Features	Fisher score
*Percentile of structure pixel	1.238
*Entropy	1.017
*Dissimilarity	1.014
*Inverse Difference	1.008
*Sum Average	0.946
*Variance	0.929
Energy	0.926
Max of bins in Hough transform	0.924
Difference entropy	0.914
Contrast	0.850

Figure 40 demonstrates numerical results of the cross-validation. The matrix (a) shows detailed classification results in which diagonal elements correspond the perfect matching between true grades and computed grades. The bar graph (b) specifies a distribution of classification results with respect to a grade error allowance, respectively. The MR image (c) demonstrates the selected regions of interest and their true scores assigned by experts, which will be used as a set of training data in the developed classifier. The colored MR image (d) represents automatically computed fibrosis severity degrees ranging from 0 to 4 with a specified RGB colormap for every pixel over the liver region, excluding a background and blood vessels. Using a MAP classifier, we performed leave-one-out cross-validation which involves using a single observation as the validation data, and the remaining observations as the training data. This is repeated such that each observation in the sample is used once as the validation data. For the 126 rounds of cross-validation, Figure (a) is the classification matrix, and Figure (b) shows 55% matching with no error, 37% matching with score error of 1, 8% matching with score error of 2, 0.8% matching with score error of 3.

Figure (c) is the slice image on which the clinicians mark ROI and its score. Figure (d) is the colormap which shows the fibrosis scores over the entire liver domain except hepatic vein, artery or surrounding organs.

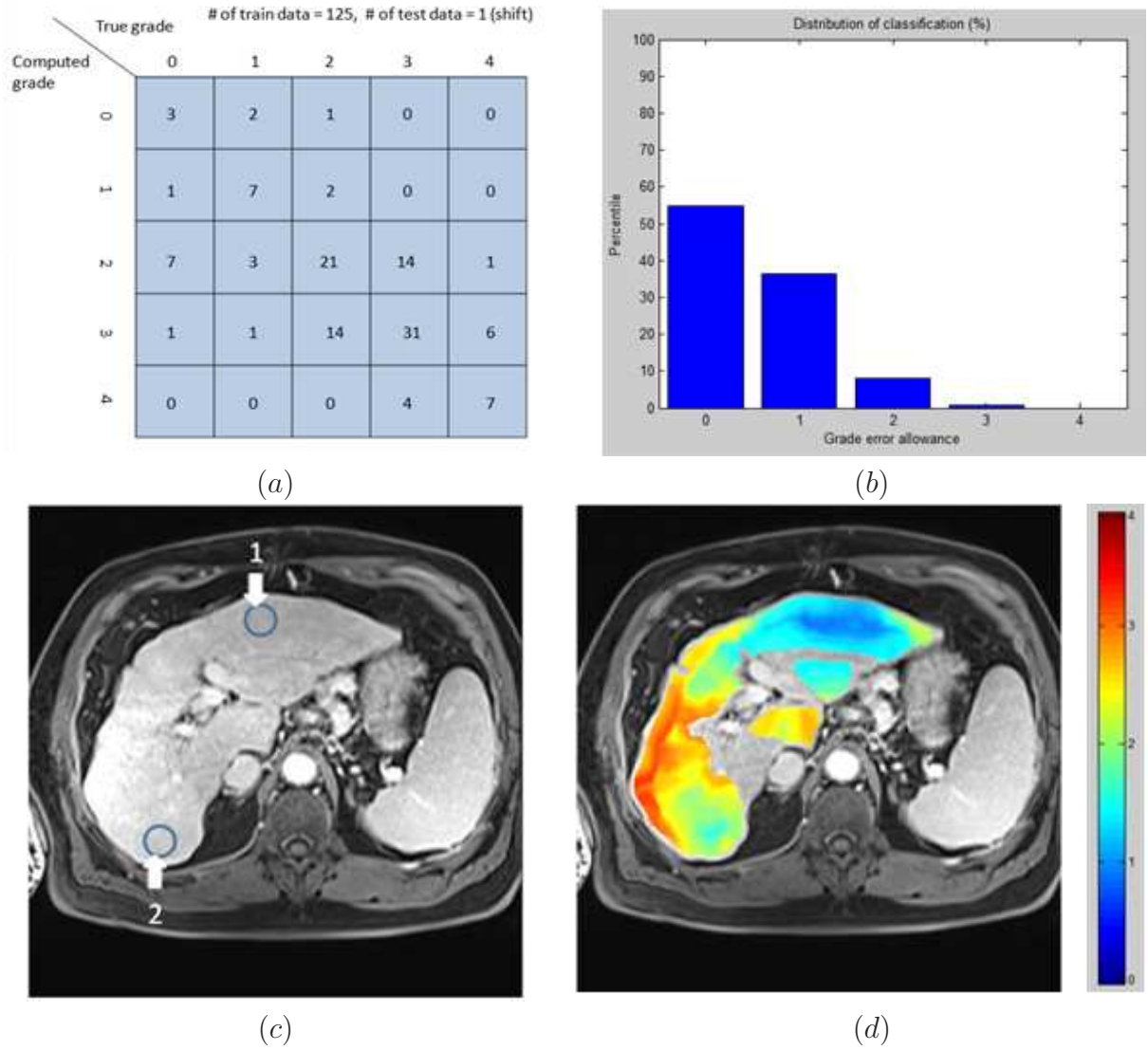

Figure 40: Cross-validation results using a MAP classification. The matrix (a) denotes the distribution between true grades and corresponding computed grades related to fibrosis severities. The bar graph (b) is the distribution of matching percentiles with respect to grade error allowances. The MR image (c) and (d) specify the true grades scored by experts for the selected regions and a colormap representation of computed grades, respectively.

CHAPTER VI

CONCLUSION AND FUTURE WORKS

In this dissertation, we proposed novel image registration and segmentation algorithms suitable for contrast-enhanced liver MRI and demonstrated a supervised learning method using image features. Image registration proposed in this dissertation is the demons algorithm based on the local correlation coefficient that accounts for changing, but correlated intensities between the reference and moving images. Employing bi-directional and parallel computing schemes is also proposed to accelerate convergence without a loss of accuracy. Image segmentation introduced is an edge function-scaled region-based active contour that coupled regional statistics and gradient information in a straightforward way. Because of inhomogeneities of a static magnetic field and a localized contrast uptake, an image volume was linearly separated into multiple functioning partitions, in which local-based regional statistics was computed, respectively.

In Chapter 3, a bi-directional local correlation coefficient (Bi-LCC) demons method was introduced for motion correction of contrast-enhanced liver MRI with the potential for clinical applications. By introducing a bi-directional scheme, the Bi-LCC demons, compared to the uni-directional LCC demons and simplified versions, could achieve the fastest convergence to the steady-state and highest accuracy such that the average error is subvoxel size. The GPU implementation of image registration boosted performance considerably and proved that OpenCL is very competitive with CUDA in popular. As another registration topic, registration of two-dimensional liver histology and three-dimensional MRI is an important step required for optimized analysis of the correlation between histologic tissue evaluation on specimens

and corresponding ROIs of MRI. Manually selected multiple point landmarks initialized a similarity transformation, and then the spatially-varying diffusion registration, combining a liver mask and point landmarks, yielded the accurate alignment of histology and MRI.

In Chapter 4, a novel edge function-scaled region-based active contour (ESRAC) algorithm was presented to resolve the leakage-to-kidney, under-, and over-segmentation problems. The automated linear multiple partitions, which approximates the Couinaud liver segments, was also applied to the computation of local regional statistics of the ESRAC. The experimental results revealed that compared to other techniques, the ESRAC model considerably reduced over-segmentation, including the leakage of the kidney, and decreased the false-positive rate. Furthermore, its partitioned version (p-ESRAC) significantly decreased under-segmentation. Based on further quantitative metrics, the p-ESRAC is considered to be a promising automated technique for liver MR imaging.

In Chapter 5, signal intensity changes and texture features were analyzed to assess the level of remaining liver function and to estimate regional liver function. Using a MAP classifier, leave-one-out cross-validation was performed, which resulted in 92% matching within score error of one. The colormap representation of the measured fibrosis score significantly facilitated the diagnosis of liver disease in the entire liver.

The proposed image registration and segmentation algorithms are highly suitable for contrast-enhanced liver MRI. Furthermore, the methods can be potentially applicable in contrast-enhanced imaging of other organs. For example, MR perfusion imaging of the brain is often used to evaluate brain function via assessment of functional parameters describing passage of blood through the brain's vascular network. Dynamic sequences must be fast to capture the rapid first-pass transit of a bolus of contrast agent through the brain, which is on the order of less than 20 seconds. Image

registration of dynamic images are required for the accurate assessment of the parameters, and the proposed registration method will be beneficial in this regard. For the heart, cine imaging is often acquired to depict the motion of the heart over multiple phases of the cardiac cycle and dynamic contrast enhanced MRI are often used to image perfusion. The LCC demons algorithm can be applied to register cardiac cine images for quantitative analysis.

The registration method developed here is applicable in a variety of circumstances in medical imaging. If the similarity measure used in the demons framework is changed to normalized mutual information, registration of other modalities (PET-MRI, CT-MRI, etc) are possible. The acceleration of our algorithm by GPU is important in time sensitive clinical applications. For instance, interventional procedures are traditionally supported by intra-operative imaging (X-ray fluoroscopy, ultrasound). There is real time feedback, but the images provide limited information. Surgical procedures are traditionally supported with pre-operative images (CT, MRI). But a link between images and patient for the duration of operation needs to be established with registration. For both cases, image registration can play an essential role augmenting intra-operative images with preoperative ones. With such an approach, image guidance can draw upon a combination of pre-operative and intra-operative imaging together with magnetic or optical tracking systems, enabling precise minimally invasive procedures.

REFERENCES

[1] M.A. Clifford, F. Banovac, E. Levy, and K. Cleary, "Assessment of hepatic motion secondary to respiration for computer assisted interventions," *Computer Aided Surgery*, vol. 7, no. 5, pp. 291–299, 2002.

[2] J.P. Thirion, "Image matching as a diffusion process: an analogy with Maxwell's demons," *Medical Image Analysis*, vol. 2, no. 3, pp. 243–260, 1998.

[3] T.F. Chan and L.A. Vese, "Active contours without edges," *Image Processing, IEEE Transactions on*, vol. 10, no. 2, pp. 266–277, 2001.

[4] I. Suramo, M. Paivansalo, and M. MYLLYLA, "Cranio-caudal movements of the liver, pancreas and kidneys in respiration," *Acta radiologica. Diagnosis*, vol. 25, no. 2, pp. 129–131, 1984.

[5] SC Davies, AL Hill, RB Holmes, M. Halliwell, and PC Jackson, "Ultrasound quantitation of respiratory organ motion in the upper abdomen," *British Journal of Radiology*, vol. 67, no. 803, pp. 1096, 1994.

[6] J.M. Blackall, A.P. King, G.P. Penney, A. Adam, and D.J. Hawkes, "A statistical model of respiratory motion and deformation of the liver," *Lecture Notes in Computer Science*, pp. 1338–1340, 2001.

[7] A.J. Herline, J.D. Stefansic, J.P. Debelak, S.L. Hartmann, C.W. Pinson, R.L. Galloway, and W.C. Chapman, "Image-guided surgery: preliminary feasibility studies of frameless stereotactic liver surgery," *Archives of Surgery*, vol. 134, no. 6, pp. 644, 1999.

[8] S. Shimizu, H. Shirato, B. Xo, K. Kagei, T. Nishioka, S. Hashimoto, K. Tsuchiya, H. Aoyama, and K. Miyasaka, "Three-dimensional movement of a liver tumor detected by high-speed magnetic resonance imaging," *Radiotherapy and Oncology*, vol. 50, no. 3, pp. 367–370, 1999.

[9] T. Rohlfing, C.R. Maurer Jr, W.G. ODell, and J. Zhong, "Modeling liver motion and deformation during the respiratory cycle using intensity-based nonrigid registration of gated MR images," *Medical physics*, vol. 31, pp. 427, 2004.

[10] V. Venkatraman, M.H. Van Horn, S. Weeks, and E. Bullitt, "Liver motion due to needle pressure, cardiac, and respiratory motion during the TIPS procedure," *Lecture Notes in Computer Science*, pp. 66–72, 2004.

[11] Pascal Cachier, Xavier Pennec, and Nicholas Ayache, "Fast non rigid matching by gradient descent: study and improvements of the 'Demons' algorithm," Tech. Rep., EPIDAURE - INRIA Sophia Antipolis - INRIA, 1999.

[12] P. Rogelj and S. Kovačič, "Symmetric image registration," *Medical image analysis*, vol. 10, no. 3, pp. 484–493, 2006.

[13] H. Wang, L. Dong, J. O'Daniel, R. Mohan, A.S. Garden, K.K. Ang, D.A. Kuban, M. Bonnen, J.Y. Chang, and R. Cheung, "Validation of an accelerated'demons' algorithm for deformable image registration in radiation therapy," *Physics in Medicine and Biology*, vol. 50, no. 12, pp. 2887–2906, 2005.

[14] T. Vercauteren, X. Pennec, A. Perchant, and N. Ayache, "Diffeomorphic demons: Efficient non-parametric image registration," *NeuroImage*, vol. 45, no. 1S1, pp. 61–72, 2009.

[15] T. Mansi, J.M. Peyrat, M. Sermesant, H. Delingette, J. Blanc, Y. Boudjemline, and N. Ayache, "Physically-Constrained Diffeomorphic Demons for the

Estimation of 3D Myocardium Strain from Cine-MRI," in *Proceedings of the 5th International Conference on Functional Imaging and Modeling of the Heart*. Springer, 2009, p. 210.

[16] V. Caselles, R. Kimmel, and G. Sapiro, "Geodesic active contours," *International journal of computer vision*, vol. 22, no. 1, pp. 61–79, 1997.

[17] P. Perona and J. Malik, "Scale-space and edge detection using anisotropic diffusion," *Pattern Analysis and Machine Intelligence, IEEE Transactions on*, vol. 12, no. 7, pp. 629–639, 1990.

[18] D. Mumford and J. Shah, "Optimal approximations by piecewise smooth functions and associated variational problems," *Communications on pure and applied mathematics*, vol. 42, no. 5, pp. 577–685, 1989.

[19] H.K. Zhao, T. Chan, B. Merriman, and S. Osher, "A variational level set approach to multiphase motion," *Journal of computational physics*, vol. 127, no. 1, pp. 179–195, 1996.

[20] H. Kato, M. Kanematsu, X. Zhang, M. Saio, H. Kondo, S. Goshima, and H. Fujita, "Computer-aided diagnosis of hepatic fibrosis: preliminary evaluation of mri texture analysis using the finite difference method and an artificial neural network," *American Journal of Roentgenology*, vol. 189, no. 1, pp. 117, 2007.

[21] D. Mahmoud-Ghoneim, G. Toussaint, J.M. Constans, and J.D. de Certaines, "Three dimensional texture analysis in mri: a preliminary evaluation in gliomas," *Magnetic resonance imaging*, vol. 21, no. 9, pp. 983–987, 2003.

[22] M. Mescam, J. Bezy-Wendling, M. Kretowski, K. Jurczuk, P.A. Eliat, and D. Olivié, "Coupling texture analysis and physiological modeling for liver dynamic mri interpretation," in *Engineering in Medicine and Biology Society, 2007.*

EMBS 2007. 29th Annual International Conference of the IEEE. IEEE, 2007, pp. 4223–4226.

[23] R. Materne, AM Smith, F. Peeters, JP Dehoux, A. Keyeux, Y. Horsmans, and BE Van Beers, "Assessment of hepatic perfusion parameters with dynamic mri," *Magnetic resonance in medicine*, vol. 47, no. 1, pp. 135–142, 2001.

[24] M. Hagiwara, H. Rusinek, V.S. Lee, M. Losada, M.A. Bannan, G.A. Krinsky, and B. Taouli, "Advanced liver fibrosis: diagnosis with 3d whole-liver perfusion mr imaging—initial experience1," *Radiology*, vol. 246, no. 3, pp. 926–934, 2008.

[25] K. Miyazaki, MR Orton, DM Koh, V. Lewington, D. Atkinson, DJ Hawkes, MO Leach, and DJ Collins, "Evaluation of slope-based hepatic perfusion index quantification methods against dual-input kinetic model based approach," in *Proc. Intl. Soc. Mag. Reson. Med*, 2009, vol. 17, p. 4215.

[26] P.V. Pandharipande, G.A. Krinsky, H. Rusinek, and V.S. Lee, "Perfusion imaging of the liver: current challenges and future goals1," *Radiology*, vol. 234, no. 3, pp. 661–673, 2005.

[27] R.M. Haralick, K. Shanmugam, and I. Dinstein, "Textural features for image classification," *Systems, Man and Cybernetics, IEEE Transactions on*, vol. 3, no. 6, pp. 610–621, 1973.

[28] D.R. Martin, R. Danrad, and S.M. Hussain, "Mr imaging of the liver.," *Radiologic Clinics of North America*, vol. 43, no. 5, pp. 861, 2005.

[29] K.I. Ringe, D.B. Husarik, C.B. Sirlin, and E.M. Merkle, "Gadoxetate disodium–enhanced mri of the liver: Part 1, protocol optimization and lesion appearance in the noncirrhotic liver," *American Journal of Roentgenology*, vol. 195, no. 1, pp. 13–28, 2010.

[30] A. Carrillo, J.L. Duerk, J.S. Lewin, and D.L. Wilson, "Semiautomatic 3-d image registration as applied to interventional mri liver cancer treatment," *Medical Imaging, IEEE Transactions on*, vol. 19, no. 3, pp. 175–185, 2000.

[31] T. Böttger, N.V. Ruiter, R. Stotzka, R. Bendl, and K.K. Herfarth, "Registration of ct and mri volume data of the liver," in *International Congress Series*. Elsevier, 2003, vol. 1256, pp. 118–123.

[32] W.C. Christina Lee, M.E. Tublin, and B.E. Chapman, "Registration of mr and ct images of the liver: comparison of voxel similarity and surface based registration algorithms," *Computer methods and programs in biomedicine*, vol. 78, no. 2, pp. 101–114, 2005.

[33] P. Cachier and X. Pennec, "{3D} Non-Rigid Registration by Gradient Descent on a Gaussian-Windowed Similarity Measure using Convolutions," *Proc. of MMBIA00*, pp. 182–189, 2000.

[34] WC Hayes, LM Keer, G. Herrmann, and LF Mockros, "A mathematical analysis for indentation tests of articular cartilage.," *Journal of biomechanics*, vol. 5, no. 5, pp. 541, 1972.

[35] Y.C. Fung, *Biomechanics: mechanical properties of living tissues*, Springer, 1993.

[36] A. Sarvazyan, A. Skovoroda, S. Emelianov, JB Fowlkes, JG Pipe, RS Adler, RB Buxton, and PL Carson, "Biophysical bases of elasticity imaging," *Acoustical Imaging*, vol. 21, pp. 223–240, 1995.

[37] AR Skovoroda, AN Klishko, DA Gusakyan, YI Mayevskii, VD Yermilova, GA Oranskaya, and AP Sarvazyan, "Quantitative analysis of the mechanical characteristics of pathologically changed soft biological tissues," *Biophysics*, vol. 40, no. 6, pp. 1359–1364, 1995.

[38] M. Zhang, YP Zheng, and A.F.T. Mak, "Estimating the effective Young's modulus of soft tissues from indentation tests?nonlinear finite element analysis of effects of friction and large deformation," *Medical Engineering and Physics*, vol. 19, no. 6, pp. 512–517, 1997.

[39] TA Krouskop, TM Wheeler, F. Kallel, BS Garra, and T. Hall, "Elastic moduli of breast and prostate tissues under compression," *Ultrasonic imaging(Print)*, vol. 20, no. 4, pp. 260–274, 1998.

[40] T. Hu and J.P. Desai, "A biomechanical model of the liver for reality-based haptic feedback," *Lecture notes in computer science*, pp. 75–82, 2003.

[41] A. Nava, E. Mazza, M. Furrer, P. Villiger, and WH Reinhart, "In vivo mechanical characterization of human liver," *Medical Image Analysis*, vol. 12, no. 2, pp. 203–216, 2008.

[42] J.-P. Thirion, "Image matching as a diffusion process: an anlogy with maxwell's demons," vol. 2, no. 3, pp. 243–260, Sept. 1998.

[43] J.M. Geusebroek, A.W.M. Smeulders, and J. Van De Weijer, "Fast anisotropic gauss filtering," *Image Processing, IEEE Transactions on*, vol. 12, no. 8, pp. 938–943, 2003.

[44] S. Tan, J.L. Dale, and A. Johnston, "Performance of three recursive algorithms for fast space-variant gaussian filtering," *Real-Time Imaging*, vol. 9, no. 3, pp. 215–228, 2003.

[45] Jan Modersitzki, *Numerical Methods for Image Registration*, Oxford Science Publications, 2004.

[46] A. Bistoquet, J. Oshinski, and O. Škrinjar, "Myocardial deformation recovery from cine MRI using a nearly incompressible biventricular model," *Medical Image Analysis*, vol. 12, no. 1, pp. 69–85, 2008.

[47] T. Hausken, D.F. Leotta, S. Helton, K.V. Kowdley, B. Goldman, S. Vaezy, E.L. Bolson, F.H. Sheehan, and R.W. Martin, "Estimation of the human liver volume and configuration using three-dimensional ultrasonography: effect of a high-caloric liquid meal," *Ultrasound in medicine & biology*, vol. 24, no. 9, pp. 1357–1367, 1998.

[48] Pascal Cachier, Xavier Pennec, and Nicholas Ayache, "Fast non rigid matching by gradient descent: study and improvements of the 'demons' algorithm," Tech. Rep. 3706, EPIDAURE - INRIA Sophia Antipolis - INRIA, June 1999.

[49] S.S. Samant, J. Xia, P. Muyan-
"Ozçelik, and J.D. Owens, "High performance computing for deformable image registration: Towards a new paradigm in adaptive radiotherapy," *Medical Physics*, vol. 35, pp. 3546, 2008.

[50] P. Muyan-Ozcelik, J.D. Owens, J. Xia, and S.S. Samant, "Fast deformable registration on the GPU: A CUDA implementation of demons," in *International Conference on Computational Sciences and Its Applications*, 2008, pp. 223–233.

[51] A. Munshi, "OpenCL 1.0 Specification," *Khronos Group, May*, 2009.

[52] H. Wu, A.M. Krasinskas, M.E. Tublin, and B.E. Chapman, "Registering liver pathological images with prior in vivo ct/mri data," *Medical Image Computing and Computer-Assisted Intervention–MICCAI 2005*, pp. 564–571, 2005.

[53] O. Škrinjar, "Point-based registration with known correspondence: Closed form optimal solutions and properties," *Biomedical Image Registration*, pp. 315–321, 2006.

[54] K. Rohr, P. Cathier, and S. Worz, "Elastic registration of electrophoresis images using intensity information and point landmarks," *Pattern recognition*, vol. 37, no. 5, pp. 1035–1048, 2004.

[55] P. Cachier and N. Ayache, "Isotropic energies, filters and splines for vector field regularization," *Journal of Mathematical Imaging and Vision*, vol. 20, no. 3, pp. 251–265, 2004.

[56] A.S. Frangakis and R. Hegerl, "Noise reduction in electron tomographic reconstructions using nonlinear anisotropic diffusion," *Journal of structural biology*, vol. 135, no. 3, pp. 239–250, 2001.

[57] U. Vovk, F. Pernus, and B. Likar, "A review of methods for correction of intensity inhomogeneity in mri," *Medical Imaging, IEEE Transactions on*, vol. 26, no. 3, pp. 405–421, 2007.

[58] T. Heimann, B. Van Ginneken, M.A. Styner, Y. Arzhaeva, V. Aurich, C. Bauer, A. Beck, C. Becker, R. Beichel, G. Bekes, et al., "Comparison and evaluation of methods for liver segmentation from ct datasets," *Medical Imaging, IEEE Transactions on*, vol. 28, no. 8, pp. 1251–1265, 2009.

[59] D. Kainmüller, T. Lange, and H. Lamecker, "Shape constrained automatic segmentation of the liver based on a heuristic intensity model," in *Proc. MICCAI Workshop 3D Segmentation in the Clinic: A Grand Challenge*, 2007, pp. 109–116.

[60] K.A. Saddi, M. Rousson, C. Chefdhotel, and F. Cheriet, "Global-to-local shape matching for liver segmentation in ct imaging," in *MICCAI 2007 Workshop Proceedings of the 3D Segmentation in the Clinic: a Grand Challenge*, 2007, pp. 207–214.

[61] P. Slagmolen, A. Elen, D. Seghers, D. Loeckx, F. Maes, and K. Haustermans, "Atlas based liver segmentation using nonrigid registration with a b-spline transformation model," in *MICCAI 2007 Workshop Proceedings of the 3D Segmentation in the Clinic: a Grand Challenge*. Citeseer, 2007, pp. 196–206.

[62] L. Rusko, G. Bekes, G. Németh, and M. Fidrich, "Fully automatic liver segmentation for contrast-enhanced ct images," *MICCAI Wshp. 3D Segmentation in the Clinic: A Grand Challenge*, vol. 2, no. 7, 2007.

[63] Y. Boykov and G. Funka-Lea, "Graph cuts and efficient nd image segmentation," *International Journal of Computer Vision*, vol. 70, no. 2, pp. 109–131, 2006.

[64] L. Ruskó and G. Bekes, "Liver segmentation for contrast-enhanced mr images using partitioned probabilistic model," *International journal of computer assisted radiology and surgery*, vol. 6, no. 1, pp. 13–20, 2011.

[65] G. Chen, L. Gu, L. Qian, and J. Xu, "An improved level set for liver segmentation and perfusion analysis in mris," *Information Technology in Biomedicine, IEEE Transactions on*, vol. 13, no. 1, pp. 94–103, 2009.

[66] N. Paragios, R. Deriche, et al., "Coupled geodesic active regions for image segmentation," 1999.

[67] Y. Chen, F. Huang, H.D. Tagare, and M. Rao, "A coupled minimization problem for medical image segmentation with priors," *International journal of computer vision*, vol. 71, no. 3, pp. 259–272, 2007.

[68] J. Oh, D. Martin, and O. Skrinjar, "Gpu-based motion correction of contrast-enhanced liver mri scans: An opencl implementation," in *Biomedical Imaging: From Nano to Macro, 2011 IEEE International Symposium on*. IEEE, 2011, pp. 783–786.

[69] D.H. Ballard, "Generalizing the hough transform to detect arbitrary shapes," *Pattern recognition*, vol. 13, no. 2, pp. 111–122, 1981.

[70] D.W. Shattuck and R.M. Leahy, "Brainsuite: an automated cortical surface identification tool," *Medical Image Analysis*, vol. 6, no. 2, pp. 129–142, 2002.

[71] R. Adams and L. Bischof, "Seeded region growing," *Pattern Analysis and Machine Intelligence, IEEE Transactions on*, vol. 16, no. 6, pp. 641–647, 1994.

[72] D.R. Martin, D. Seibert, M. Yang, K. Salman, and M.P. Frick, "Reversible heterogeneous arterial phase liver perfusion associated with transient acute hepatitis: Findings on gadolinium-enhanced mri," *Journal of Magnetic Resonance Imaging*, vol. 20, no. 5, pp. 838–842, 2004.

[73] R. Danrad and D.R. Martin, "Mr imaging of diffuse liver diseases.," *Magnetic resonance imaging clinics of North America*, vol. 13, no. 2, pp. 277, 2005.

[74] J.R. Movellan, "Tutorial on gabor filters," *Open Source Document*, 2002.

[75] C. Grigorescu, N. Petkov, and M.A. Westenberg, "Contour detection based on nonclassical receptive field inhibition," *Image Processing, IEEE Transactions on*, vol. 12, no. 7, pp. 729–739, 2003.